Study of black hole spin of Cyg X-1 with the X-ray spectral/timing analysis

Takafumi Kawano

Doctoral Thesis
Hiroshima University

January 2017

Abstract

Measuring black hole spin (rotation of black hole) is important in order to understand the relativistic jet seen from the accretion flow. However, unlike mass, spin is difficult to determine as it only affects the spacetime properties very close to the black hole. There are three potential methods to estimate black hole spin. Two of them use the spin-dependence of the last stable circular orbit around the black hole as a diagnostic. This minimum radius leads to the maximum temperature and the highest luminosity of the disk emission. It also gives the fastest orbital velocity and strongest gravity which together sculpt the profile of the fluorescent iron line emission. The other proposed method instead uses the characteristic fast variability features (low and high frequency quasi-periodic oscillations: QPOs), interpreting these as the spin-dependent relativistic precession timescales (Lense-Thirring, and radial/vertical oscillation or Lense-Thirring and vertical/breathing mode oscillations). Black hole binaries are very bright, and thus, the statistical quality of the data is extremely good, giving small uncertainties on the derived spin in all methods. However, there are also systematic uncertainties, which are much less easy to quantify, but it is important because one object where all three techniques can be used gives three different spin values.

Clearly it is important to know which measurements are the most robust, and this depends on the black hole spectrum. Spectra which are dominated by the disk emission can give the same inner disk radius (so the same spin) for different mass accretion rates. However, the same radius is not always derived when the high-energy tail exists in the X-ray spectrum with more than $\sim 20\%$ of the total power. Therefore, robust spin estimation from disk continuum fitting requires that the spectrum is disk dominated. Conversely, the high-energy tail is required for reflection in order to have harder X-ray emission illuminating the disk. Unlike the disk continuum, the iron line and its associated reflected continuum are only a small fraction of the total flux, so a stronger tail gives better statistics to enable the small (5-10%) iron line to be constrained against the continuum. Unlike disk continuum fitting, the shape of the reflected emission does not depend on the distance to the source nor the black hole mass, which are sometimes poorly known. However, the reflected shape is dependent on more free parameters than that of the standard disk continuum model.

Using the fast timing QPO features then seems to offer a more model-independent way to constrain black hole spin of the galactic binary systems. However, while the timing features are independent of the spectral modeling, they are not independent of the specific QPO model assumed. Observational evidence in favor of a Lense-Thirring (vertical) precession origin for the low frequency QPO are accumulated, but the frequency depends on both spin and radius of the precessing material rather than spin alone. Combining this with that the high frequency QPOs potentially breaks this degeneracy, the spin value obtained depends on which high frequency oscillation mode is assumed to produce them, and this is not yet clear.

Thus we see observationally that the disk continuum fits can give robust results, but only for the subset of data where the spectra are disk-dominated. This is an issue for disk continuum fitting in Cyg X-1 as it never goes to a state where the high-energy tail is very low. Thus the very high spin of $a_* > 0.9$ measured in this system by disk continuum fitting, could depend on how the high-energy tail is modeled. Here we show new data from the Suzaku X-ray satellite where the high-energy tail is the weakest ever observed in Cyg X-1. We show that this spectrum gives the same high spin value as previous soft state datasets with stronger tail when we fit with the same continuum model of a standard disk and Compton tail from electrons with a non-thermal electron distribution. However, we get a significantly better fit for lower black hole spin if we allow an additional component between the disk and the high energy Comptonisation. This emission carries only $\sim 10\%$ of the total luminosity, and indicates a region which is optically thick, and fairly cooler than Comptonization corona, but hotter than the majority of the disk emission, and clearly thermal. This could be due to a hybrid thermal/non-thermal electron distribution, but the high optical depth more naturally connects this to the disk. This could be connected to a changing accretion disk structure during transitions, where the truncated disk models predict that the inner cool disk is reforming from the hot flow.

We show that the models with an additional thermal component is significantly better to explain the spectrum and confirmed the consistency by timing analysis. Fundamentally, disk continuum fitting assumes that the disk vertical structure is well described by the disk equations. This may not be true during the major hard-soft spectral transition, or whenever the inner disk is threaded by significant magnetic field.

Contents

List of Tables

List of Figures

Chapter 1

Introduction

1.1 Introduction

Cyg X-1 was the first black hole candidate to be identified, and thus is one of the best studied. However, it has some differences compared to the majority of black hole binaries in our Galaxy. It is a persistently bright rather than transiently. Even though the system has a high mass companion star, the mass accretion rate from this is probably not high enough for the disk to remain stable for purely Roche lobe overflow. Therefore, the disk is considered to be partly wind-fed.

While the resulting mass accretion rate onto the black hole is rather stable, its value is close to that of dramatic spectral transition, and thus, the system shows strong spectral variability. It switches between the low/hard Compton-dominated state and the high/soft disk dominated state, but with only a factor 2-3 change in overall luminosity. This is very different from transient systems, where the mass accretion rate rises dramatically from quiescence to outburst, and the state transition takes place. This may be the origin of the differences seen in the hard-to-soft spectral state change between Cyg X-1 and transient objects. The transients show a large-scale hysteresis, where the hard-to-soft transition during the rapid outburst rise can occur at a much higher (up to at least a factor of 10) luminosity than the reverse transition on the decline, and where the luminosity of the hard-to-soft transition itself is variable between different outbursts of the same source. By contrast, in Cyg X-1, the hysteresis is only small scale, with a luminosity change of less than a factor of 2–3, and the hard-to-soft transition luminosity is fairly stable.

It is not clear whether Cyg X-1 ever makes a complete state change since the spectrum in its high/soft state always has a fairly strong high-energy tail, and this tail shows different variability properties from those in the transient systems. If the transition is incomplete, the disk structure may be different from that of a standard high/soft state. This has important implications for measuring black hole spin from the disk emission, since this implicitly assumes that the disk structure is given by the standard Novikov-Thorne steady state equations. The fairly strong Comptonisation tail is another complicating factor in measuring spin. The disk emission has to be disentangled from the tail, and we need to consider photons lost from the disk by Compton scattering. These issues make the measurement of black hole spin of Cyg X-1 more difficult because the Comptonisation is known to be complex in the high/soft state. Previous spectral fits of Cyg X-1 X-ray emission required an additional soft Comptonisation component as well as a disk component and a high energy tail. However, this additional component was not considered in recent works to derive spin from disk emission fitting in Cyg X-1 in high/soft state, and they show extremely high spin of $a_* > 0.9$. This conflicts with some theoretical predictions of black hole spin of $a_* < 0.15$ for tidal locking scenario and CC-SASI scenario.

Here we show new data from Suzaku X-ray satellite where the high energy Compton tail is the weakest ever observed in Cyg X-1. This should gives us the best opportunity to study the intrinsic disk spectrum. Also we could obtain a significantly better fit by including an additional soft Comptonisation component of the

disk emission rather than by disk emission alone. We could not distinguish among models where this additional component originates from the disk structure during the transition or from the corona. These models gave significantly lower black hole spin. In conclusion, black hole spin of Cyg X-1 could not be robustly determined using current spectral models.

Chapter 2

Review of black hole binaries

2.1 Stellar mass black hole binary

2.1.1 Basic concept

"Event Horizon", which is discovered by Schwarzschild as an analytic solution of Einstein's equation of gravity (Schwarzschild 1916), is a special boundary supposed only some objects could produce it; when the object has a strong gravity under a large mass concentration in the small region. Their gravitational filed is so strong that, in the boundary, escape velocity is faster than the speed of light; nothing can escape. Such an object is named as a black hole by J. A. Wheeler in 1967 (Overbye 1991), and has been one of the most popular term and the most challenging issues in astrophysics.

The gravitational force is described with the Newtonian mechanics as

$$F_{\rm g} = \frac{GMm}{r^2} \tag{2.1}$$

, where G, M, m, r are the gravitational constant, the mass of the object producing the gravitational filed, the mass of the test particle, and distance between the object and test particle, respectively. The gravitational potential can be written as $-GM/r$, and the escape velocity of test particle is $v = \sqrt{2GM/r}$. This velocity will increase with the decreasing distance to the object, and reach the speed of light at the Schwarzschild radius ($R_{\rm S}$);

$$R_{\rm S} = 2R_{\rm g} = \frac{2GM}{c^2} = 2.9\Big(\frac{M}{M_\odot}\Big)\ [\rm km] \tag{2.2}$$

, where $M_\odot$ is the mass of Sun.

Schwarzschild assumed that there is an object of mass point, in the isotropic space-time and solved the Einstein equation, and obtained the relation between the time of the rest-frame of the test particle ($\rm d\tau$) and the time of the observer (located at the infinity from the mass point) frame (dt) as

$$d\tau = \Big(1 - \frac{R_{\rm S}}{r}\Big)^{1/2} dt \tag{2.3}$$

In the equation (2.3), in the case of $r > R_{\rm S}$, when the test particle is getting close to the object, the time (dt) of the observer frame is getting long. In the case of $r < R_{\rm S}$, the equation (2.3) will lose the physical meaning. Therefore, in other words, the objects within $R_{\rm S}$ can not escape. This $R_{\rm S}$ is called as the "Event Horizon". Black hole solution with the Einstein's equation can have three parameters; M (mass), J (angular momentum), and Q (electric charge). The Schwartzshild solution corresponds to the J=Q=0 (See §2.2).

2.1.2 Birth of a black hole in the universe

In the final stage of stars, some stars are thought to become compact objects of a white dwarf, a neutron star, or a black hole depending on the initial mass of the

star as shown in Figure 2.1 (e.g, Heger & Woosley 2002). There are two criteria to identify a compact object as a stellar mass black hole, a luminosity and a mass. To distinguish a black hole from a white dwarf, the mass is a useful criteria because a white dwarf can not have a mass exceeding the Chandrasekhar limit of $\simeq$1.4 $M_{\odot}$. Also to distinguish one from a neutron star, the mass is important to estimate. The maximum mass of a neutron is thought to be up to $\sim$2.9 $M_{\odot}$ (Kalogera & Baym 1996). Therefore, If the mass of the compact object is estimated to be higher than $\sim$3 $M_{\odot}$, we can confirm that the object is a black hole. Additionally, a luminosity also works for a criteria to identify a celestial object as a stellar-mass black hole when one assumes the binary system is shining at an Eddington limit (See §2.3.2).

The neutron stars are confirmed to be formed by supernova explosion because some neutron stars are found in the supernova remnant. While, the birth of black holes is still unveiled because ever discovered black hole binaries (See §2.4.1) do not associate a supernova remnant.

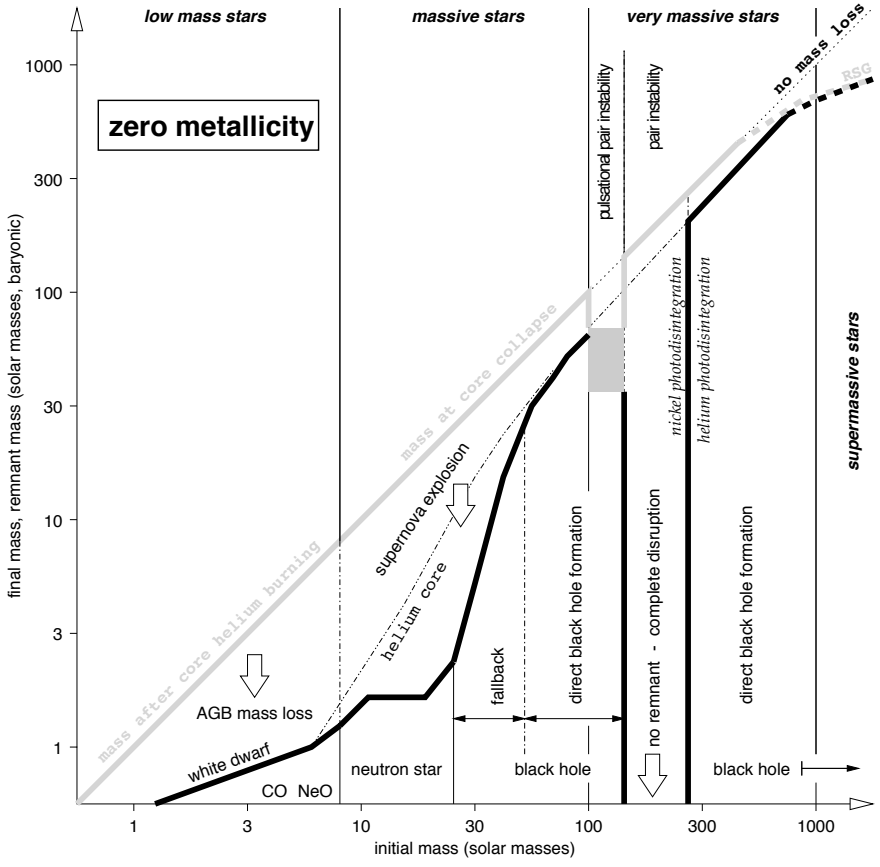

Figure 2.1: The initial-final mass function of non-rotating primordial stars. The horizontal axis shows the initial mass of stars. The vertical axis shows the final mass of collapsed object (black curve), and the mass of the star with out mass loss (Heger & Woosley 2002).

2.1.3 Discovery of the first black hole binary

The stellar-mass black hole can be observed in the electromagnetic wave only when it has a companion star; a black hole composes a binary system, and is gravitationally powered by mass accretion.

The first confirmed black hole binary of Cygnus X-1 (hereafter Cyg X-1) is known as one of the handful strong X-ray sources in the Galaxy since the early stage of X-ray astronomy, which has started in 1962 with rocket science. Oda et al. (1971) utilized *Uhuru*, the first X-ray satellite in history, and observed the short time-scale variability, less than 1 sec, from Cyg X-1 as shown in Figure 2.2. In this paper, they argued that

> *the rapid rotational period requires that the rotation star be a collapsed object, such as a neutron star or a black hole (Oda et al. 1971).*

To unveil the identification of a celestial object as a stellar-mass black hole, a mass is useful criterion (See §2.1.2). Here, we introduce an observational method to estimate masses of binary system. Considering a binary system:

$$a_1 + a_2 = a \tag{2.4}$$
$$M_1 a_1 = M_2 a_2 \tag{2.5}$$

, where a_1, a_2, are distances of a compact object and a companion star, respectively, from the center of mass, M_1 and M_2 are masses of the compact object and the companion star, respectively. Also, we introduce the total mass of M, and the total distance of a. When the spectral lines of a companion star can be observed, it is possible to estimate the the velocity projected onto the line of sight of K:

$$K = \frac{2\pi a_2 \sin i}{P\sqrt{1-e^2}} \tag{2.6}$$

, where P is the orbital period, i is the inclination angle of the binary plane, e is the eccentricity.

Using the Kepler's third law of $G(M_1 + M_2) = (2\pi/P)^2 a^3$, we can obtain a quantity

$$f \equiv \frac{M_1^3 \sin^3 i}{(M_1+M_2)^2} = \frac{K^3 P}{2\pi G}(1-e^2)^{3/2} \tag{2.7}$$

This formula is called as *mass function of f*, which is utilized to derive the mass of objects in a binary system, and calculated from observables K, P, and e.

The discovery of Cyg X-1 is the first scientific achievement to associate a black hole with an actual object. Following the *Uhuru* detection, the study of Cyg X-1 has been performed (e.g., review paper by Oda 1977). The radio counter part was found, also an optical companion star of HDE226868, 9.5 mag supergiant, was identified, leading to determination of the orbital period of P=5.6 day (Figure 2.3),

the Doppler velocity of K=75 km sec^{-1} and therefore, the mass function is estimated as $f = 0.22\ M_\odot$. In addition, owing to the optical estimation of $M_2 \sim 25\ M_\odot$, $i \sim 30°$, and $e \sim 0.06$, the mass of the compact object was constrained as $M_1 > 9.5\ M_\odot$ (Paczynski 1974). Thus, Cyg X-1 has been confirmed as the first black hole binary.

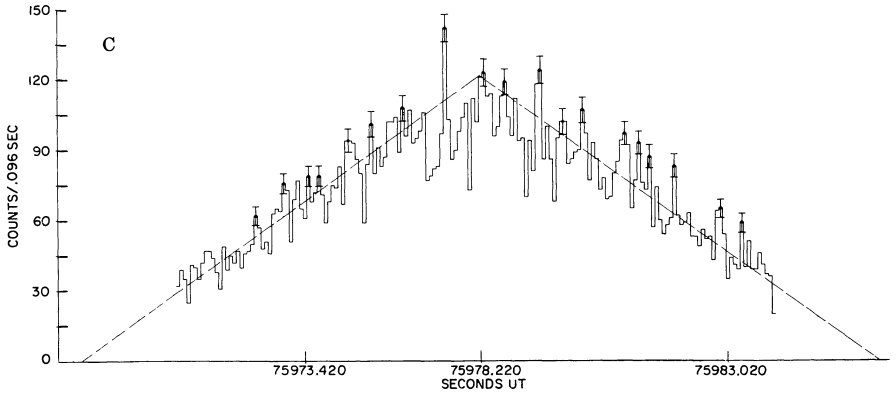

Figure 2.2: X-ray light curve of Cyg X-1 with bin size of 0.096 seconds observed by *Uhuru* satellite on 1971 March 6. The dashed line shows the time-dependent detector response (Oda et al. 1971).

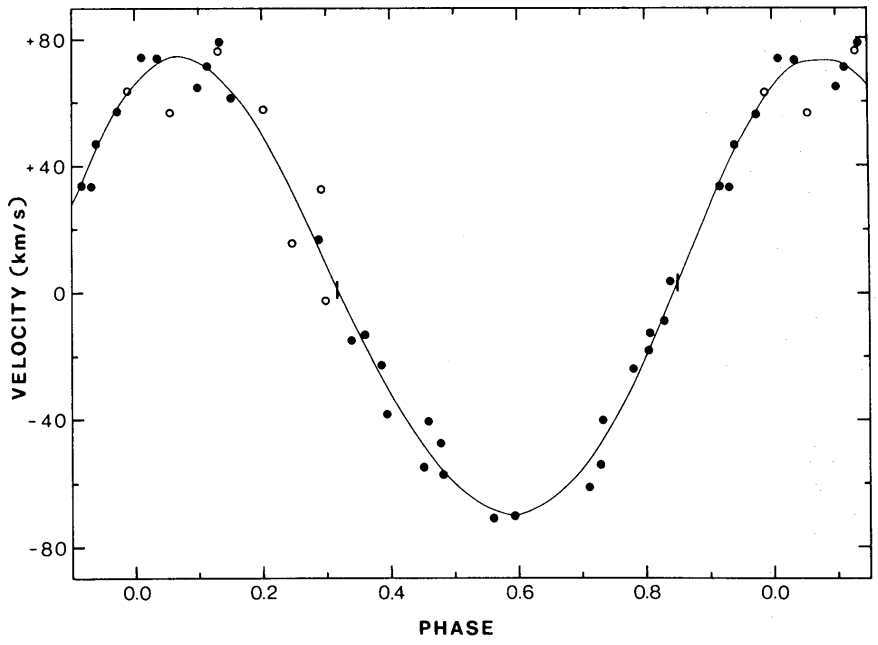

Figure 2.3: The absorption line velocity curve of HDE226868 folded with 5.6 days (Bolton 1975).

2.2 Spinning black hole

A black hole are thought to have three parameters (See §2.4.1). While in this thesis, we will focus on observable parameters with current observatories, mass and angular momentum. Thus, we assume a electric charge of black hole is zero. Actually, an electric charge is likely to be negligible in astrophysical contexts because it is shorted out by the surrounding plasma (Blandford & Znajek 1977).

In this section, we briefly introduce the concept of spinning black hole only with theoretical aspect. The observational results are summarized in §2.5.

2.2.1 Basic concept of Kerr black hole

The basic concept of the Kerr black hole is constructed in 1963 (Kerr 1963), and conventionally, we call "Schwarzschild black hole" for a non-spinning black hole, and "Kerr black hole" for a spinning black hole to distinguish whether spin is zero or not. The origin of the black hole spin is the angular momentum of the parent star (See §2.2.3 for detail). When the star gravitationally collapses (See §2.1.2), the stars rotate more quickly, following angular momentum conservation law. In this case, there are a lot of theorems, which guarantee the direct physical relevance of the Kerr spacetime, however, as the unique exact solution corresponding to stationary spinning black holes (Visser 2007). The spin parameter of a_* is written using angular momentum of J as

$$a_* = \frac{J}{J_{\max}} \tag{2.8}$$

$$= \frac{J}{GM^2/c} \tag{2.9}$$

Thorne (1974) gave the canonical upper limit of spin as $\sim$0.998, thus, $-0.998 \leq a_* \leq 0.998$. Typically in the case of accreting black hole, a positive spin value means the co-rotating accretion disk, and a negative value means counter-rotating one. However, it is important to note that all of the predicted and measured spin parameters are positive (Moreno Méndez & Cantiello 2016, also see §2.5). Even considering fully relativistic magnetohydrodynamic (MHD) accretion simulations, the value dose not change significantly (Gammie et al. 2004).

2.2.2 Blandford-Znajek process

The rotating black holes have a new concept of "ergosphere". In the region between outer ergosphere and outer event horizon any object can not stand stationary, however, can escape to infinity. This region is known as the "ergo region" as shown in Figure 2.4. When we suppose a Schwarzschild black hole, that is $a_* \to 0$, the stationary limit surface moves to over lie the even horizon and the ergo region disappears (Visser 2007).

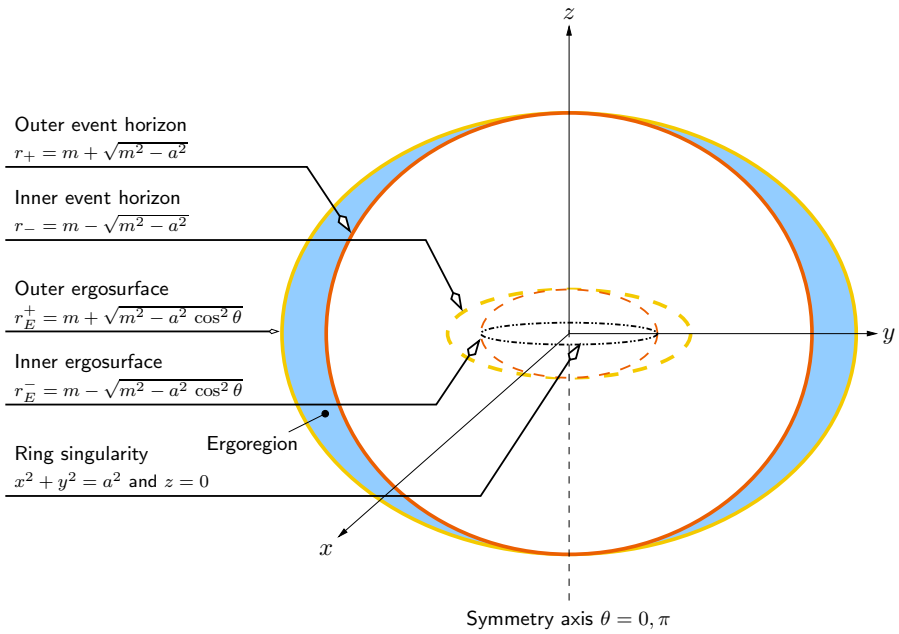

Figure 2.4: Schematic view of the horizons, ergosurfaces, and curvature singularity in the Kerr spacetime. When the limit of $a_* \to 1$, the stationary limit surface moves to over lie the even horizon and the ergo region disappears (Visser 2007).

Penrose process (Penrose 1969) claimed that when *negative* energy particles falls into the ergo region, the "outer region" could gain a *positive* energy. Following the theory, Blandford & Znajek (1977) proposed that the extracted *positive* energy from the Kerr holes via a magnetized plasma could be used to power a jet. Today, this theory seems to be the most plausible to construct relativistic jet in active galactic nuclei, gamma-ray bursts, and microquasars (McKinney & Gammie 2004). However, there are few direct observational evidence for such a link (See §2.5).

2.2.3 The natal spin and spin up

The origin of black hole spin is thought in the same way with rotating neutron stars (pulsars). When a neutron star is produced, and the spin period bacomes short enough (∼10 sec – 100 msec); a pulsar is born. The origin of the angular momentum of neutron stars is thought as followings;

- transportation of an angular momentum from a parent star
- affected by asymmetries of the core collapse supernova explosion
- spin up by accretion

The transportation of the angular momentum from the parent star has been studied (e,g, Heger et al. 2000; Suijs et al. 2008; Cantiello et al. 2014), however

the physics of transportation of internal angular momentum in stars is not yet understood. Though, generally, a star cannot have extremely high spin because of the equilibrium between its own gravity and centrifugal force.

The effects of asymmetries of the core collapse (CC) supernova explosion has been studied and they predicted that the effect is small (e.g., Moreno Méndez & Cantiello 2016). Moreno Méndez & Cantiello (2016) studied the CC-SASI (Standing Accretion Shock Instability) scenario, and predicted that the natal spin is $0.07 < a_* < 0.27$ for 1–5 $M_\odot$ black holes, and <0.15 for Cyg X-1, LMC X-1, and M33 X-7 (See Table 2.2 for physical parameters of these objects).

Axelsson et al. (2011) estimated that the upper limit of spin up is $a_* \leq 0.02$ in the case for Cyg X-1. The estimation of spin up based on the calculation that the mass accretion rate of $\dot{M}_{\rm capture} \sim 10^{-8}\ M_\odot\ {\rm yr}^{-1}$ and the age of the system of $\sim 7 \times 10^6$ yr, thus the black hole could gain an accreted mass of ∼0.1 $M_\odot$ since its formation (the total lost mass is ∼1 $M_\odot$), and the mass accretion could cause the $a_* \leq 0.02$.

Considering these effects to spin up, black hole spin seems not to be extremely high especially for stellar-mass black holes (Moreno Méndez & Cantiello 2016), and the theoretical predictions agree with some observational results, but argue against some ones (See §2.5).

2.2.4 The effect of black hole spin

The Figure 2.5 shows the ratio of electromagnetic to matter energy flux on the horizon based on the axisymmetric numerical simulations of a black hole surrounded by a magnetized plasma, where the plasma is described by the equations of general relativistic magnetohydrodynamics, and the effects of radiation are neglected. The solid line indicates numerical data, while the dotted line indicates a best fit of equation (2.10). We can see the effects of black hole spin become strong with spin over ∼0.8–0.9. While if black hole spin is less than ∼0.8, the effect is the same for any spin.

$$\frac{\dot{E}^{(EM)}}{\dot{E}^{(MA)}} \approx -0.068(2 - r_+)^2 \tag{2.10}$$

$$\dot{E}^{(EM)} : \text{Electromagnetic energy flux} \tag{2.11}$$

$$\dot{E}^{(MA)} : \text{Matter energy flux} \tag{2.12}$$

$$r_+ : 1 + \sqrt{1 - a^2} \quad \text{(Radius of the event horizon)} \tag{2.13}$$

$$\text{(in units of } c = G = 1) \tag{2.14}$$

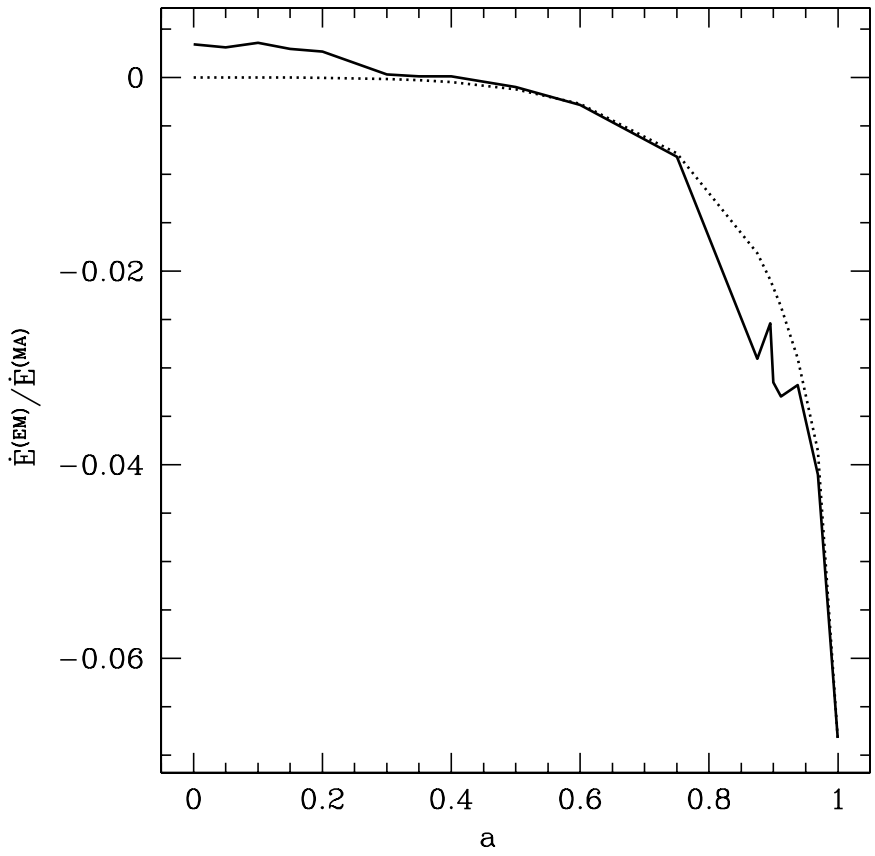

Figure 2.5: The ratio of electromagnetic to matter energy flux on the horizon based on the axisymmetric numerical simulations of a black hole surrounded by a magnetized plasma. $\dot{E}^{(EM)}$: Electromagnetic energy flux. $\dot{E}^{(MA)}$: Matter energy flux. (McKinney & Gammie 2004).

2.3 Accretion disk

2.3.1 basic concept of a disk

Gas around a compact object falls with the force of gravity. Usually accreting gas has angular momentum, and thus rotate around the compact object as accretion. Such a structure formed by accreting gas in the orbital motion around a compact object is called as an accretion disk.

The basic theoretical model has been advanced since 1950s, and the foundation framework greatly grew in 1970s. The accretion disk works as a converter of gravitational energy to radiant energy. To radiate effectively, a gas density should be high because the radiation efficiency is proportional to square of the density. To achieve the high density, the angular momentum need to be thrown away with the effect of a viscosity. When the angular momentum decreases, the gases will accrete to the compact object. Generally, spin speed, angular velocity, and angular momentum of a test particle with circular motion around mass point of M are written as

$$v_K = \sqrt{GM/r},\ \Omega_K = \sqrt{GM/r^3},\ \text{and}\ l_L \equiv r v_K = \sqrt{GMr} \tag{2.15}$$

, where r is the distance to M. This is called as Kepler rotation. The self gravity of disk is usually ignored. When viscosity works, the angular momentum is transferred to the outer side, and the gas accretes, Therefore, in other words, viscosity undertakes two roles; transportation of the angular momentum to the outer side, and conversion of gravitational energy to radiant energy.

2.3.2 Accretion disk models

There are lots of accretion disk models to explain the X-ray spectrum. We refer four accretion disk models widely used in the study of the X-ray spectrum; the standard disk (Shakura & Sunyaev 1973), the radiatively inefficient accretion flow (ADAF) (Yuan et al. 2003), the slim disk (Abramowicz et al. 1988), and the disk around Kerr black hole (Li et al. 2005).

Figure 2.6 shows the thermal equilibrium curve between the vertically-integrated surface density and the mass accretion rate (Abramowicz et al. 1995). The upper branch shows the advection-dominated accretion flow, and slim disk and standard disk are on the other equilibrium curve. Above the dotted lines denoted as $\tau = 1$ (τ is an optical depth) are the optically thin region. The parameters assumed to calculate the curves are a mass 10 $M_\odot$ and an inner disk radius $R_{\rm in}$ of 5 $R_{\rm g}$.

Standard accretion disk model

The "Standard" accretion disk model (α-disk model) was developed in the early 1970s owing to the theoretical efforts by Lynden-Bell, Pringle, Rees, Shakura, Sunyaev, Novikov, Thorne, and others. To introduce the model, we show some assumptions followings;

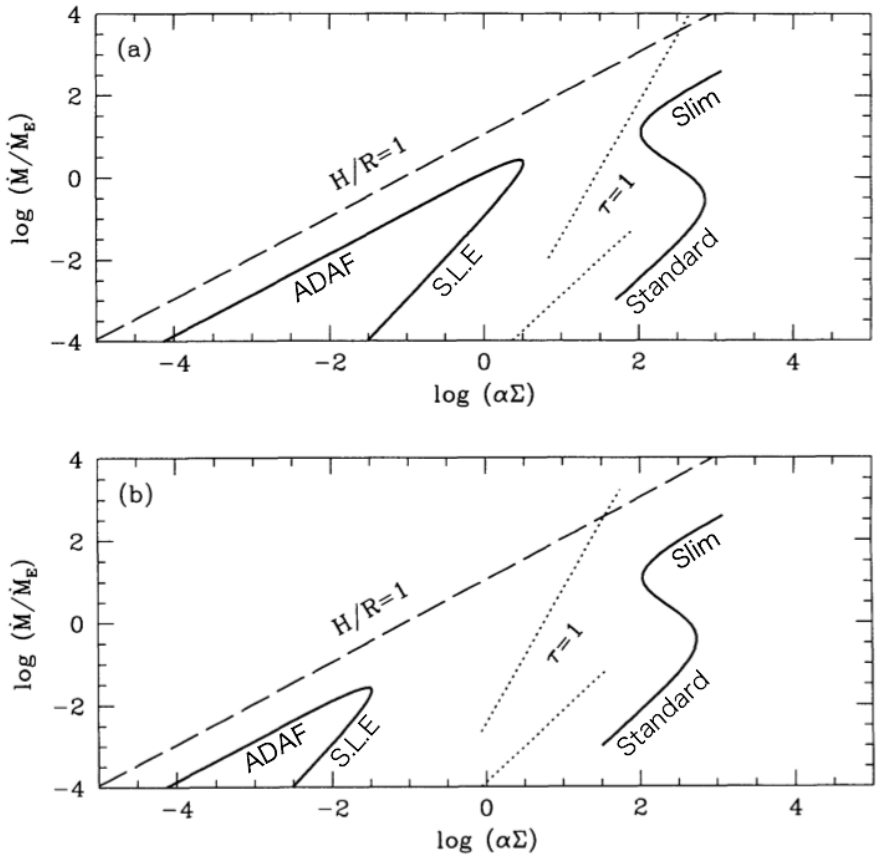

Figure 2.6: Top: The thermal equilibria between the vertically-integrated surface density and the mass accretion rate. The upper branches show advection-dominated accretion flow. Above the dotted lines (optical depth of $\tau = 1$) shows optically thin, thus the right solid S-shaped line is located optically thick region. The parameters assumed mass of 10 $M_\odot$, $R_{\rm in}$ of 5 $R_{\rm g}$. Bottom: The same as top panel but $\alpha = 0.01$ (Abramowicz et al. 1995).

- The mass and gravitational force of the disk is negligible.
- The disk exists in the plane of the equator of the black hole.
- The gas composing the disk rotates fast and accretes slowly to the black hole.
- The disk structure is axially symmetric.
- The disk is geometrically thin, and thus $H \ll r$, where H and r is thickness and radius of the disk, respectively.
- The disk is optically thick.
- The radiation of the disk is black body.
- The gas in the disk follow Keplerian rotation.
- Hydrostatic balance holds in the vertical direction.
- Magnetic field is negligible in the global system.
- The gravitational energy is transferred to the radiant energy efficiently
- The kinematic viscosity of ν is written as $\nu = \alpha c_{\rm s} H$, where $c_{\rm s}$ is a speed of sound and α is a dimensionless parameter of less than 1.

Here, we can obtain am important formula of energy flux (F) and distance to the black hole of r;

$$F \equiv \sigma T_{\rm s}^4 = \frac{3}{8\pi}\frac{GM\dot{M}}{r^3}\left(1 - \sqrt{\frac{r_{\rm in}}{r}}\right) \tag{2.16}$$

, where σ, $T_{\rm s}$, $r_{\rm in}$ are a Stefan-Boltzmann constant, the surface temperature of the disk, and the distance from inner edge of the disk to the black hole, respectively. This formula means the gravitational energy is transformed to the radiative energy efficiently because the left term shows the ratio of the radiative cooling, and the right term shows the release rate of the gravitational energy. The viscosity plays a important role to release the energy, but dose not appear in the formula. In the case of $r \gg r_{\rm in}$, we can see the relation of $T_{\rm s} \propto r^{-3/4}$, and the temperature is approximately written as $T_{\rm s} = T_{\rm in}(r/R_{\rm in})^{-3/4}$, where $T_{\rm in}$ is the temperature at the inner most radius.

Since we assume the surface temperature of disk depends on the radius and the radiation mechanism of each area are black body, the spectrum is expressed by a superposition of black bodies with various temperatures as shown in Figure 2.7. Therefore, it is called as the Multi-Color Disk (MCD) model. The MCD model basically well describes the actual X-ray spectrum (See §2.4.3).

If we compare accreting black holes with different M, it is convenient to scale with the Eddington luminosity, which is the maximum achievable luminosity of

radiation, expressed as The Eddington luminosity could be exceeded if the accretion flow is spherically asymmetric;

$$L_{\rm E} = 1.3 \times 10^{39} \Big(\frac{M}{10 M_{\odot}} \Big) \ {\rm erg \ sec^{-1}} \tag{2.17}$$

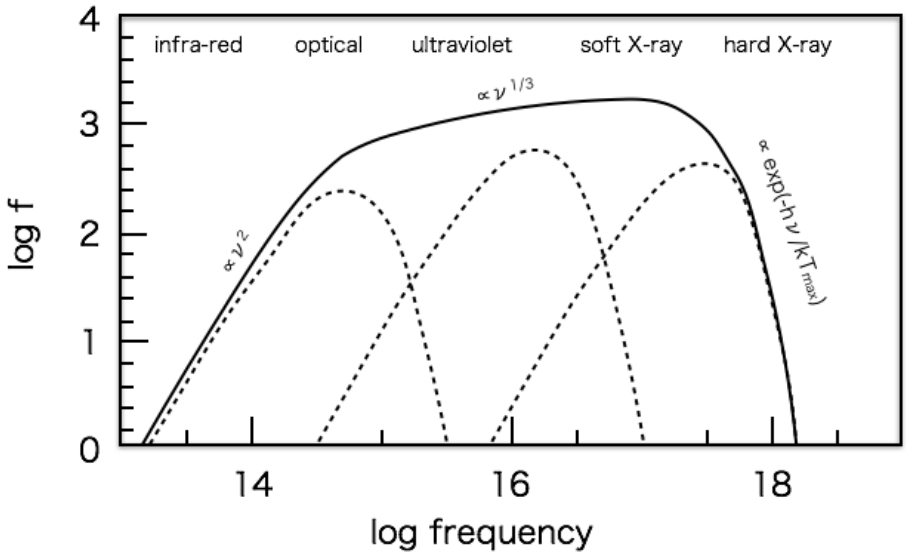

Figure 2.7: Typical spectrum of the standard disk in disk dominated state (high/soft state, See §2.4.3). The horizontal axis is the frequency and the vertical axis is observed flux in arbitrary units. In the high-frequency region, $\exp(-h\nu/kT_{\rm max})$ (Wien cut-off) appears because of the exist of the inner edge of the disk (See §2.3.3). In the low-frequency region, ν^2 (Rayleigh-Jeans slope) due to radiation from the outer radius of the disk. in the middle frequency, the flux follows $\nu^{1/3}$.

Until the gas reaches the inner edge (See §2.3.3), the half of potential energy is transformed to a radiative energy, and the other half transformed to a kinetic energy (Virial theorem). Thus, the luminosity of an accretion disk is written as

$$L_{\rm disk} \simeq \frac{1}{2} \frac{GM\dot{M}}{r_{\rm in}} \tag{2.18}$$

, where $\dot{M}$ is mass accretion rate. Therefore, the smaller $r_{\rm in}$, the larger energy would be radiated. On the other hand, the disk luminosity is described with energy conversion efficiency of η:

$$L_{\rm disk} = \eta \dot{M} c^2 \tag{2.19}$$

In the framework of general relativity, $\eta \sim 0.06$ for Schwarzschild black hole, and $\eta \sim 0.42$ for maximum rotating Kerr black hole. Considering the $\eta \sim 0.007$ of nuclear fusion of hydrogen, the efficiency of a disk is remarkable.

Furthermore, the disk luminosity is written with the innermost temperature and the innermost radius;

$$L_{\rm disk} = 4\pi R_{\rm in}^2 \sigma T_{\rm in}^4 \tag{2.20}$$

In the sense of observational aspects, the equation (2.20) is useful to study black hole binaries (See § 2.5).

Radiatively inefficient accretion flow model

Although the standard disk model has made great contributions to explain the disk structure, it cannot explain the high energy X-ray tail, rapid fluctuation, and so on. Thus, to explain the origin of the high energy X-ray tail, some accretion flow models are propounded in a complementary way. Today, Radiatively Inefficient Accretion Flow (RIAF) model is thought to be plausible. This model is based on the ADAF (Advection-Dominated Accretion Flow) model, and today, the inefficient radiation model is generally called RIAF model including ADAF model. In the RIAF model, the accretion flow is hot and its density is low, and thus it is less radiative. Less radiative means less radiative cooling, and thus accretion flow would be hotter. The maximum temperature of accretion gas can be estimated as a virial temperature;

$$T_{\rm vir} = \frac{2}{3}\frac{GMm_{\rm p}}{kr} \sim 4\times 10^{12}\frac{R_{\rm S}}{r}\ [K] \tag{2.21}$$

, where k, $m_{\rm p}$, and $R_{\rm S}$ are Boltzmann constant, mass of proton, and Schwarzschild radius (See §2.1.1). This formula says the viral temperature dose not depend on the black hole mass, and up to 10^{12} K (corresponding to ∼86000 KeV assuming black body radiation). However, as a result of Coulomb interaction of proton and electron, gas can be cool and the temperature would be around $\sim 10^{10}\ K$ (corresponding to hard X-ray region). Figure 2.8 shows the typical spectrum of ADAF disk (Manmoto et al. 1997), together with the spectrum of Sgr A*, which is the central core of the Galaxy and has a broad band wavelength radiation from radio to gamma-ray. ADAF model shows an energy break around $\sim 10^{20}$ Hz (corresponding to several hundred KeV).

When it has higher luminosity as a result of higher accretion rate, the density will increase and radiation will be efficient. In that case, the disk is not RIAF but the standard disk. The maximum luminosity of RIAF is estimated as the ∼10% level of Eddington limit. Then, we can draw a scenario with the standard disk model in the case of higher luminosity (soft spectrum, See §2.4.3), and RIAF model plays a role in the case of lower luminosity (hard spectrum, See §2.4.4). The comparison between standard disk and RIAF is summarized in Table 2.1

Slim disk model

The standard disk model cannot explain the case of not only low luminosity (See §2.3.2) but also high luminosity around Eddington limit. In the case of higher

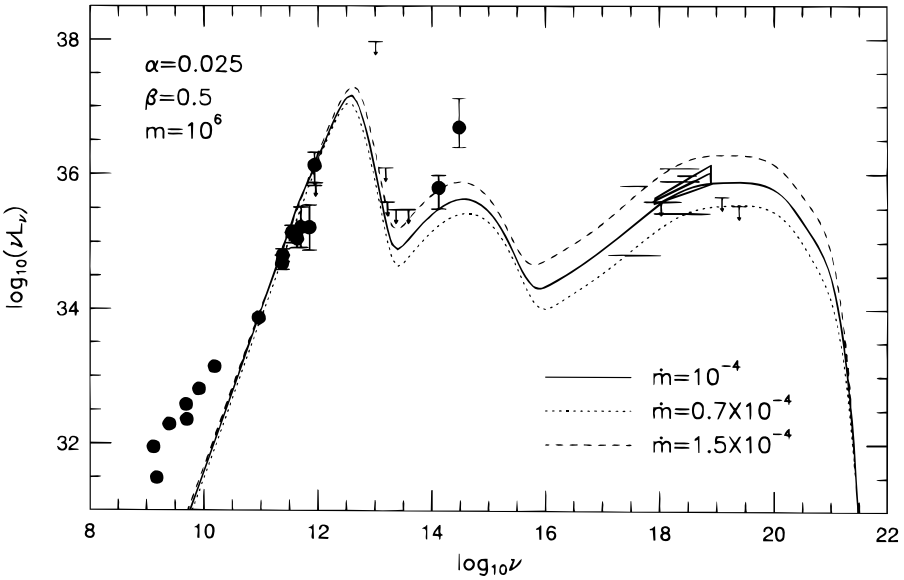

Figure 2.8: The spectrum of Sgr A* (the central core of the Galaxy). In the low energy region (radio region), the spectrum shows Rayleigh-Jeans radiation. The Compton scattering component of the low energy photon create the central mountain structure. Further Compton component and the thermal bremsstrahlung cause the X-/gamma-rays (Manmoto et al. 1997).

accretion rate, the accretion flow has a higher optical depth and created photons would repeat scattering and absorption. Then, it could be difficult to escape from the disk. Therefore, the photons accrete to the black hole with the accretion flow, and the transfer efficiency of the gravitational energy to the radiation gets worse.

Following the standard disk model, the slim disk model is propound (Abramowicz et al. 1988). In the sense of difficulty to escape from the disk, the spectrum is similar to the standard model but slightly modified from the standard model (Figure 2.6).

Disk around Kerr black hole

The radius of ISCO with Kerr black hole can be smaller than Schwarzschild black hole (See §2.3.3), thus the energy flux from disk will be larger (See equation 2.16). Therefore, the shape of spectrum would be changed depending on the spin parameter.

Figure 2.9 shows the thermal spectrum with different spins. Left panel corresponds Schwarzschild black hole, and right panel does Kerr black hole. The Kerr black hole can gain an additional inner component of the disk, which shows a higher energy segment in the spectrum. Because of Keplerian rotation of the disk, inner part of the disk has higher velocity and thus the Fe-K line becomes broader. See also §2.5 for review of previous results to estimate spin parameters.

Table 2.1: The comparison between the standard disk and RIAF (Radiatively Inefficient Accretion Flow) model.

parameters	standard disk	RIAF
disc structure	axial symmetric	axial symmetric
accretion flow	slow accretion	rapid accretion helically
velocity of disk rotation	Keplerian rotation	slower than Keplerian rotation
transfers of the gravitational energy	black body	synchrotron radiation Compton scattering thermal bremsstrahlung
viscosity	α model	α model
maximum temperature	$\sim 10^7 M_1^{-1/4}$ K	ion/electron temperature $\sim 10^{12}$/ $\sim 10^9$ K
luminosity	$\propto$ accretion rate	$\propto$ (accretion rate)^2
geometry thickness (H) of the disk	H$\ll$r	H$<$r
optically thickness (τ) of the disk	$\tau > 1$	$\tau < 1$

2.3.3 Innermost stable circular orbit

The innermost stable circular orbit (ISCO) is the minimal radius where the accretion disk can have a stable circular motion. For the Schwarzschild black hole, the radius of ISCO is equal to $6R_{\rm g}$ (Kaplan 1949), where $R_{\rm g} = 3R_{\rm S} = 6GM/c^2$ (See §2.1.1). For the Kerr black hole (Kerr 1963), the calculation of the ISCO is much more complicated because of more complex general relativity equation. In this subsection, we refer various estimations of radius of ISCO in theoretical method, and observational approach. In the observational approach, it is strongly related with the estimation of black hole spin, and thus we give only introduction and other details are given in §2.5.

A radius of ISCO depends on the spin of black hole and rotation direction of orbital motion of test particle (e.g., Jefremov et al. 2015, and references there in). Here we use the unit of $G = c = 1$; $R_{\rm g} = M$ and other physical quantities of dimensionalities: $[L] = [M]$, $[J] = [M]$, $[E] = 1$, $[a_*] = [M]$, $[s] = [M]$.

Figure 2.10 shows radii of ISCO with different direction of motion and spin of test particles (Jefremov et al. 2015). There are six cases denoted as A, B, C, D, E, and F which represent different spin and orbital motion of test particle. Primes represent a different spin of black hole; for $a_* = 0$ (Schwarzschild black hole), just letters are used (e.g., A), for $a_* \ll M$, primes is used (e.g., A$'$), for $a_* = M$, double primes are used (e.g., A$''$). The direction of particle's spin is shown by an arrow on a circle; clockwise arrow (C and F) means particles co-rotating with black hole,

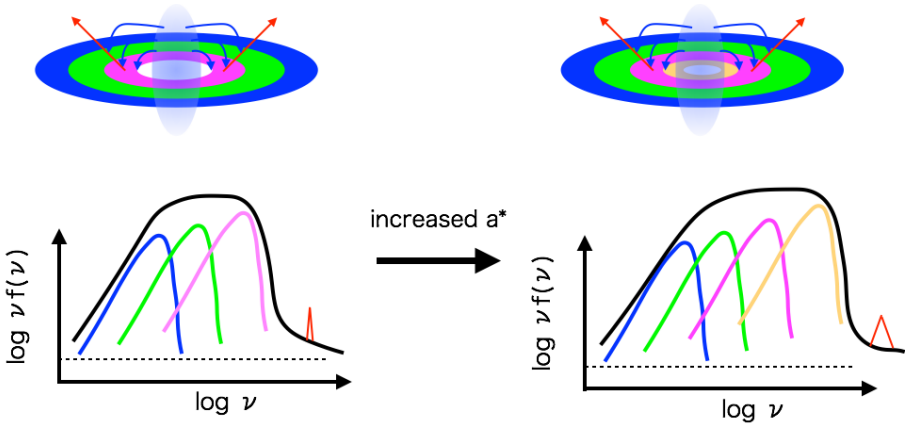

Figure 2.9: Thermal spectrum with different spin. Left panel corresponds Schwarzschild black hole, and right panel is Kerr black hole. Additional inner component (yellow) of the disk with Kerr black hole is corresponding to higher energy component in the spectrum. Because of Keplerian rotation of the disk (See § 2.3.2), inner part of the disk has higher velocity and thus the Fe-K line (red) becomes broader.

anti-clockwise arrow (D and E) means counter-rotating, for spin less particles (A and B) arrow is not used. The direction of the orbital motion of test particle is shown by straight arrow outside circles. The size of black hole is shown for the case of the extreme spin. In the case of a Schwarzschild black hole, the radii of ISCO for spin less particles equals to $6M$, independently of direction of orbital motion (A and B). In the case of a Kerr black hole, the radii of ISCO depends on the direction of orbital motion. For slowly rotating black hole, $a_* \ll M$; counter-rotating particle A$'$ has an orbit with $r_{\rm ISCO} > 6M$, co-rotating particle B$'$ has an orbit with $r_{\rm ISCO} < 6M$. For the extreme Kerr black hole, $a_* = M$, a counter-rotating particle A$''$ has an orbit with $r_{\rm ISCO} = 9M$, a co-rotating particle B$''$ has an orbit with $r_{\rm ISCO} = M$. Presence of spin increases or decreases the ISCO radius in comparison with spin less case, as shown in the case of particles C, D, E, F (also C$'$, C$''$ and so on). Remind that z-axis is directed along the rotation axis of black hole, so $a_* > 0$. The particles C and D (also E and F) have the same radius of ISCO in the case of Schwarzschild black hole, while they have a different radius of ISCO in the case of Kerr black hole. For the extreme Kerr BH particles B$''$, D$''$, F$''$ have the same radii of ISCO.

The spin parameter with the counter-rotating particle is usually expressed as a negative value. However, to date, all of the predicted and measured spin parameters are positive (Moreno Méndez & Cantiello 2016, also see §2.2 and §2.5).

In the observational aspects, the existesnce of ISCO is successfully demonstrated for some black hole binaries. Figure 2.11 shows the first determination of the time evolution (∼10 days) of the measured inner radius of GX 339−4 observed by *Tenma* satellite (Makishima et al. 1986). The inner radius is remained remarkably constant while the power-law flux has changed. Figure 2.12 shows the long-term history of

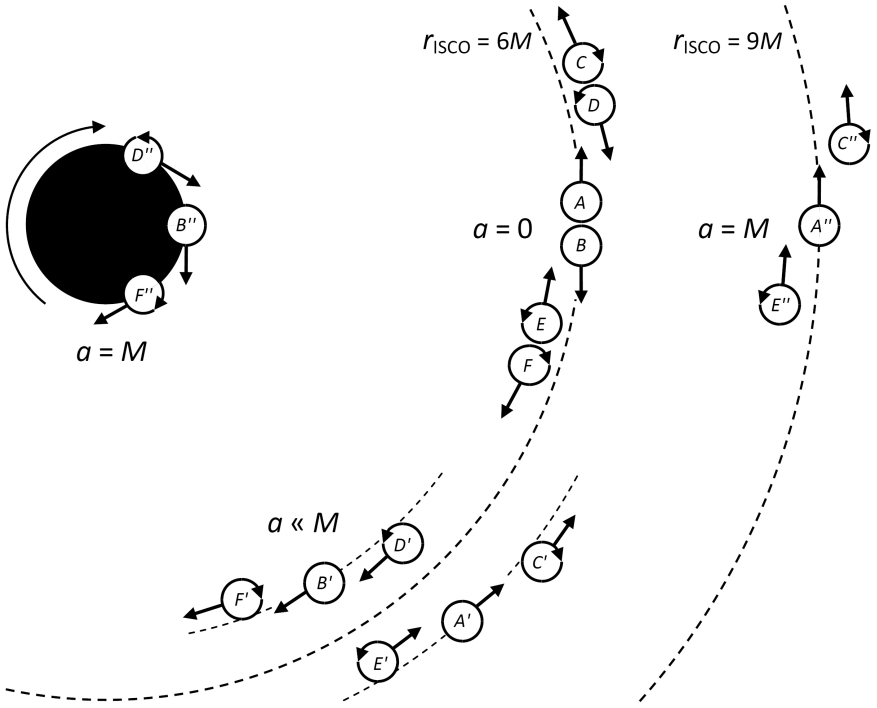

Figure 2.10: The radii of ISCO with different direction of motion and spin of test particles (Jefremov et al. 2015).

measured $r_{\rm in}$ of LMC X-3, observed by eight observatories ($RXTE$, $Suzaku$, $Swift$, $XMM-Newton$, $BeppoSAX$, $ASCA$, $Ginga$, and $EXOSAT$) over ∼30 years. The $R_{\rm in}$ is obviously constant (Steiner et al. 2010).

Figure 2.13 shows the relation between the mass and the inner radius (Makishima et al. 2000). Here, the mass is estimated by optical measurements, while the inner radii are estimated by X-ray observations. The three HMXBs of Cyg X-1, LMC X-1, LMC X-3 (See Table2.2 for physical parameters of these objects), and a transient object of GS 2000+25 show $R_{\rm in} = 6R_{\rm g}$ within errors; in other words, the spin parameter of these objects are close to $a_* = 0$. On the other hands, $R_{\rm in}$ of other sources are less then that of $R_{\rm in} = 6R_{\rm g}$, and thus these binaries are suggested to contain Kerr black holes. Therefore, the X-ray measurements support the existence of the last stable orbit. Furthermore, the result shows X-ray measurements could constrain the spin parameter (See §2.5 for detail about spin estimation).

2.3.4 Typical time scale an accretion disk

There are three important time scales of an accretion disk; the dynamical time scale of $t_{\rm dyn}$, the thermal time scale of $t_{\rm th}$, and the viscous time scale of $t_{\rm vis}$. While the $t_{\rm vis}$ shows a typical time scale of radial disk inflow, $t_{\rm th}$ shows that of thermal processes. These three time scales are not independent, but they are related to one another;

$$t_{\rm dyn} = \frac{1}{\Omega_K} \sim \alpha t_{\rm th} \sim \alpha\Big(\frac{H}{r}\Big)^2 t_{\rm vis} \tag{2.22}$$

, where $\Omega_K = \sqrt{GM/r^3}$, and α is viscosity (See §2.3.2).

The $t_{\rm vis}$ is numerically given;

$$t_{\rm vis} \sim 1.5\Big(\frac{\alpha}{0.1}\Big)^{-1}\Big(\frac{H}{r}\Big)^{-2}\Big(\frac{r}{100r_{\rm g}}\Big)^{3/2}\Big(\frac{M}{10M_\odot}\Big)\ {\rm sec} \tag{2.23}$$

Since H/r is small, the $t_{\rm vis}$ would be ∼ a day with a black hole of 10 $M_\odot$.

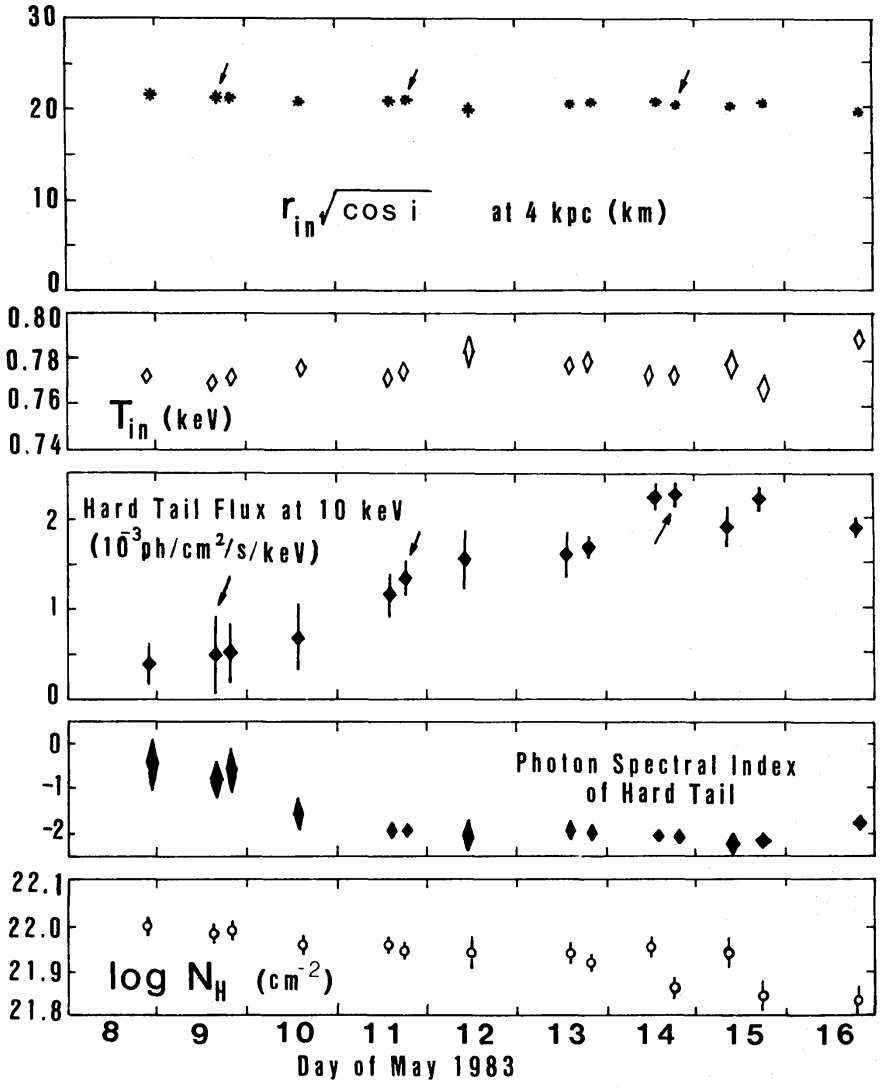

Figure 2.11: Half-day averaged of the spectral parameters; $r_{\rm in}\sqrt{\cos\,i}$ assuming $d =$ 4 kpc, the disk temperature, the card tail flux (assuming power-law model) at 10 keV, a hat-tail photon index, and a log common density (Makishima et al. 1986).

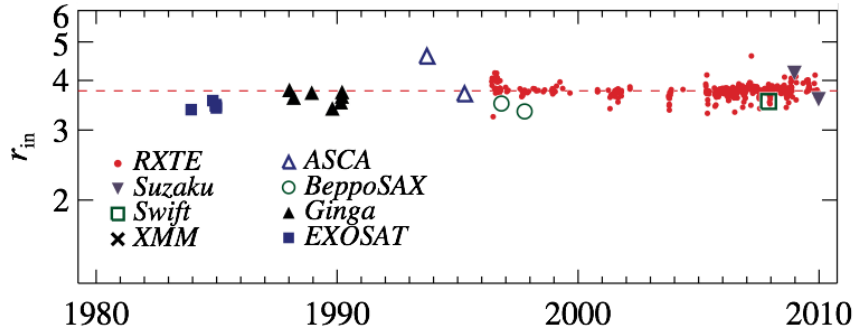

Figure 2.12: The long-term history of the inner radius of LMC X-3 observed by eight observatories. The dashed line is corresponding to the center of the RXTE data (red circle). The $R_{\rm in}$ is shown in $R_{\rm g}$ unit (Steiner et al. 2010).

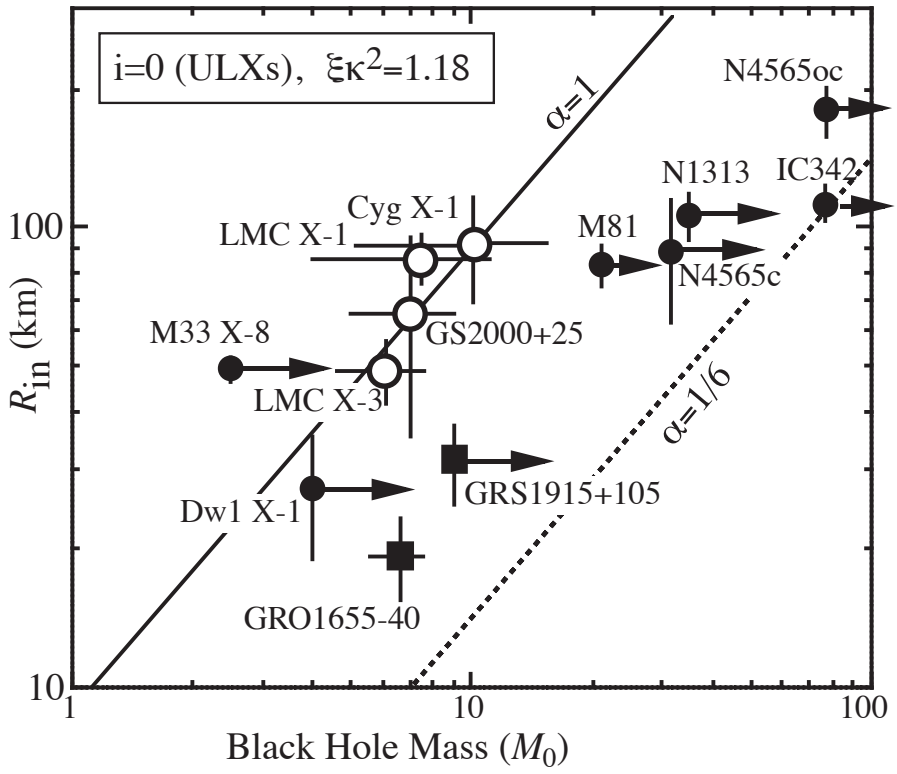

Figure 2.13: The relation between $R_{\rm in}$ and black hole mass. Here, $\alpha = 1$ is corresponding to the ISCO of Schwarzschild black hole, and $\alpha = 1/6$ is that of extreme Kerr blak hole (Makishima et al. 2000).

2.4 X-ray properties of black hole binary

2.4.1 Black X-ray binaries

After Cyg X-1, ∼20 black hole binaries are found in our Galaxy. Most of them are transient systems; a X-ray spectral and temporal property vary with time dramatically. Furthermore, the optical counterparts have been identified for most of them. During the X-ray faint period, the optical spectral observations have been conducted to estimate the mass of a star (equation 2.7) without contamination of emission from an accretion disk.

The size of a compact object is small, and usually it cannot fill its Roche lobe in their binary system, and only a companion star could fill one. Almost all of Galactic X-ray binaries appear to fall into two distinct groups; the high-mass X-ray binaries (HMXBs) and the low-mass X-ray binaries (LMXBs). In HMXBs, a compact object is fed through powerful stellar winds from a companion star as shown in Figure 2.14 right. While, in the case of LMXBs, a compact object is surrounded by an accretion disk, which is provided by Roche lobe overflow (left panel in Figure 2.14).

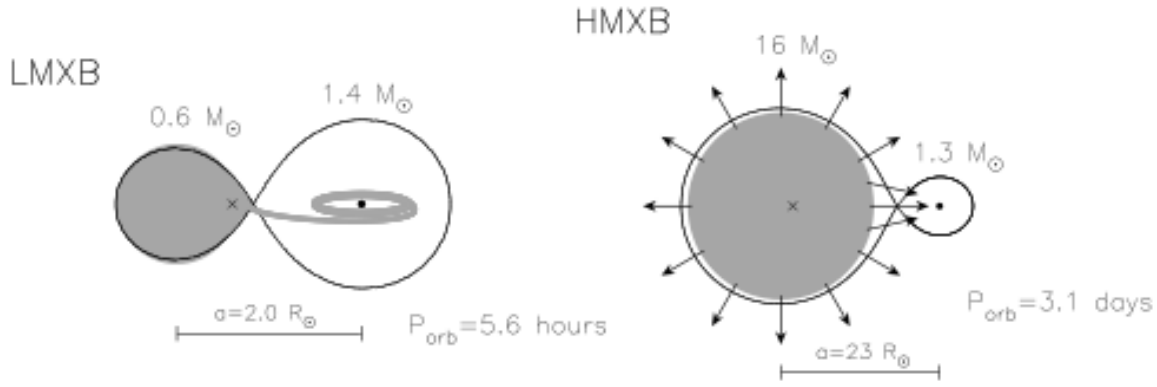

Figure 2.14: Schematic pictures of a low mass X-ray binary (left), and high mass X-ray binary (right) (Tauris & van den Heuvel 2006).

Figure 2.15 shows schematic sketch of 16 black hole binaries in the Milky Way Galaxy. Some of them are long-period systems containing hot or cool supergiants (Cyg X-1 and GRS 1915+105) and most of other systems contain K-dwarf companions (Remillard & McClintock 2006).

Only two high-mass black hole binaries of Cyg X-1 and SS 433 are listed in *Catalogue of high-mass X-ray binaries in the Galaxy (4th edition)*, while totally 114 HMXBs in the Galaxy are cataloged (Liu et al. 2006). Cyg X-1 is the only one persistently bright black hole binary in the Milky Way Galaxy, and totally four persistently bright black hole binaries are found. Two persistently bright black hole binaries are in the Large Magellanic Cloud, LMC X-1 and LMC X-3. M33 X-7 is observed in the nearby spiral galaxy Messier 33 (NGC 598) at 840 kpc. The

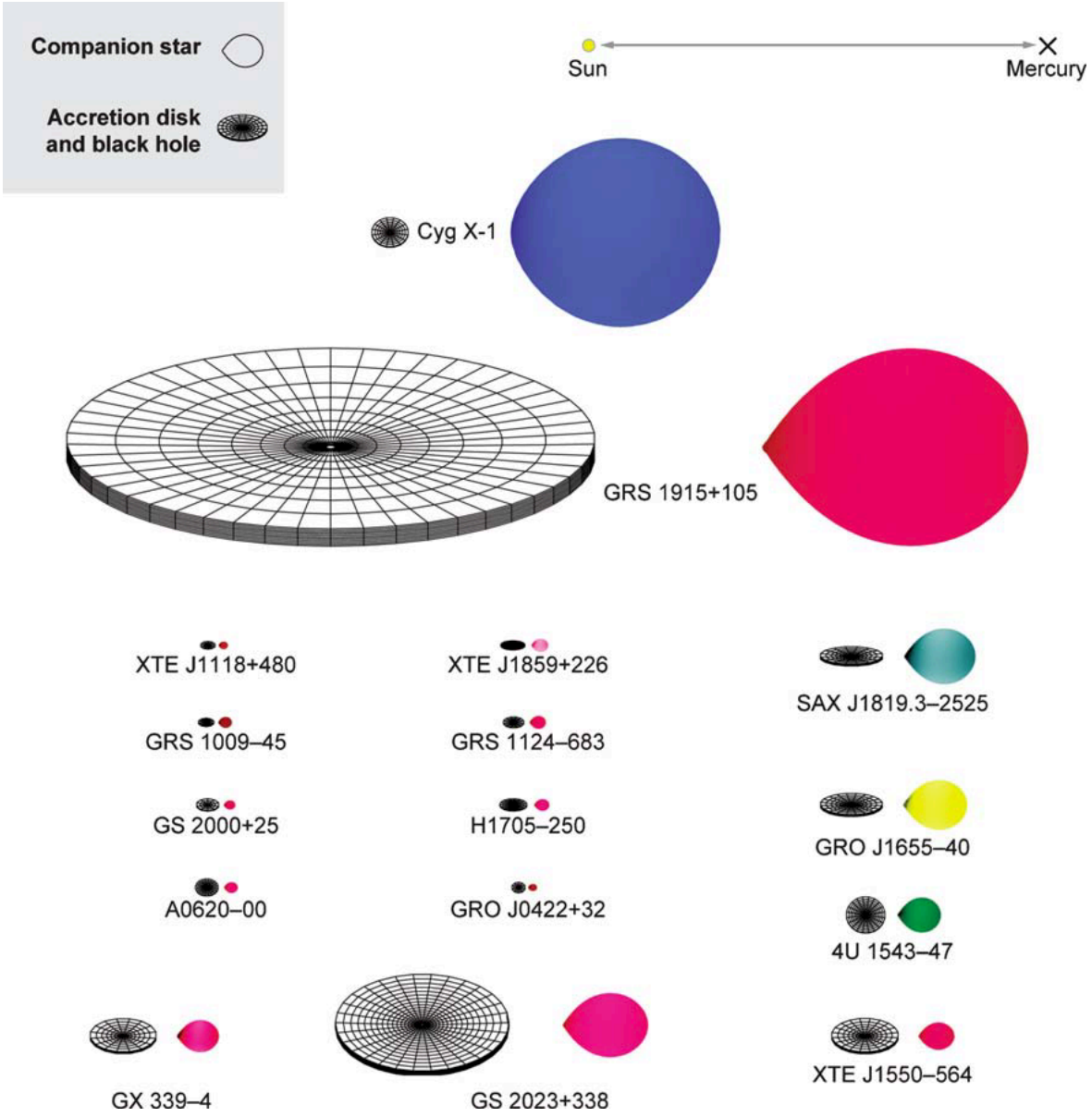

Figure 2.15: Scale drawings of 16 black-hole binaries in the Milky Way Galaxy. The Sun-Mercury distance of 0.4 AU is shown at the top. The estimated binary inclination is indicated by the tilt of the accretion disk. The color of the companion star roughly indicates its surface temperature (Remillard & McClintock 2006).

Table 2.2: The basic parameters of high mass black hole binaries.

Name	D [kpc]	i [deg]	P [day]	f [$M_\odot$]	M_1 [$M_\odot$]	Star	References
Cyg X-1	$1.86\ ^{+0.12}_{-0.11}$	$27.1^{+0.8}_{-0.8}$	5.6	$0.244^{+0.05}_{-0.05}$	$14.8^{+1.0}_{-1.0}$	O9.7Iab	3, 4, 7, 9
LMC X-1	$48.10^{+2.22}_{-2.22}$	$36.38^{+2.02}_{-2.02}$	3.9	$0.14^{+0.05}_{-0.05}$	$10.91^{+1.41}_{-1.41}$	O7III	4, 6
LMC X-3	$48.10^{+2.22}_{-2.22}$	69.24±0.72	1.7	$2.3^{+0.3}_{-0.3}$	$6.98^{+0.56}_{-0.56}$	B3V	4, 6, 8
SS 433	$5.5^{+0.2}_{-0.2}$	78.8	13.0	0.46	9	A5/A7	1,2
M33 X-7	840±20	74.6±1.0	3.45	0.46±0.08	15.65±1.45	O7III/O8III	5

[1] Blundell & Bowler (2004), [2] Cherepashchuk et al. (2005), [3] Gies et al. (2008)

[4] McClintock & Remillard (2006), [5]Orosz et al. (2007)

[6] Orosz et al. (2009), [7] Orosz et al. (2011), [8] Orosz et al. (2014), [9] Reid et al. (2011),

black hole mass of this system is the highest among stellar black holes ever observed ($\sim$16 $M_\odot$). M33 X-7 is also persistently bright, and it is interesting to note that it shows eclipse (Pietsch et al. 2004, 2006; Orosz et al. 2007). The basic parameters of these five black hole binaries are listed in Table 2.2. The other black hole binaries are transient. One exception is GRS 1915+105 which remains bright since it erupted on August 1992.

2.4.2 State transition

To describe the variable spectrum of black hole binaries, several distinct spectral states, which are caused by different physical properties of accretion flows around black holes (Esin et al. 1997, See also §2.3), are propounded (e.g., Nowak 1995; Tanaka & Shibazaki 1996; Esin et al. 1997; Zdziarski et al. 2002; Remillard & McClintock 2006; Done et al. 2007). There are two main states, a high/soft state and low/hard state, and some more spectral states to distinguish; e.g., very high state, ultra soft state, intermediate state, and quiescent state.

The left panel of Figure 2.16 shows the X-ray spectrum of GRO J1655−40 taken from the 2005 outburst in the very high state, the low/hard state, the high/soft state, and the ultra soft state (Done et al. 2007). That of middle and right panels show how accretion flow changes to explain these different spectra, with differing contributions from the disc, hot inner flow and its associated jet, active regions above the disc and a wind (Esin et al. 1997; Done et al. 2007).

Figure 2.17 shows the broad band spectra in several distinct spectral states of Cyg X-1 (Zdziarski et al. 2002); the black and blue spectra show the hard state (*Ginga* and *CGRO*/OSSE spectrum on 1991 June 6th, *BeppoSAX* spectrum on 1998 May 3-4th), the cyan spectrum shows the hard state spectrum which was

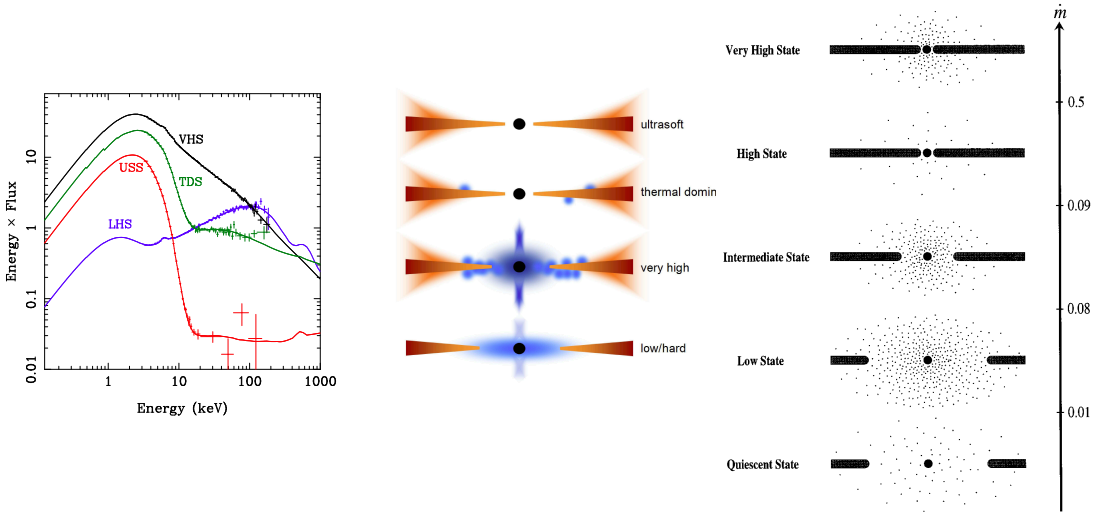

Figure 2.16: Left: The X-ray spectrum of GRO J1655−40 taken from the 2005 outburst in very high state (black), the low/hard state (blue), the high/soft state (green), and ultra soft state (red). Middle: Proposed accretion flow changes to explain these different spectra, with differing contributions from the disc, hot inner flow and its associated jet, active regions above the disc and a wind (Done et al. 2007). Right: Schematic picture of configuration of the accretion flow in different spectral states as a function of the total mass accretion rate of $\dot{m}$ (Esin et al. 1997).

substantially softer than the other hard state spectra (*BeppoSAX* spectrum on 1996 September 12nd), the green spectrum shows the intermediate spectrum (*RXTE* spectrum on 1996 May 23rd), the red and magenta spectra shows the soft state (*CGRO*/OSSE and COMPEL spectra from 1996 June 14-15th, *ASCA* and *RXTE* spectrum of 1996 May 30-31st), respectively. Comparing the spectra of Cyg X-1 with GRO J1655−40 (Figure 2.16, 2.17, and 2.19), we can see the spectrum of Cyg X-1 in the soft state has a stronger hard tail component than GRO J1655−40.

2.4.3 High/soft state

In the high/soft state, the luminosity is ∼1-10% level of Eddington limit, where the X-ray spectrum is dominated by a soft X-ray component below ∼10 keV. The soft component is well described by the standard disk model (Shakura & Sunyaev 1973, See also §2.3.2), and the characteristic temperature is ∼1 keV (Tanaka & Shibazaki 1996). Additionally, a hard tail component, which is well described with power-law with a photon index of ∼2, is often observed above ∼10 keV (e.g., Figure 2.16, 2.17, 2.19). This tail is quantitatively understood as a Comptonization of the disk emissions (Figure 2.16). The total luminosity in the soft state exceeds the low/hard state (described bellow), and thus the state is said as “high” “soft” state.

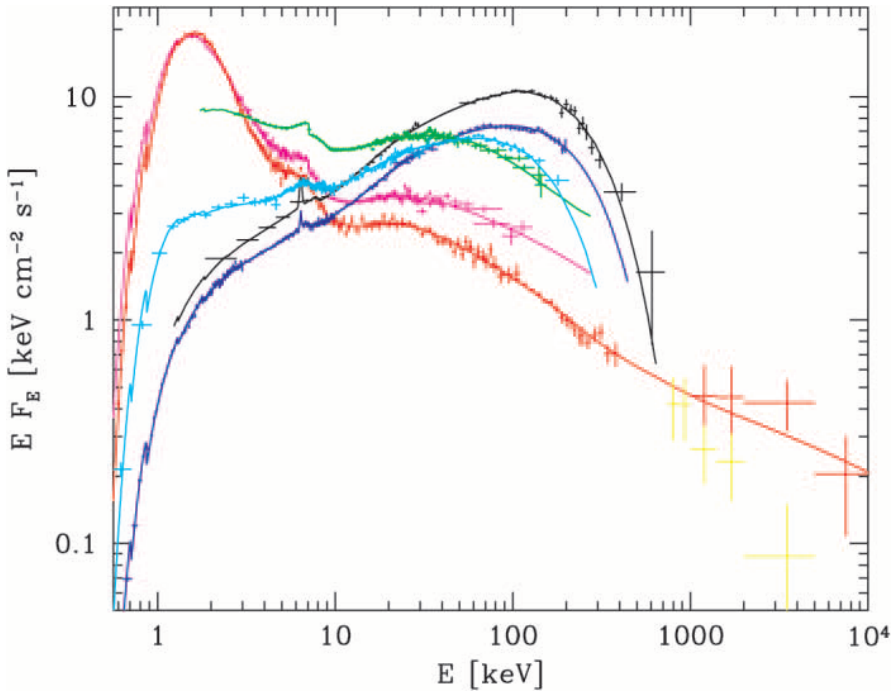

Figure 2.17: The broadband spectrum of Cyg X-1 (*Ginga*, *BeppoSAX*, *CGRO*/OSSE and COMPTEL, *ASCA*, *RXTE*/PCA,). The black and blue spectra show the hard state, the cyan spectrum shows hard state spectrum but substantially softer than the other hard state spectrum, the green spectra shows the intermediate spectra, the red and magenta spectrum show the soft state, respectively. The spectrum of Cyg X-1 always show the stronger tail (Zdziarski et al. 2002).

2.4.4 Low/hard state

In the low/hard state, the spectrum is approximately represented by the power-law with a photon index of ∼1.5-2.0, and has an exponential cutoff around 100 keV (Sunyaev & Truemper 1979). The spectral shape is generally described by the unsaturated Compton scattering of the X-ray photons from the accretion disk by thermal electrons in hot inner flow or corona (Figure 2.16). The total luminosity is generally $\sim 10^{-8} - 1\%$ level of the Eddington luminosity (Nowak 1995), and thus the state is said as "low" "hard" state. In the hard state, the standard disk component is too faint to observe, and the temperature of the inner disk is lower than that in the high/soft state. Thus, it is hard to determine the inner disk radius by observations of the disk. Therefore, in such a case, another approach of utilizing of the reflection components originated from the inner parts of the disk is useful to estimate the inner disk radius.

The fluorescent lines of the iron-K lines at 6.4 keV and a significant K absorption edge of iron ∼7.1 keV appear in the low/hard state, and these features are caused by a reflection of X-rays by a cool disk. Figure 2.18 shows the iron line profiles in various conditions (Laor 1991). The line emissions from the vicinity of the black holes are expected to be broadened by doppler shift and gravitational redshift, depending on where the lines are produced (Fabian et al. 1989; Laor 1991). These structures could be a good tracer of the inner edge of the disk (e.g., Ebisawa et al. 1991; Ueda et al. 1994), though the technique to utilize a emission lines for the tracer of the inner edge of the disk in the low/hard state is still controversial.

There are some results to argue that the inner radii of the disk of several black hole binaries, which is including GX 339−4 and GRO J1655−40, are continued to the ISCO in the low/hard state utilizing the broadened iron-K lines (e.g., Miller et al. 2006; Reis et al. 2010). However, some previous results suggested that the inner radius of the disk does not extend to the ISCO in the low/hard state (e.g., Tomsick et al. 2009; Shidatsu et al. 2011; Kolehmainen et al. 2014). Especially, Done & Diaz Trigo (2010) showed that the disk is truncated over 20 R_g by the re-analysis results of GX 339−4 in low/hard state. We note that reflection fits generally give an extremely high spin for GX 339−4 (e.g. Ludlam et al. (2015) but see Kubota & Done (2016), also See §2.5). What is more, today, the picture of the truncated disk in the low/hard state is popular to understand the property of black hole binaries (Figure 2.16).

2.4.5 State transition signature in Optical

As described in §2.4.1, the accretion flow comes from a companion star, and it is natural to assume that such a state transition is associated with a redistribution of the circumstellar matter in the system (Čechura et al. 2015). The optical data show that the properties derived by Doppler tomography of Hα, which can resolve accretion flows in binaries, is relating with X-ray spectral transition (Čechura et al.

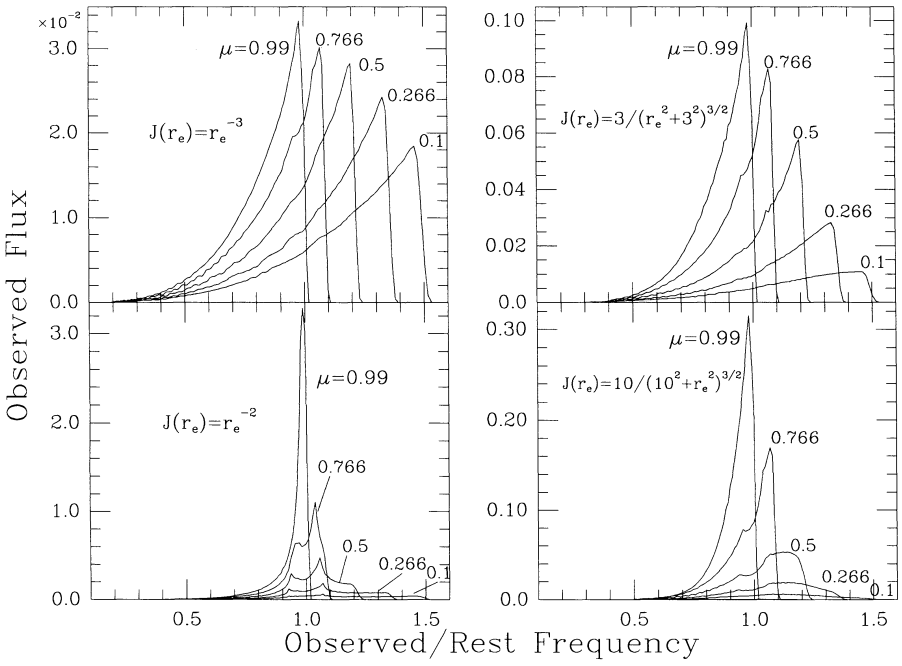

Figure 2.18: The relativistic disk line profiles for various emissivity laws of $J(r_e)$. The inclination angles of $\nu = \cos i$ are indicated, and the flux is normalized in an artificial unit (Laor 1991).

2015).

2.4.6 Timing behavior

Measurement of rapid X-ray variability on milliseconds to seconds time scales is important to understand the emission mechanism of black hole binaries. Because it is a clue to study black hole binaries with a new sight of view, while spectrum fitting always relies on the spectral model. There are many achievements with timing analysis (e.g., Galeev et al. 1979; Poutanen & Fabian 1999; Churazov et al. 2001; Done et al. 2007; Uttley et al. 2011), such that the high/soft state spectrum shows very little rapid variability although strong variations in the luminosity of the disc blackbody component are seen on long time-scales corresponding to transitions between the soft and hard spectral states (Belloni et al. 2005). On the other hand, variability of several tens of percents has been observed in the low/hard state and it is thought that the origin of variability is energetically dominated by the power-law emission and is associated with a hot optically thin flow, magnetized corona, or even the base of the persistent radio-emitting jets (e.g., Zdziarski et al. 1998; Markoff et al. 2005; Droulans et al. 2010). Additionally, strong quasi-periodic oscillations (QPOs) are observed during the state transitions of black hole binaries (e.g., Axelsson et al. 2005; Sobolewska & Życki 2006; Done et al. 2007).

Figure 2.19 shows the energy spectra (left) and Power Spectral Densities (PSDs, right) of GRS J1655−40 in steep power-law, thermal, and hard state (Remillard & McClintock 2006, See also Figure 2.16 for spectral transition of the object). In the Steep Power Law (SPL, correspond to very high state) and the Thermal (correspond to high/soft state), the power × frequency is less variable. While, in the Hard (low/hard) state, the variation power is much higher than that of other states, and QPOs are frequently observed. Also figure 2.20 shows the evolution of the PSD of Cyg X-1 from hard state (panel a) to canonical soft state (panel f) (Axelsson et al. 2005). The top three panels (a-c) are observed within a few hours during MJD 52330, panels d and e are from MJD 52324 with no more than a few hours apart, and the bottom panel (f) is from an observation on MJD 52358. These panels illustrate the shift in the peak frequencies of the Lorentzians (dashed line) as it shifts to higher frequencies, the gradual increase of the power-law as the source goes from the hard state to the soft state, and changes that can occur on this timescale. Figure 2.21 shows the typical low/hard and high/soft spectrum of three black hole binaries (top panel), and the PSDs (bottom panel) associated with the top panel, which are observed by PCA and HXTE onboard *RXTE*. The power of Cyg X-1 shows the "flat structure" ∼10 Hz, and decreases above ∼10 Hz in high/soft state. While other binaries shows the peak structure in high/soft state.

The disk does not vary on timescales of less than a few seconds in the high/soft state (e.g. Churazov et al. 2001, also See §2.3.4), so variability on faster timescales must instead be connected to the Comptonization region(s). This fast variability shows that the light curves at higher energies are correlated with those at lower energies, but with a time lag, and this lag gets shorter for faster variability timescales (Miyamoto & Kitamoto 1989; Nowak et al. 1999; Pottschmidt et al. 2000; Grinberg et al. 2014). Such frequency dependent time lags are commonly seen in the low/hard state, where they are now interpreted as fluctuations propagating down through a Comptonising flow which is radially stratified in both spectrum and variability. Slow fluctuations are stirred up at larger radii, where the spectra are softer. These propagate down to modulate the emission from smaller radii where the spectra are harder, giving rise to a lag of the hard band relative to the soft. Faster fluctuations are stirred up closer to the black hole, so they have less far to propagate in order to reach the hard spectral region, thus giving shorter lags (Lyubarskii 1997; Kotov et al. 2001; Arévalo & Uttley 2006; Rapisarda et al. 2016). The high/soft state in Cyg X-1 has frequency dependent time lags in its fast variability (Pottschmidt et al. 2000), so must have radially stratified Compton continuum spectra rather than a single non-thermal Compton component.

Figure 2.22 shows frequency-resolved lag–energy spectra for four frequency ranges from 0.034 Hz to 8 Hz of GX 339−4. The lags are all measured relative to the same 0.54–10.08 keV band and plotted so that energies with more positive values of lag are lagging behind energies with less positive values of the lag. In the insets of the figure, the covariance spectra for the same frequency ranges are shown, which are plotted as ratio to the simple absorbed power-law (photon index=1.55, absorption

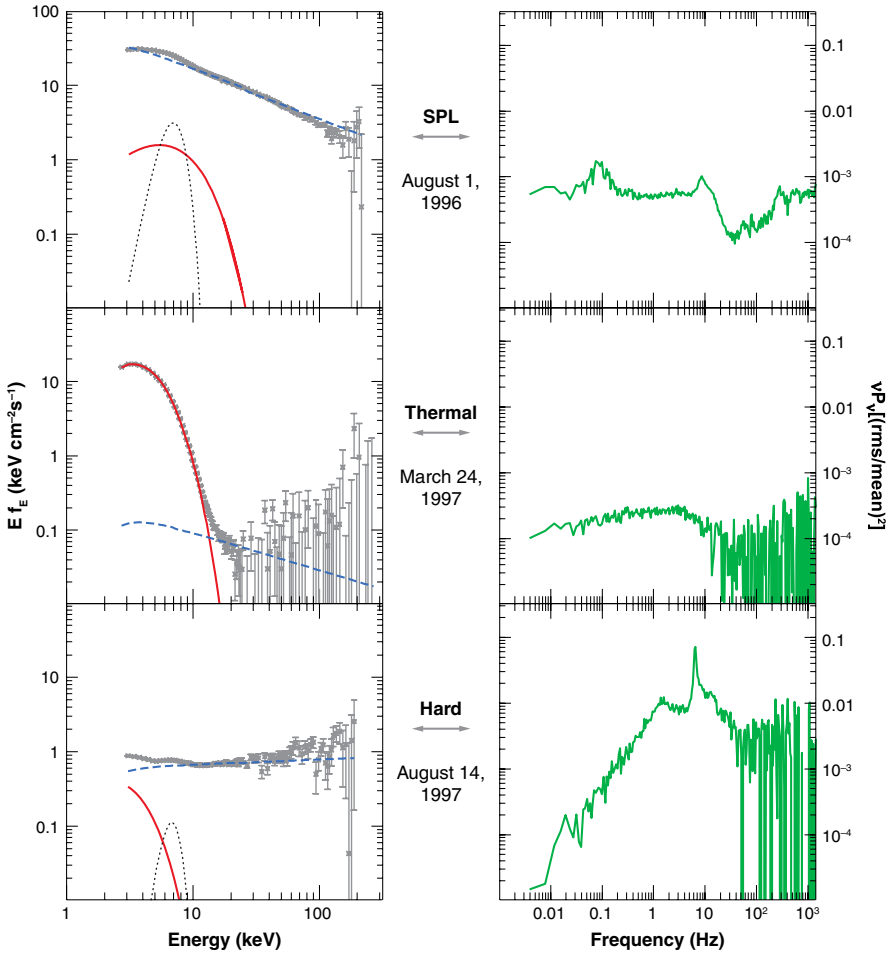

Figure 2.19: The energy spectra (left) and Power Spectral Densities (PSDs, right) of GRS J1655−40 in steep power-law, thermal, and hard state. In the left panels, red solid lines show thermal component, blue dashed lines show power-law, and black dotted lines show Fe Kα. Right panels plotted as $\log(\nu \times P_\nu)$ versus $\log \nu$ (Remillard & McClintock 2006).

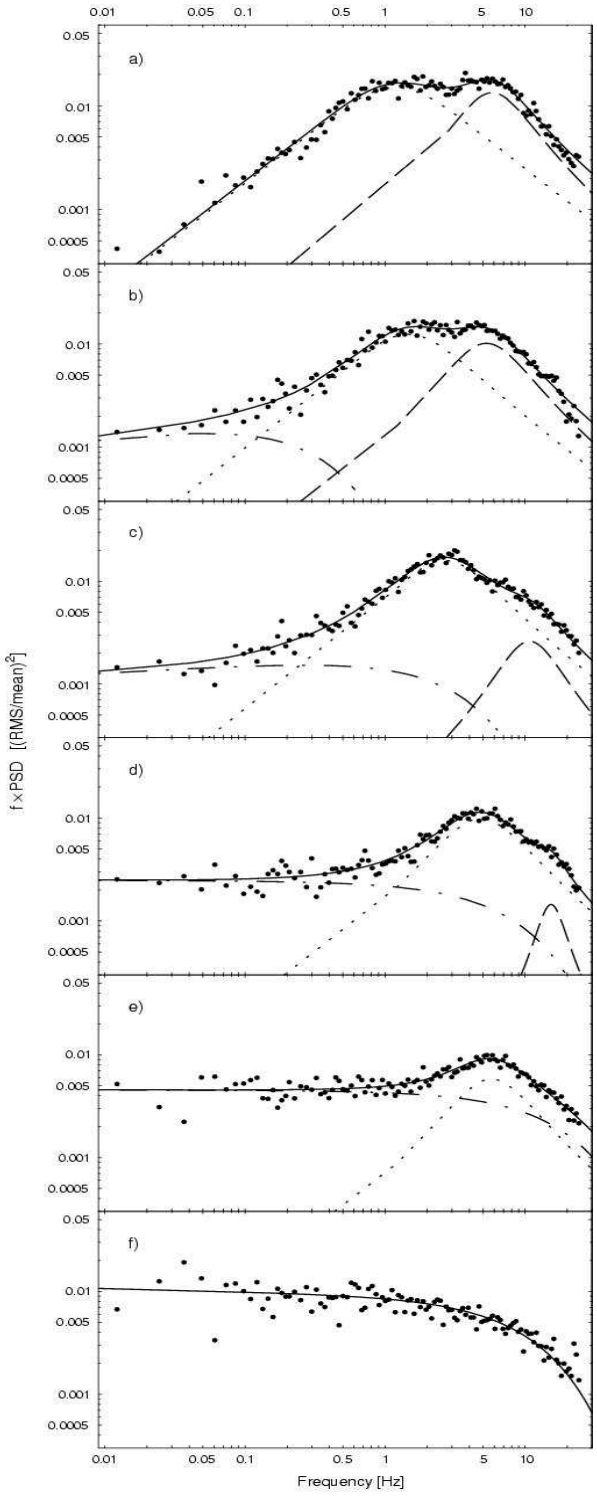

Figure 2.20: The evolution of the PSD of Cyg X-1 from hard state (panel a) to canonical soft state (panel f). The top three panels (a-c) are observed within a few hours during MJD 52330, panels d and e are from MJD 52324 with no more than a few hours apart, and the bottom panel (f) is from an observation on MJD 52358 (Axelsson et al. 2005).

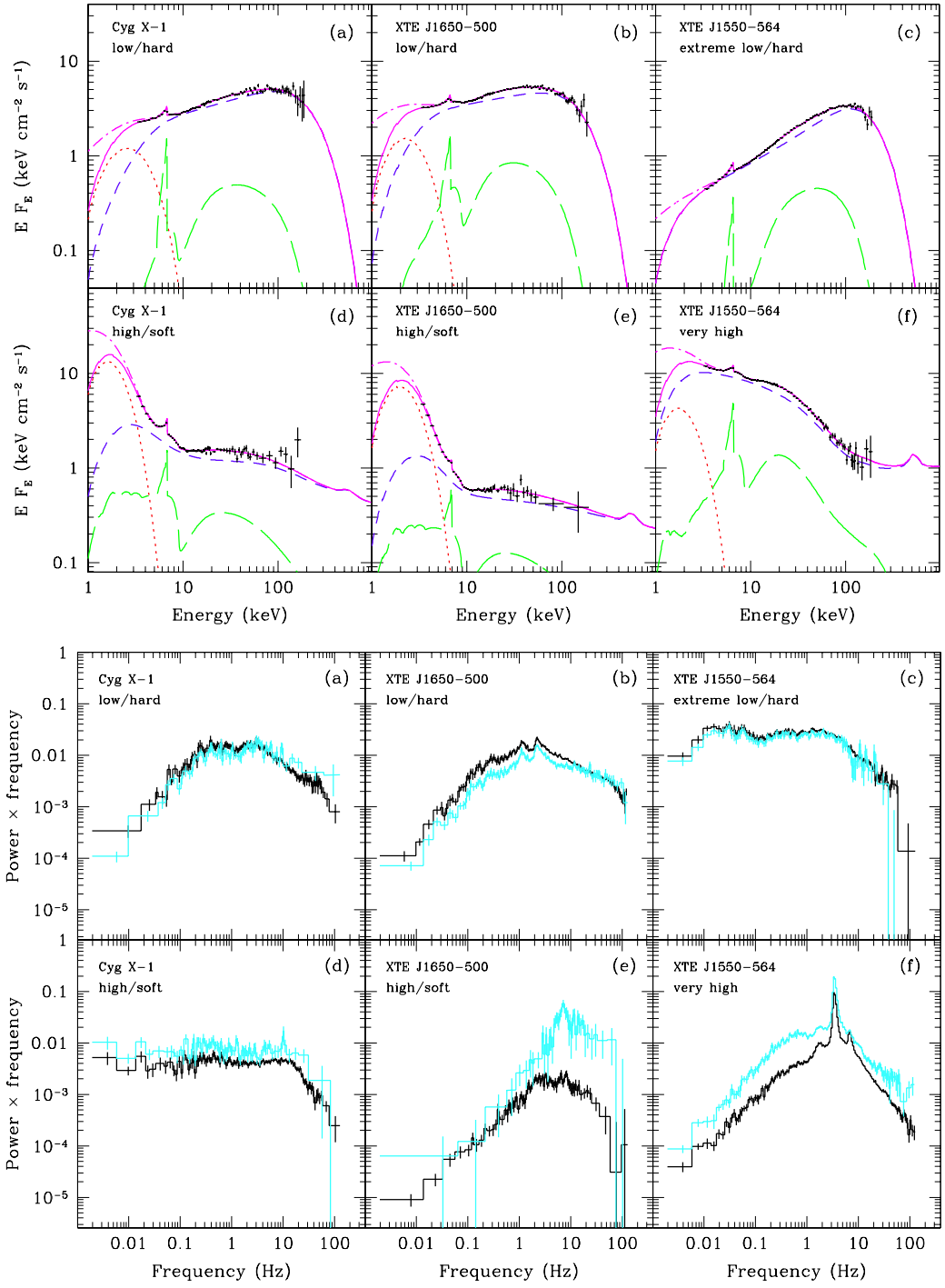

Figure 2.21: Top: The typical high/soft and low/hard spectrum of three black hole binaries observed by PCA and HXTE onboard *RXTE*. Bottom: The PSDs associated with the top panel. (Done & Gierliński 2005).

is 6×10^{21} cm^2 fitted to the 3–10 keV range) model.

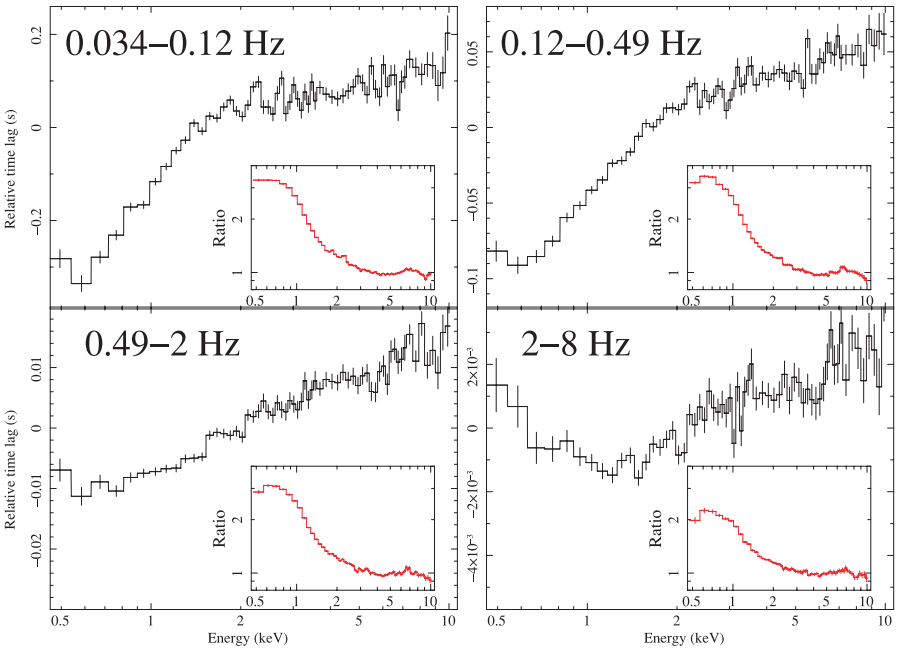

Figure 2.22: The frequency-resolved lag–energy spectra for four frequency ranges from 0.034 Hz to 8 Hz of GX 339−4, and the covariance spectra for the same frequency ranges are shown in the insets (Uttley et al. 2011).

2.4.7 Outflows from black hole binaries

Some galactic X-ray binary systems have a jet, and they are named as "microquasar" after similar properties of quasars. Thus some black hole binaries are also called as microquasars; such as GRS 1915+105, SS 433, 1E 1740.7−2942, GRO J1655−40, and XTE J1550−564. In the strict definition, microquasar is limited for a black hole binaries, but generally we refer celestial objects with relativistic jets including neutron stars as microquasars. The microquasar is an ideal laboratory to study the relation between mass accretion and outflow (such as jet). In the X-ray region, emission from the inner region of disk is dominated, while in the radio and infra-red synchrotron radiation from a jet is dominated. Therefore, conducting a simultaneous multi-wave observation, we can study these relations. Variation time scale depends on the Schwartzshild radius and thus the mass of black hole. Thus, we can study the time evolution of accretion disk and jet with reasonable time scale. (For example, a phenomena can be traced within several minutes in microquasars even though it take thousand years in M 87 galaxy.)

GRS 1915+105 is one of the most studied microquasars, and has a distinctive feature. Figure 2.23 shows a light curve of GRS 1915+105 in the X-ray band, infra-red, and radio (Mirabel et al. 1998). Obviously, we can see huge fluctuations with

time scale of ∼1 minute, and quasi periodic dip after that. Interestingly, during the dip, the spectral index becomes harder. The behaviors are interpreted to be due to the luminosity of GRS 1915+105 is close to the Eddington limit and has high mass accretion rate. When thermal instability in the inner part of the disk is saturated, enormous gas is transferred to the black hole, and it occurs cyclically. Furthermore, it is interesting to note that the disk transition seems to be a trigger of the jet. When the X-ray spectrum transits from hard to soft, the jet seems to be appeared; the simultaneous radio and infra-red flares have been observed. Here, it is qualitatively understood that the radio peak after the infra-red peak is caused by the wavelength dependency of the emission peak, because a plasma, which emits synchrotron radiation, is expanding. The similar behavior was obsersed with other microquasars, and the state transition seems to have a key to understand the mechanism of the jet.

Figure 2.24 shows an unified model of the disk evolution and the jet formation/suppression, which shows the relationships between jets and X-ray states (Fender et al. 2004). In the lower panel, the jet Lorentz factor and the disc inner radius are explained qualitatively. Also in the sketches of i–iv, morphology of the jet changes in the X-ray state are shown, and, in the top panel, tracks of state transitions of an X-ray source are also shown in the hardness-intensity diagram. The solid vertical line in the figure is named as "jet line", which determines presence or absence of compact jets. In the right region from the jet line, the X-ray spectrum is relatively hard and a steady radio jet is present, and in the left reign, the spectrum is soft and the jet is quenched. While the mechanism of the jet launch is thought to be more complicated from recent studies, which indicates that hard-to-soft transitions are not always be a tiger of the launch of the jet (Miller et al. 2012; Rushton et al. 2012; Paragi et al. 2013).

For Cyg X-1, a mildly relativistic ($v \sim 0.6c$) 'quiescent' radio jet, which is extending to 15 milliarcsec from a core region with an opening angle of 2°, is always detected by Very Large Array (VLA) at 8.4 GHz in the low/hard X-ray state (Stirling et al. 2001). While, in the high/soft X-ray state, very long baseline interferometry (VLBI) detected unresolved weak compact jet of ∼0.2 milliarcsec (at 4 cm) and ∼3 milliarcsec (at 13 cm) using the residual positions of removing proper motion, parallax and orbital motion signatures (Rushton et al. 2012).

On the other hand, the jet of Cyg X-1 in X-/gamma-ray is not clear and some indirect detection have been reported. *INTEGRAL* detected very high polarization from Cyg X-1 for a total exposure of more than 2.5 million seconds over 6.5 years; polarization degree of $> 75\%$ with polarization angle of 39°±3 in 370-850 KeV (Jourdain et al. 2012, *INTEGRAL*/SPI), polarization degree of 67±30% with polarization angle of 40°±15 in 400-2000 KeV (Laurent et al. 2011, *INTEGRAL*/IBIS), and they claimed that the origin of the highly polarized X-/gamma-ray is a jet. However, it is important to note that the angle of radio jet is -20° to -25° and away from the *INTEGRAL* polarization results. *INTEGRAL* is not designed as dedicated polarimeters, nor calibrated as such.

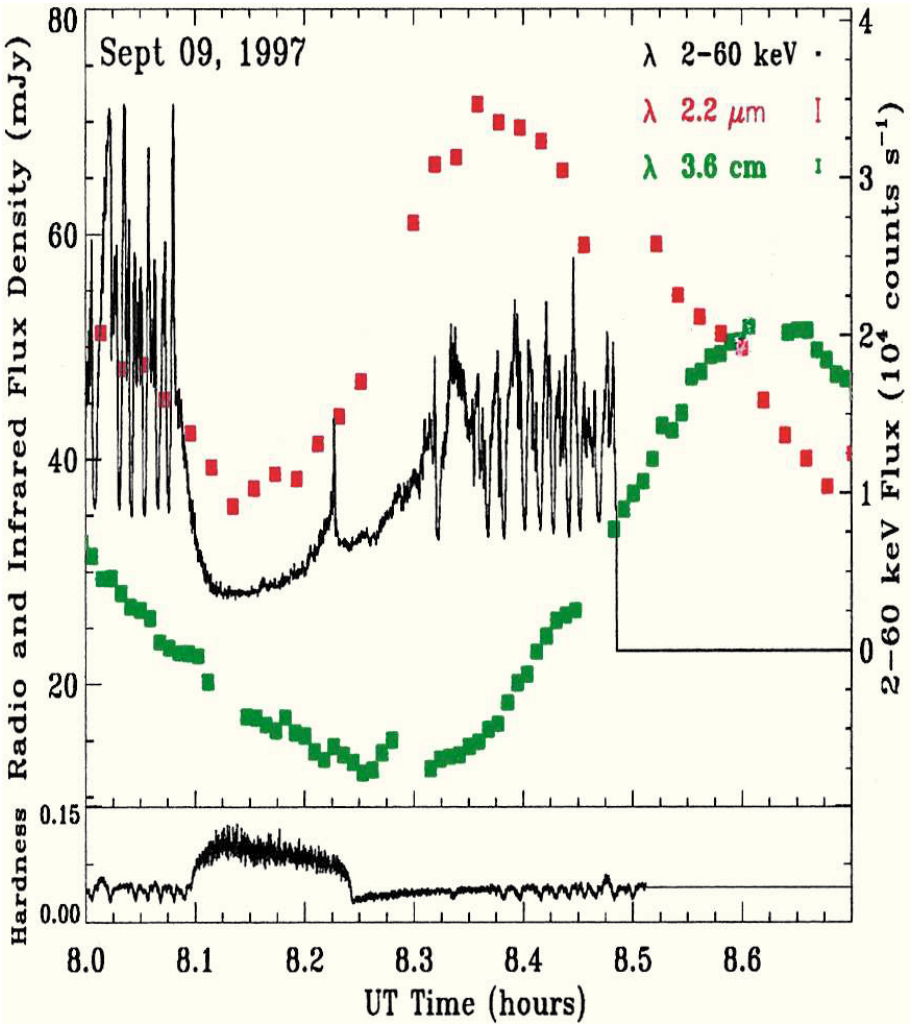

Figure 2.23: Top: The light curve of GRS 1915+105. Black line: X-ray in 2-60 keV. Red square: infra-red of 2.2 μm. Green square: iradio of 3.6 cm. Bottom: The hardness ratio between 13-60 keV to 2-13 keV. (Mirabel et al. 1998).

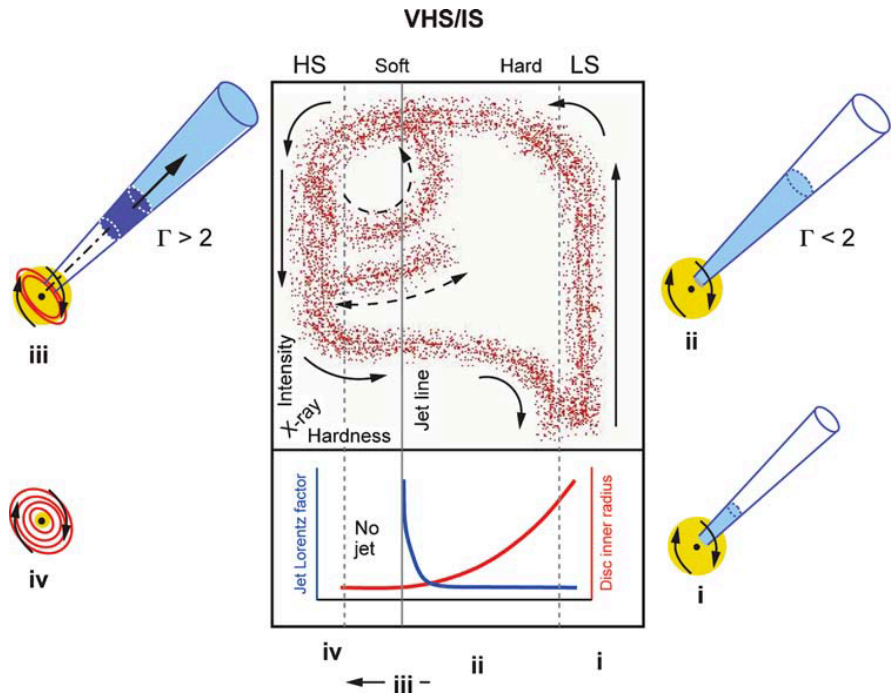

Figure 2.24: A schematic view of the model for disk-jet coupling in black-hole binaries. The upper panel shows a typical X-ray hardness-intensity diagram of black hole binaries (here, "HS" indicates the high/soft state, "VHS/IS" indicates the very high or intermediate state, and "LS" indicates the low/hard state). The lower panel shows the variation of the bulk Lorentz factor of the outflow (blue) and inner disk radius (red) against the hardness ratio. The sketches of i–iv show the morphology of the jet evolve with changes in the X-ray state (Fender et al. 2004).

In gamma-rays, ∼1-2 day long flare events above 100 MeV was reported by *AGILE* (Sabatini et al. 2010, 2013) in the and high/soft state hard-to-soft transtion, and also by *MAGIC* above 100 GeV (Albert et al. 2007) in the the high/soft state. Also there are a report that *Fermi*/LAT detected emissions with very soft spectrum in above 40 MeV in the hard state with 7.5-year data(Zanin et al. 2016). They concluded that it is a high-energy cut off of the high-energy power-law tail, and is most likely associated with the relativistic jets (Zdziarski et al. 2016a,b).

The origin of the jets in (micro)quasars or other celestial objects are still controversial, but today it is thought that black hole spin is key to produce the jet (See §2.6).

2.5 Estimation of the black hole spin

Measuring black hole spin is important in order to understand and quantify its effect on the relativistic jet from the accretion flow (See e.g., McClintock et al. 2014). However, unlike mass, spin is difficult to determine as it only affects the spacetime properties very close to the black hole. In this section, we mainly refer to the results of Cyg X-1, and results are summarized in Table 2.3.

There are three potential observational methods, and two theoretical scenarios in the literature;

- core collapse and Standing Accretion Shock Instability scenario (See §2.2)
- tidal locking scenario
- characteristic fast variability features (low and high frequency quasi-periodic oscillations: QPOs)
- last stable circular orbit;
  - disk continuum fitting
  - profile of the fluorescent iron line emission

tidal locking scenario

The spin is solely determined by the system parameters at tidal locking. Because the tidal-synchronization timescale of the massive star is short enough to allow for the star to rotate synchronously with the orbital period, and the maximum spin the system could be constrained by tidal synchronization with the companion star at a very late stage in its evolution (Moreno Méndez & Cantiello 2016, and references there in). Figure 2.25 shows the relation between black hole spin and orbital period (Lee et al. 2002; Brown et al. 2008). It assumes that the black hole resulting from the collapse of a helium star synchronizes with the orbit, and shows that the result depends very little on the mass of the black hole. From the current orbital period of Cyg X-1 of 5.6 days, and considering a maximum mass loss of $1M_{\odot}$ (See §2.2), the orbital period of the binary at the time of BH formation is estimated to be $\sim$5.3 days, and black hole spin is estimated that less than 0.1 from Figure 2.25 (Brown et al. 2008).

characteristic fast variability features

There is mounting observational evidence in favor of a Lense-Thirring (vertical) precession origin for the low frequency QPOs (Ingram et al. 2016), but the frequency depends on both spin and radius of the precessing material rather than spin alone (Stella & Vietri 1998; Ingram et al. 2009). Combining this with the high frequency QPOs potentially breaks this degeneracy, but the spin value obtained depends on

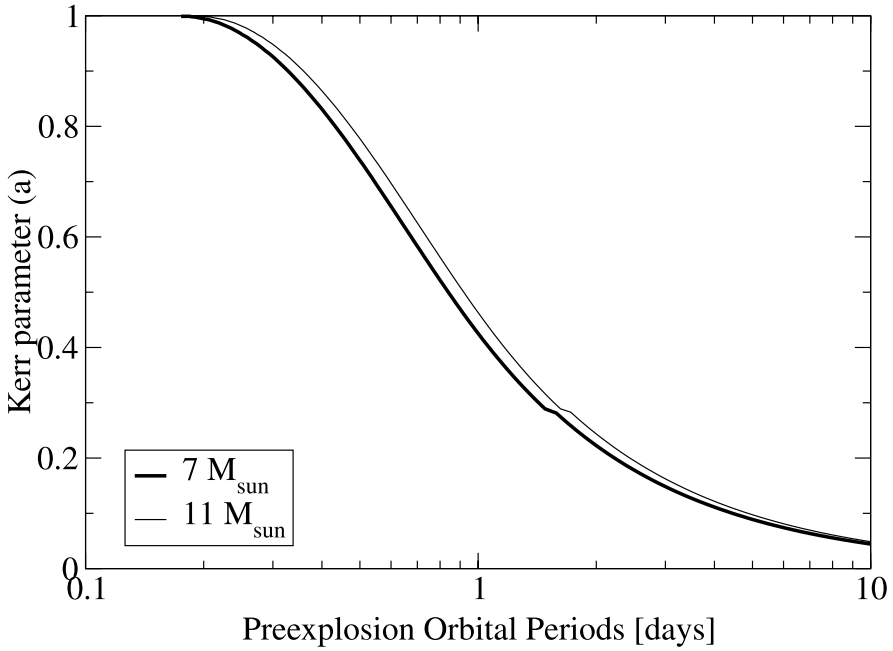

Figure 2.25: The relation between black hole spin and orbital period for 7 $M_\odot$ and 11 $M_\odot$ black hole binary (Lee et al. 2002; Brown et al. 2008).

which high frequency oscillation mode is assumed to produce them, and this is not yet clear (Motta et al. 2014; Fragile et al. 2016). Axelsson et al. (2005) estimated black hole spin of Cyg X-1 with more than 750 pointed observations data of *RXTE* (See Figure 2.20), and assumed the Lorentzian profiles followings (Gilfanov et al. 1999; Stella & Vietri 1999; Nowak 2000);

$$
\begin{aligned}
L_i(f) &= \frac{H_i W_i \nu_i}{(f-\nu_i)^2 + f W_i \nu_i} \quad \text{(Lorentzian profiles; Gilfanov et al. 1999, Nowak 2000)} \\
\nu_{nod} &\propto a_* M^{1/5} \nu_{per}^{6/5} \quad \text{(Stella \& Vietri 1999)} \\
\nu_{nod} &= \nu_\phi - \nu_\theta \quad \text{(the nodal precession frequency)} \\
&= \frac{1}{2}\nu_1 \\
\nu_{per} &= \nu_\phi - \nu_r \quad \text{(the periastron precession frequency)} \\
&= \nu_2 \\
\mathrm{H_i} &: \text{the value of } f P_f \text{ at the peak frequency } \nu_i \\
\mathrm{W_i} &: \text{width of the measurement profile}
\end{aligned}
$$

and estimated black hole spin as 0.48±0.01 (they also obtained -0.57±0.01 for retrograde rotation answer at the same time. However, they only use positive (prograde) one following papers such as Axelsson et al. 2011) as shown in Figure 2.26.

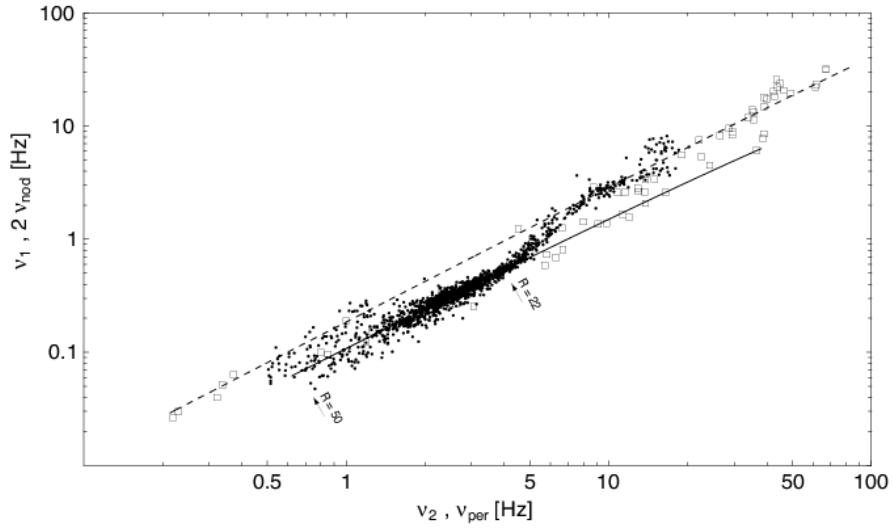

Figure 2.26: The relation between peak frequencies. The fitting results show black hole spin as 0.48±0.01 (prograde) and -0.57±0.01 (retrograde) (Axelsson et al. 2005).

last stable circular orbit; disk continuum fitting

The soft X-ray component in the high state can be used to estimate the black hole spin by assuming that the MCD emission region reachs down the radius of innermost last circular orbit. Makishima et al. (2000) used MCD plus power-law model for *ASCA* data, and estimated the inner radius of the disk ($R_{\rm in}$) from the bolometric luminosity ($L_{\rm bol}$) and the temperature of the inner disk ($T_{\rm in}$), utilizing the formula of $R_{\rm in} = \xi\kappa^2\sqrt{\frac{L_{\rm bol}}{4\pi\sigma T_{\rm in}^4}}$, where $\xi = 0.412$ is correction factor reflecting the fact that $T_{\rm in}$ occurs at a radius somewhat larger than $R_{\rm in}$, and $\kappa \sim 1.7$ is the ratio of the color temperature to the effective temperature. Figure 2.13 shows the results for some black hole binaries, and the innermost radius of Cyg X-1 is close to that of Schwarzschild black hole (black hole spin ~ 0). Miller et al. (2009) used relativistic thermal disk model (KERRBB, Li et al. 2005) and the constant-density-ionized (CDID)-disk reflection model (Ballantyne et al. 2001) for $XMM-Newton$ data, and estimated black hole spin as 0.05±0.01 as shown in Figure 2.27 upper left.

While Gou et al. (2011, 2014); Tomsick et al. (2014); Walton et al. (2016) derived an extremely high spin value, using relativistic disk, Comptonisation or (cut-off) power-law, and reflection model for *RXTE*, *ASCA*, *Chandra*, *Swift*, *Suzaku*, *NuSTAR* data as shown in Figure 2.27.

Transient black hole binaries show a large scale hysteresis, where the hard-to-soft transition during the rapid outburst rise can occur at a much higher (up to at least a factor of 10) luminosity than the reverse transition on the decline, and the luminosity of the hard-to-soft transition itself is variable between different outbursts of the same source (e.g., Smith et al. 2002; Maccarone & Coppi 2002; Gierliński & Newton 2006; Gladstone et al. 2007; Dunn et al. 2010; Yu & Yan 2009). Utilizing

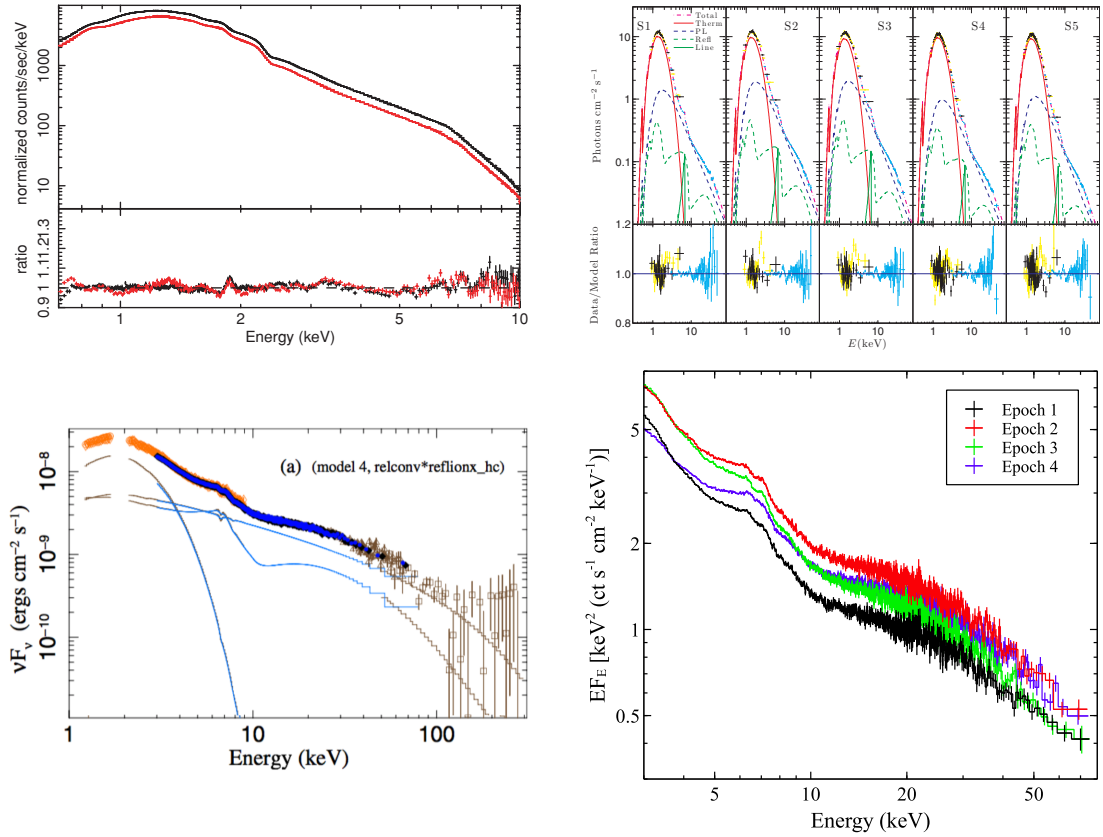

Figure 2.27: Cyg X-1 spectrum in high/soft state. Upper left: $XMM-Newton$ spectra with relativistic thermal disk and continuum model (KERRBB, Li et al. 2005) and the constant density ionized (CDID) disk reflection model (Ballantyne et al. 2001), and black hole spin of 0.05±0.01 is estimated (Miller et al. 2009). Upper right: S1-S2:$Chandra$ and $RXTE$, S3-S4:$Swift$ and $RXTE$, S5:$Suzaku$(2010) spectrum with relativistic thermal disk and Comptonization of disk photons and the relativistic reflection model, and black hole spin of >0.983 is estimated (Gou et al. 2014). Lower left: $NuSTAR$ and $Suzaku$ spectrum with disk blackbody component, a cutoff power-law, a REFLIONX_HC reflection model with relativistic blurring, and a simple ionized absorber, and black hole spin of >0.83 is estimated (Tomsick et al. 2014). Lower right: $NuSTAR$ spectrum. The spectrum is fitted with the simple model consisting of an relativistic thermal disk and a high-energy power-law tail, and black hole spin of 0.93< a_* <0.96 is estimated (Walton et al. 2016). See also Table 2.3 for summarized parameters.

equation (2.20), we can estimate the R_{in} (e.g., Kubota et al. 2001; Gierliński & Done 2004; Davis et al. 2006; Done et al. 2007; Done & Davis 2008; Kolehmainen & Done 2010; Kolehmainen et al. 2011). Figure 2.28 shows the relation between the disk luminosity and the T_{in} for LMC X-3 and GRO J1655−40. The system parameters of these objects are very similar; black hole mass of ∼6.98 and 6.3±0.5, inclination angle of 69.24±0.72 and 70.2±1.9 for LMC X-3 and GRO J1655−40, respectively. However, the estimated R_{in} is ∼60 km and ∼27 km, corresponding to black spin of ∼0 and ∼0.65, respectively. The anomalous component in GRO J1655−40 is though as Comptonization, and a similar component is observed in XTE J1550−564 and more discussed in Kubota & Makishima (2004).

By contrast, in Cyg X-1, the hysteresis is only small scale, less than a factor of 2-3, and the hard-to-soft transition luminosity is fairly stable, thus we cannot see the L-T relation nor cross check at different luminosity whether we get the same spin from the disc continuum fits or not (Smith et al. 2002; Zdziarski et al. 2002).

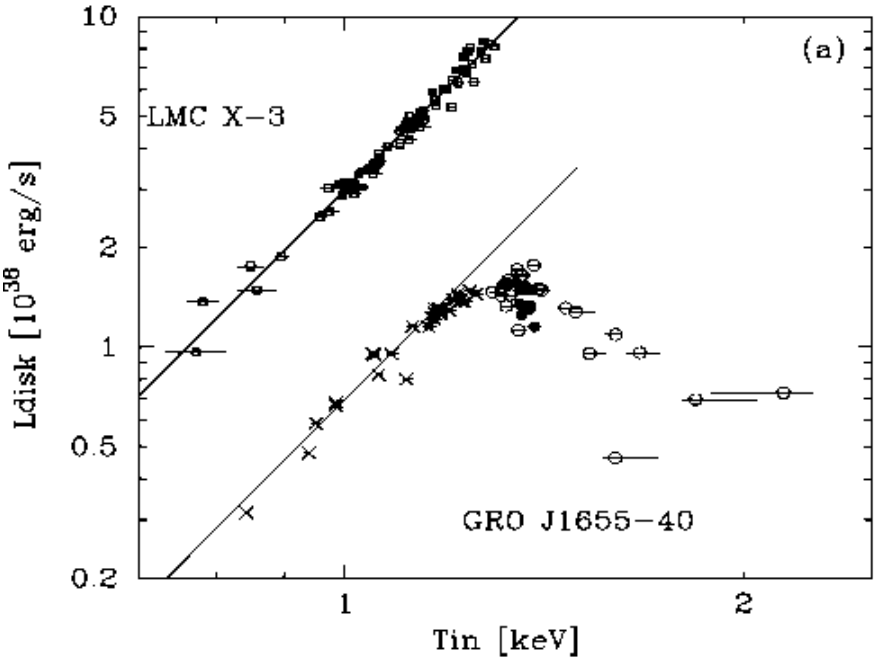

Figure 2.28: The relation between the disk luminosity and the T_{in} for LMC X-3 and GRO J1655−40. Black hole spin of ∼0 and ∼0.65 are estimated for these object, respectively (Kubota et al. 2001).

the last stable circular orbit; fluorescent emission

In the low/hard state, the reflection and Comptonized component dominate the spectrum (See §2.4.4). Since the fluorescence iron-K line is seen in the reflection

component and it is originated from the inner disk, the profile of the iron line emission would be a tracer of black hole spin.

There are some estimations of black hole spin with the model of the fluorescent iron line emission for $XMM-Newton$, $RXTE$, $Suzaku$, and $NuSTAR$ data (Duro et al. 2011; Fabian et al. 2012; Parker et al. 2015) as shown in Figure 2.29. All results show an extremely high spin and it means the disk continue to the innermost stable circular orbit like in the high/soft state. However, it is still controversial (See §2.4.4). We note again that reflection fits generally give an extremely high spin for GX 339−4 (e.g. Ludlam et al. 2015; Kubota & Done 2016), while continuum fitting allows low spin solutions (Kolehmainen & Done 2010).

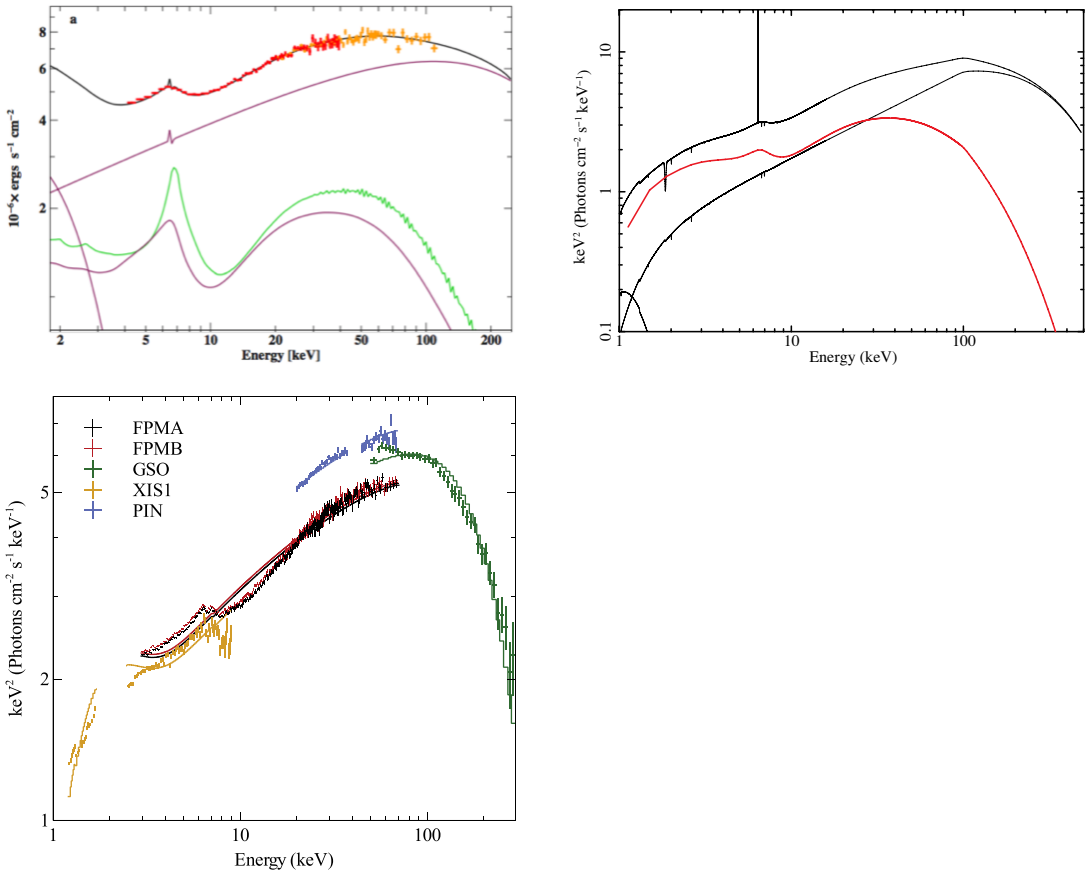

Figure 2.29: Cyg X-1 spectrum in low/hard state. Upper left: $XMM-Newton$ and $RXTE$ spectrum with relativistic thermal disk, cutoff power-law, and relativistically smeared reflection model, and black hole spin of $0.88^{+0.07}_{-0.11}$ is estimated (Duro et al. 2011). Upper right: $Suzaku$ (2009) spectrum with thermal disk, high cut power-law, and relativistically blurred reflection model, and black hole spin of $0.97^{+0.014}_{-0.02}$ is estimated (Fabian et al. 2012). Lower: $NuSTAR$, $Suzaku$ (2014) spectrum with thermal disk, two temperature Compton, and relativistically relativistic reflection model, and black hole spin of >0.97 is estimated (Parker et al. 2015). See also Table 2.3 for summarized parameters.

Table 2.3: The estimated black hole spin of Cyg X-1

Method	state	observatory	spin	References
CC-SASI senario	—	—	<0.15	(Moreno Méndez & Cantiello 2016)
tidal locking	—	—	<0.1	(Brown et al. 2008)
QPO	low/hard	*RXTE*	0.48 ± 0.01	(Axelsson et al. 2005)
continuum fitting	high/soft	$XMM-Newton$	0.05 ± 0.01	(Miller et al. 2009)
		RXTE, *ASCA*, *Chandra*	>0.95	(Gou et al. 2011)
		Chandra, *RXTE*, *Swift*, *Suzaku*(2010)	>0.983	(Gou et al. 2014)
		NuSTAR, *Suzaku*(2012)	>0.83	(Tomsick et al. 2014)
		NuSTAR	$0.93< a_* <0.96$	(Walton et al. 2016)
line fitting	low/hard	$XMM-Newton$, *RXTE*	$0.88^{+0.07}_{-0.11}$	(Duro et al. 2011)
		Suzaku(2009)	$0.97^{+0.014}_{-0.02}$	(Fabian et al. 2012)
		NuSTAR, *Suzaku*(2014)	>0.97	(Parker et al. 2015)

2.6 Relation between black hole spin and jet

There are only a few studies about the relation between black hole spin and jet power for black hole binaries (e.g., Narayan & McClintock 2012; Ludlam et al. 2015), and some results show the correlation, but some results do not, thus, it is still under discussion.

Figure 2.30 shows one of observational results of the relation between jet power and spin (Narayan & McClintock 2012). They utilized of five transient LMXBs of A0620−00, XTE J1550−564, GRO J1655−40, GRS 1915+105, and 4U 1543−47. The spin parameters are estimated by an assumption of the disc inner edge is close to the innermost stable circular orbit (See §2.3.3), and the jet power is estimated by the formula of $P_{\rm jet} \equiv D^2(\nu S_\nu)_{\rm max,5\ GHz}/M$, where S_ν is a peak flux at a standard frequency of 5 GHz and normalized by the distance to the source D and BH mass of M.

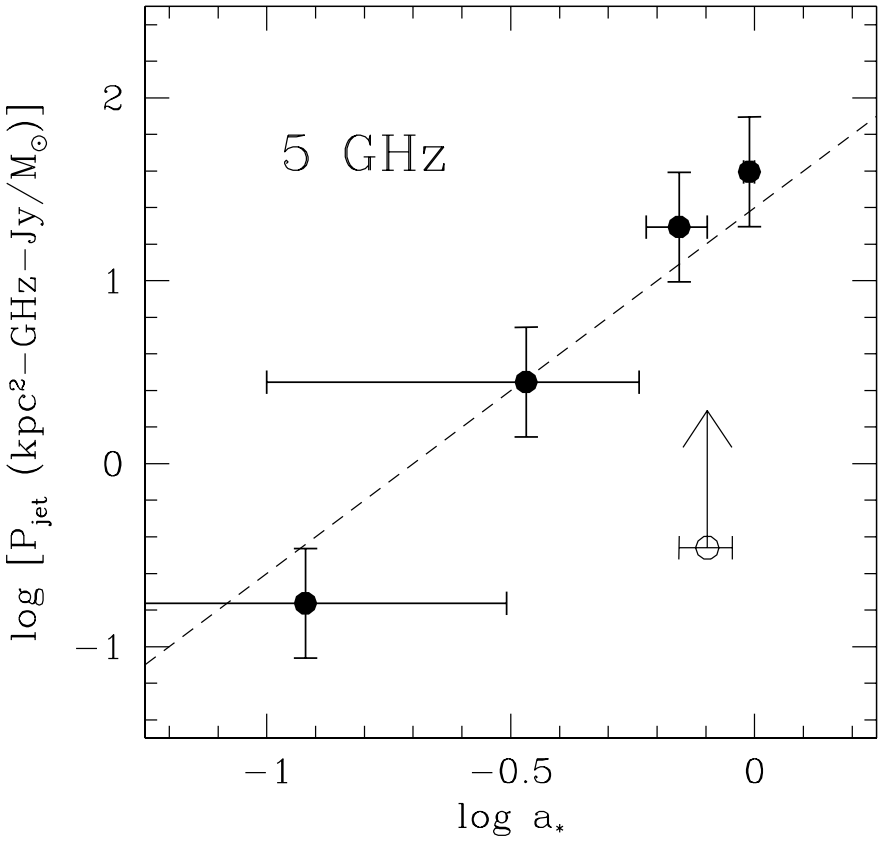

Figure 2.30: The relation between a power of jet and a spin of black hole. The jet power is estimated with the formula of $P_{\rm jet} \equiv D^2(\nu S_\nu)_{\rm max,5\ GHz}/M$, and spin value is estimated with an assumption of the disc inner edge is close to the innermost stable circular orbit. (Narayan & McClintock 2012).

2.7 Motivation and Strategy of this Study

Cyg X-1 is one of the most studied object as described in previous sections, however, black hole spin is poorly understood. Thus, in this thesis, we aim to constrain black hole spin with the most plausible method. We choose the method of the estimation of the R_{in} with fitting the continuum component of the spectrum in high/soft state, because the technique to utilize a emission lines for the tracer of the inner edge of the disk in the low/hard state is still controversial, and the technique to utilize QPOs has been studied with more than 750 pointed observations data of *RXTE*, thus we would not obtain significantly better statistics than previous work, furthermore the technique has a potential to have answers of prograde and retrograde at the same time.

The spectrum of Cyg X-1 always shows the stronger tail, and it makes difficult to estimate the 'true' R_{in}. Therefore we aim to find the best spectrum, whose tail component is the smallest ever observed, and try to find the best spectral model to explain the spectrum and estimate black hole spin robustly.

Furthermore, we validate the models with new sight of light, timing technique, and conclude the best model and black hole spin.

This thesis is comprised as follows. Chapter 2 gives an over view of the X-ray observatory of *Suzaku*. Chapter 3 and 4 describe the observational studies of Cyg X-1, and these chapters are based on the publication of Kawano et al. (2017). Chapter 5 provides a summary of the results and conclusions of the thesis.

Chapter 3

Instrumentation

3.1 The selection of instrumentation

Ideally, to estimate black hole spin, we need to observe the spectrum of Cyg X-1 as broad as possible. Figure 3.1 shows the schematic spectrum of a black hole binary in high/soft state with the energy range of current/recent X-ray observatories. The spectrum has a thermal peak around ∼1 keV, and higher energy tail is up to several hundred keV. Thus, we need to observe both of the thermal component and the hard tail to estimate black hole spin, because the shape of the thermal component is depending on the estimation of the hard tail. Considering the energy range, *Suzaku* is the best X-ray observatory for the strategy of the study. Thus, we utilize *Suzaku* for the study, and we refer the instrumentation of *Suzaku* in following sections.

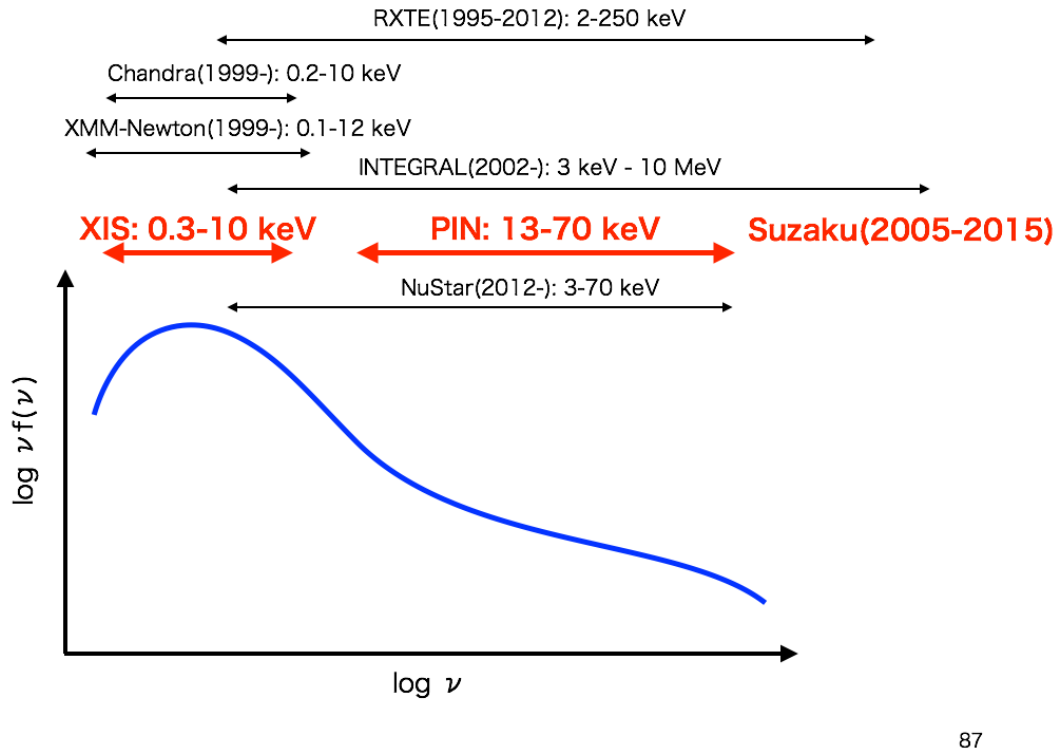

Figure 3.1: The schematic spectrum of a black hole binary in high/soft state with the energy range of current/recent X-ray observatory

3.2 Overview of the *Suzaku* satellite

Suzaku (Mitsuda et al. 2007), which is called $ASTRO-E2$ before the launch, is the Japanese nineteenth scientific satellite and the fifth X-ray astronomical satellites. *Suzaku* was launched from Uchinoura Space Center with the M-V launch vehicle by Japan Aerospace Exploration Agency (JAXA) on July 10th 2005. The interest life of the *Suzaku* satellite was set as 2 years, however the scientific observations had been conducted around 10 years. Because of aged deterioration of the battery system, the radio connection was getting difficult. Finally, the scientific observations finished on June 1st, 2015.

An overview of the *Suzaku* satellite is shown as Figure 3.2. The weight of Sukzau satellite is 1680 kg, the length is 6.5 m along the telescope axis with an extendible optical bench (EOB), and the diameter of the octagonal-shaped body is 2.1 m. The total power consumption is ∼660 W. The *Suzaku* satellite aimed to conduct wide-band high resolution and photometry/spectrometric observations for great variety of X-ray sources such as the black hole systems, cosmic hot plasma, cluster of galaxies to investigate the cosmic large-scale structure, the evolution of cluster of galaxies, the evolution of active galactic nuclei, the evolution of cosmic heavy element, and so on. To accomplish these scientific goals, more than 20 Japanese insinuations, together with a Japan-US collaboration have been contributed to construct the satellite.

The energy range for pointing observation of the *Suzaku* satellite is 0.2 – 600 keV band with the X-ray Imaging Spectrometer (XIS, Koyama et al. 2007) and the Hard X-ray Detector (HXD, Takahashi et al. 2007), and X-ray micro calorimeter (the X-ray Spectrometer, or XRS, Kelley et al. 2007), but XRS did not work in orbit because of the liquid helium coolant failure. The XIS composes four X-ray sensitive imagine CCD cameras, which locate at the foci of the X-ray Telescopes (XRT, Serlemitsos et al. 2007). Three XISs (XIS0, XIS1, XIS3) are front-illuminated CCDs (FI: energy range of 0.4 – 12 keV), and another (XIS2) is a back-illuminated CCD (BI: energy range of 0.2 – 12 keV). The HXD is non-imaging, collimated detector, which has energy range of 10 – 600 keV and extends the bandpass of XISs to much higher energy (Kokubun et al. 2007). The basic information of the instruments of *Suzaku* is summarized in Table 3.1 and 3.2.

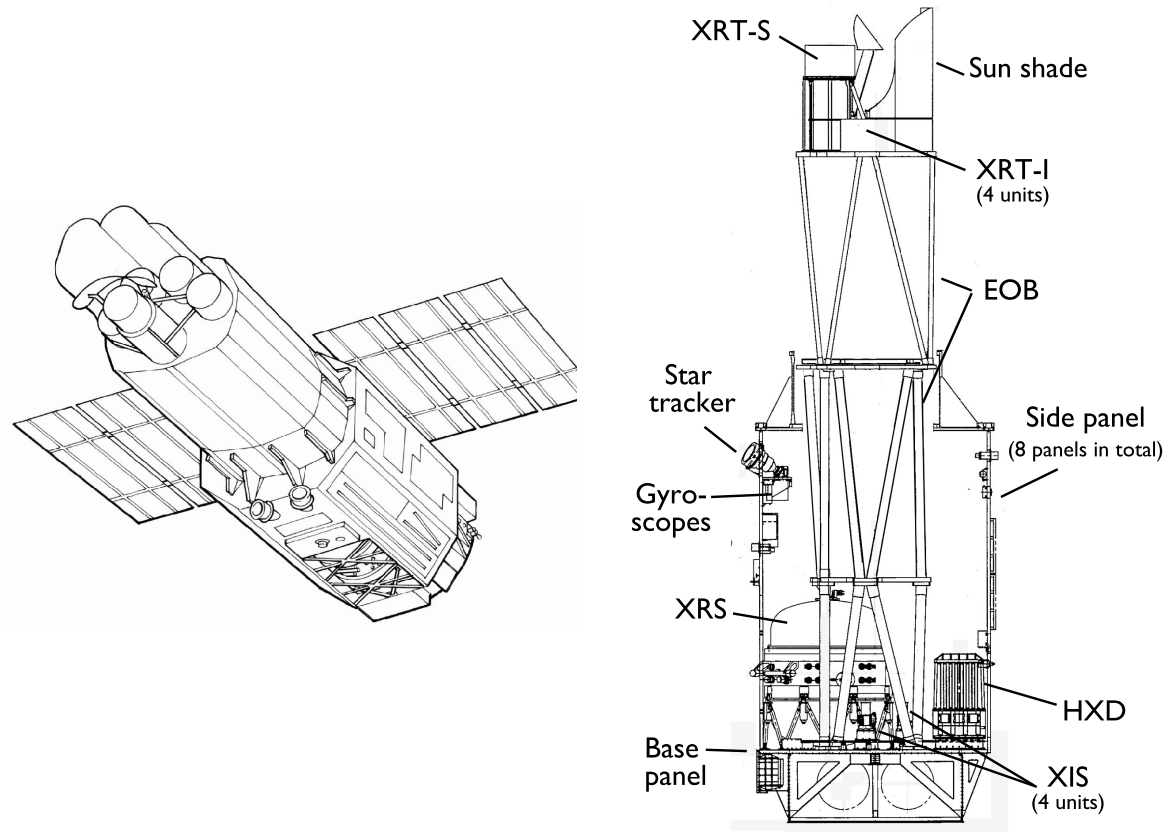

Figure 3.2: Left: Schematic view of *Suzaku*. Right: Internal side view of *Suzaku* after EOB deployment (Mitsuda et al. 2007).

3.3 X-ray telescope (XRT)

3.3.1 Basic properties

The XRT on board *Suzaku* has been developed jointly by more than five institutions such as Nagoya University, Tokyo Metropolitan University, ISAS/JAXA, NASA/GSFC and so on. The XRT is a thin-foil-nested Wolter-I type telescope as shown in Figure 3.3 right (Serlemitsos et al. 2007). *Suzaku* has five XRTs: four XRT-Is (XRTI-I0, XRTI-I1, XRTI-I2, and XRTI-I3) and one XRT-S, and they are mounted on the top of EOB on the spacecraft as shown in Figure 3.2 right, and Figure 3.3 left. The XRT-Is are identical and used for individual XISs, and XRT-S is used for XRS. Each of the reflectors are composed aluminum foils coated with thin ($\gtrsim$ 1000 $\AA$) gold layer with a thickness of 152 μm, and the number of nesting is 175 and 168 for XRT-I and XRT-S, respectively.

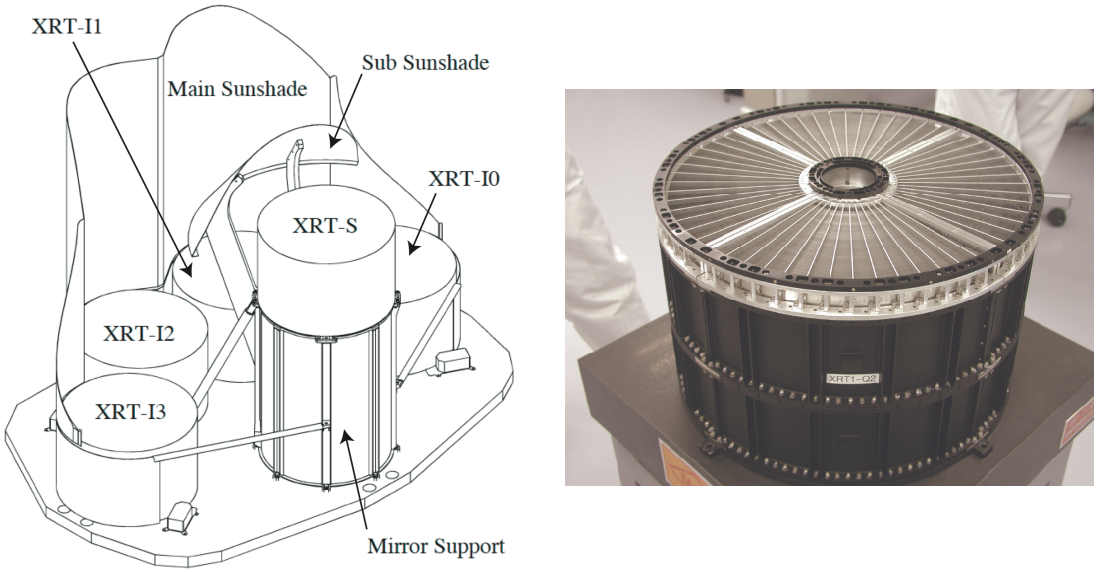

Figure 3.3: Left: the configuration of XRT on the EOB top plate. See also Figure 3.2 for overview. Right: Photograph of the module of XRT-I1 (Serlemitsos et al. 2007).

To focus X-rays onto the detector, the incoming photons are reflected twice by the primary and secondary reflector as shown in Figure 3.4. The major reflection paths are called as "Normal Reflection", "Secondary Reflection", and "Backside Reflection". The latter two paths could cause stray light, in other words, these processes make a ghost image. To reduce the intensity of the stray light, the pre-collimator is utilized. Figure 3.5 shows the effect of pre-collimator to reduce the intensity of the stray light. The middle panels of Figure 3.5 show simulated stray light images without and with the pre-collimator, respectively, where the simulated source is locates at the (DETX, DETY) = (-20', 0') (See also Figure 3.11), and is monochromatic point-like source of 4.5 keV. The middle panel shows that the

pre-collimator significantly reduce the intensity of stray light, however, it is not completely diminished. The right panel shows the XIS3 image of Crab nebula off-axis pointing in the 2.5-5.5 keV during 2005 August 22nd – September 16th.

Figure 3.6 shows the effective area of XRT and other astronomical X-ray telescopes of XMM-Newton (PN + 2MOS) and Chandra (ACIS-I and ACIS-S). There are complex edge structures of gold line energies, $\sim$2.1 keV. The effective areas of XRT-I are typically 440 cm^2 at 1.5 keV, and 250 cm^2 at 8 keV.

3.3.2 Imaging performance of the XRT responses

The point-spread functions (PSFs) and encircle-energy fractions (EEFs) of four XRT-Is are shown in figure 3.7. The PSFs and EEFs are obtained with the data of SS Cyg during 2005 November 2 01:02 UT – 23:29 UT. The target is a point source and bright enough (3.6, 5.9, 3.7 and 3.5 counts sec^{-1} for XIS0, 1, 2, 3), however there is no need to worry about pile-up effects. The angular resolutions of the XRTs are 1'.8 – 2'.3 in terms of half-power diameter (HPD), which is the diameter within half of the focused X-rays are enclosed. The angular resolution dose not significantly depend on the energy range of 0.2 – 12.0 keV.

3.3.3 Accuracy of the XRT responses

An Ancillary Response File (ARF), which describes the XRT response and the amount of the XIS optical blocking filters (OBF) contamination, should be created by running Monte-Carlo simulator for each observation, called XISSIMARFGEN and XISARFGEN (Ishisaki et al. 2007, Suzakumemo 2011-01[1]). The XISSIMARFGEN is more accurate and better to use, however, it takes a long time to create. Thus, the XISARFGEN is devised to create the ARFs with a short time. In this thesis, we utilize XISSIMARFGEN only to achieve a better precision. The data of SS Cyg are also utilized to estimate the accuracy of the simulated effects of the XRT. The simulator version 2008-04-05 is utilized for the study. The De-encircled energy function (DEF), which is corresponding to 1-EEF, is shown in Figure 3.8: the black curves show the data of SS Cyg and colored ones show simulation (Suzakumemo 2008-04[2]). Obviously, version of 2008-04-05 is significantly better than the previous one, and the accuracies of the normalization were archived with $\sim$15% and $\lesssim$5% for XRT-I0, 2 and XRT-I1, 3, respectively when the image of outer side of the radius of 2 arcmin is utilized.

[1]http://www.astro.isas.jaxa.jp/suzaku/doc/suzakumemo/suzakumemo-2011-01.pdf
[2]ftp://heasarc.nasa.gov/astroe2/doc/xrt/suzakumemo-2008-04.pdf

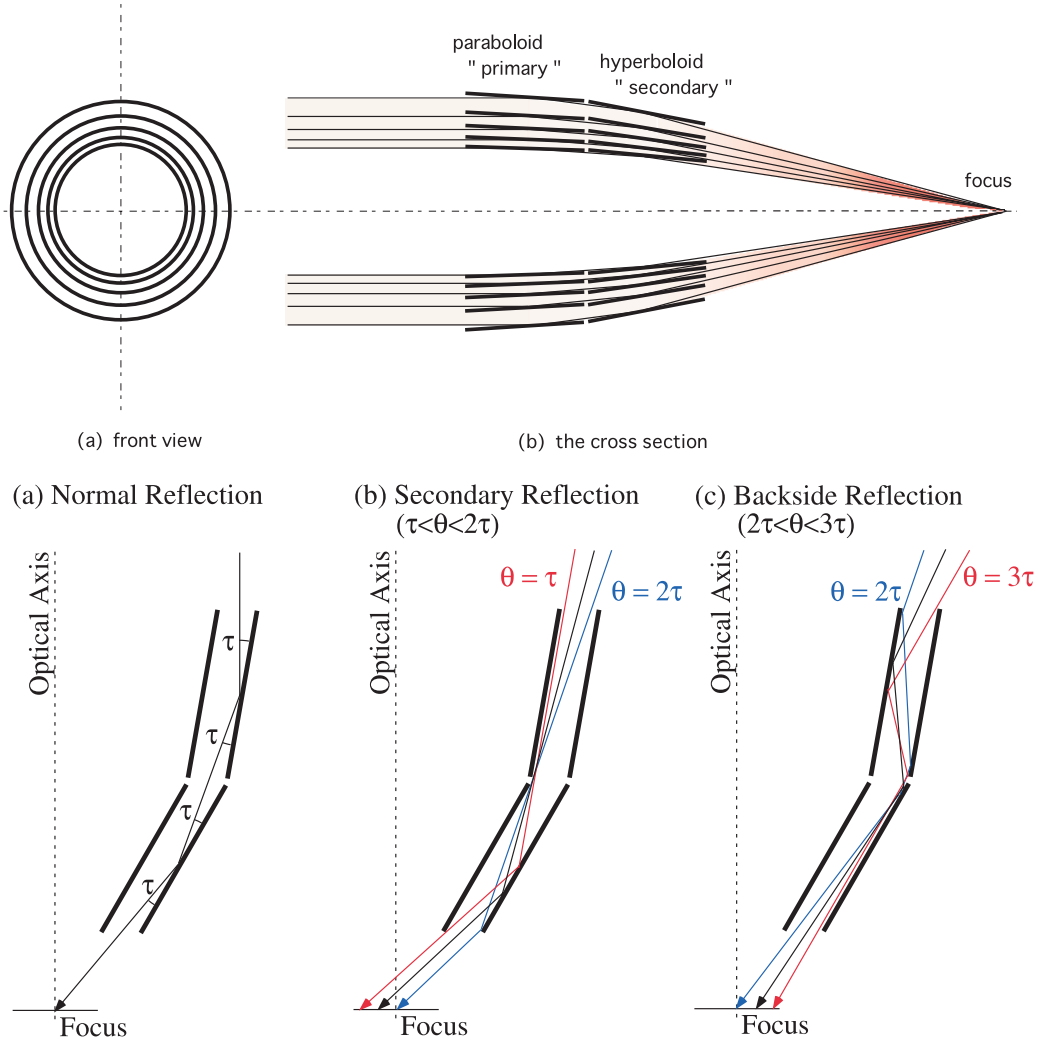

Figure 3.4: Top: schematic picture of XRT unit. (a): front view. (b): the cross section (Mori et al. 2005). Bottom: the major reflection paths of incoming photons in the XRT. τ shows the angle between the primary reflector and the the optical axis. (a): The normal double reflection, incoming photons are bent by the angle of four τ totally. (b): The secondary reflection, the angle of incoming photons are $\tau < \theta < 2\tau$. (c): The backside reflection, incoming photons are reflected at the backside of the primary reflector. In this case, the angle of incoming photons are $2\tau < \theta < 3\tau$ (Mori et al. 2005; Serlemitsos et al. 2007).

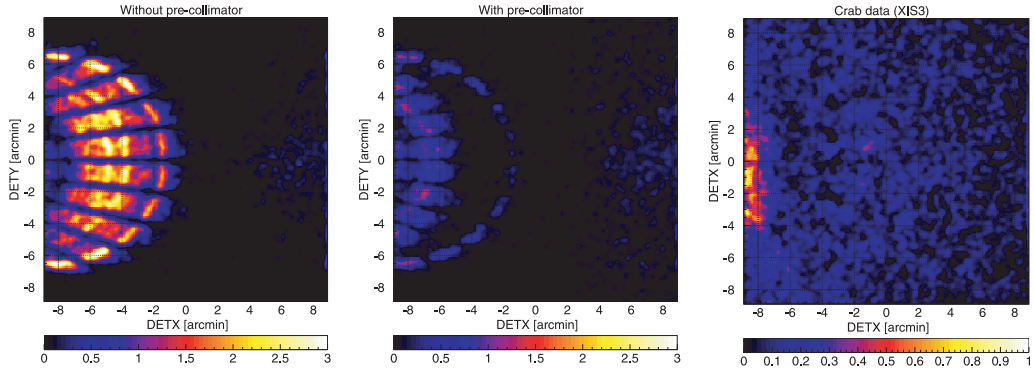

Figure 3.5: Left/middle: simulated stray light images without/with the pre-collimator, respectively, where the simulated source is locates at the (DETX, DETY) = (-20', 0') (See also Figure 3.11), and is monochromatic point-like source of 4.5 keV. Right: the XIS3 image of Crab nebula off-axis pointing in the 2.5-5.5 keV during 2005 August 22nd – September 16th (Serlemitsos et al. 2007).

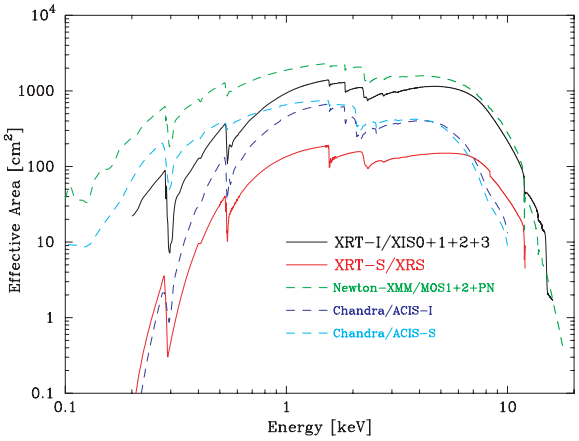

Figure 3.6: The on-axis effective area of the XRT-S unit, and summed over the four XRT-I units. There are complex edge structures of gold line energies, ∼2.1 keV (Serlemitsos et al. 2007).

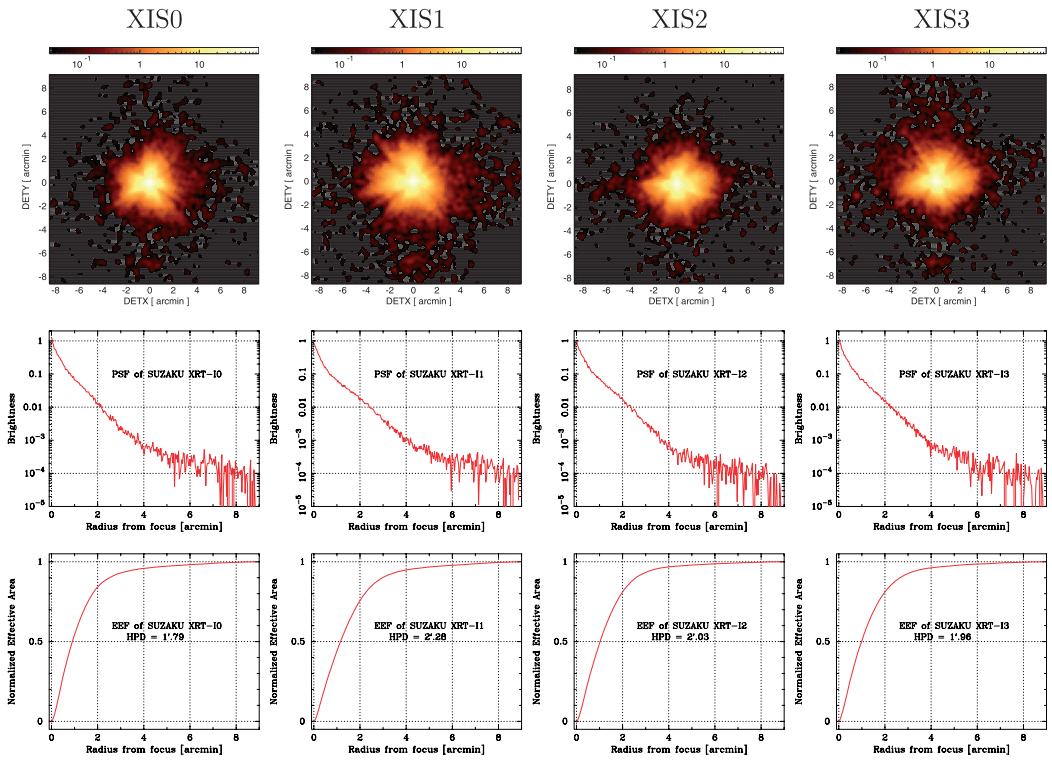

Figure 3.7: The point-spread functions (PSFs) and encircle-energy fractions (EEFs) of four XRT-Is. The PSFs and EEFs are obtained with the data of SS Cyg during 2005 November 2 01:02 UT – 23:29 UT (Serlemitsos et al. 2007).

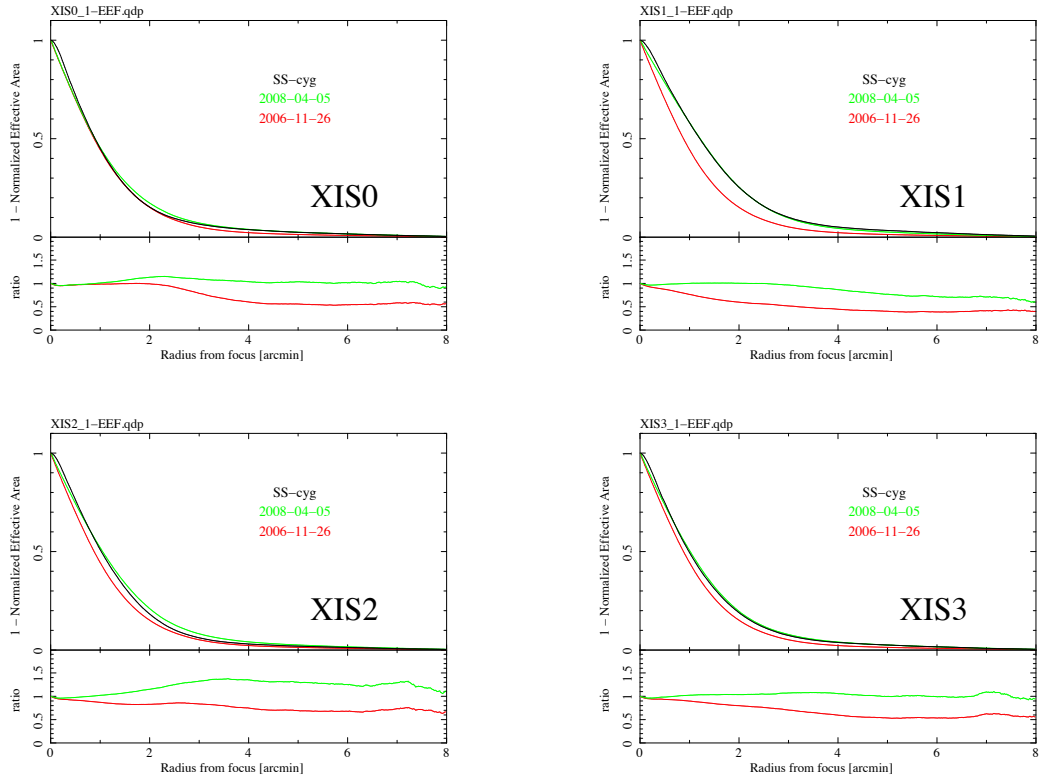

Figure 3.8: The De-encircled energy function (DEF equivalent with '1-EEF'). Black: the data of SS Cyg on 2005 November 2nd. Red: Simulation version 2006-11-26. Green: Simulation version 2008-04-05. The accuracies of the normalization can be reproduced with $\sim$15% and $\lesssim$5% for XRT-I0, 2 and XRT-I1, 3, respectively when the image of outer side of the radius of 2 arcmin is utilized (Suzakumemo 2008-04[2]).

3.4 X-ray Imaging Spectrometer (XIS)

3.4.1 Basic Properties

The XIS (Koyama et al. 2007) consists of four cameras (XIS0, XIS1, XIS2, and XIS3), which have silicon based X-ray charge coupled devices (CCDs) operated in a photon-counting mode. It has been developed jointly by Kyoto University, Osaka University, ISAS, Rikkyo University, Ehime University, Kogakuin University, and MIT. The XIS is developed, based on the experience of SIS on board *ASCA*, which has the first photon-counting CCD for X-rays. The basic parameters of XIS are listed in Table 3.1. Figure 3.9 shows a picture of the XIS unit and side view of XIS camera (Koyama et al. 2007). X-ray CCDs also has a sensitivity to optional and UV photons, and thus an optical blocking filter (OBF), which is made of polyamide and Al with a total thickness of 1200 $\mathring{A}$, is attached onto the surface of the CCDs to mask the optical and UV photons.

Table 3.1: Basic parameters of the XIS (Koyama et al. 2007)

Instruments	XIS
Field of view	17.8'×17.8'
Energy range	0.2 – 12 keV
Format	1024 × 1024
Pixel size	24 μm× 24 μm
Energy resolution (FWHM)	∼ 130 eV at 6 keV
Effective area[1]	330 cm^2(FI), 370 cm^2 at 1.5 keV
	160 cm^2(FI), 110 cm^2 at 8 keV
Time resolution	8 sec (normal)
	2 sec (1/4 window)
	7.8 msec (P-sum)

[1]The effects of the XRT-I and OBF are included for XIS.

Each XIS unit is located at the focal plane of the individual co-aligned XRT modules (Serlemitsos et al. 2007). The XIS-1 used a back-side illuminated (BI) CCD, and the other three XIS units (XIS-0, XIS-2, and XIS-3) used front-side illuminated (FI) chips. Figure 3.10 shows an effective area and a quantum efficiency of FI CCD and BI CCD. The FI CCD has the electro nods on the surface, and the BI CCD has that on the bottom. Therefore, the FI and BI CCD are superior to soft and hard energies, respectively, the FI CCD has a sensitivity in 0.4 – 12.0 keV, and the BI CCD has a sensitivity in 0.2 – 12.0 keV. Each CCD unit has a single CCD chip with pixels of 1024 × 1024, whose size is 24 μm× 24 μm, and has a field of view of 17'.8 × 17'.8.

3.4.2 Observation modes for bright sources

Figure 3.11 shows the schematic view of XIS CCD unit and four arguments of read out nodes (Koyama et al. 2007). The pixel data are collected in each segment

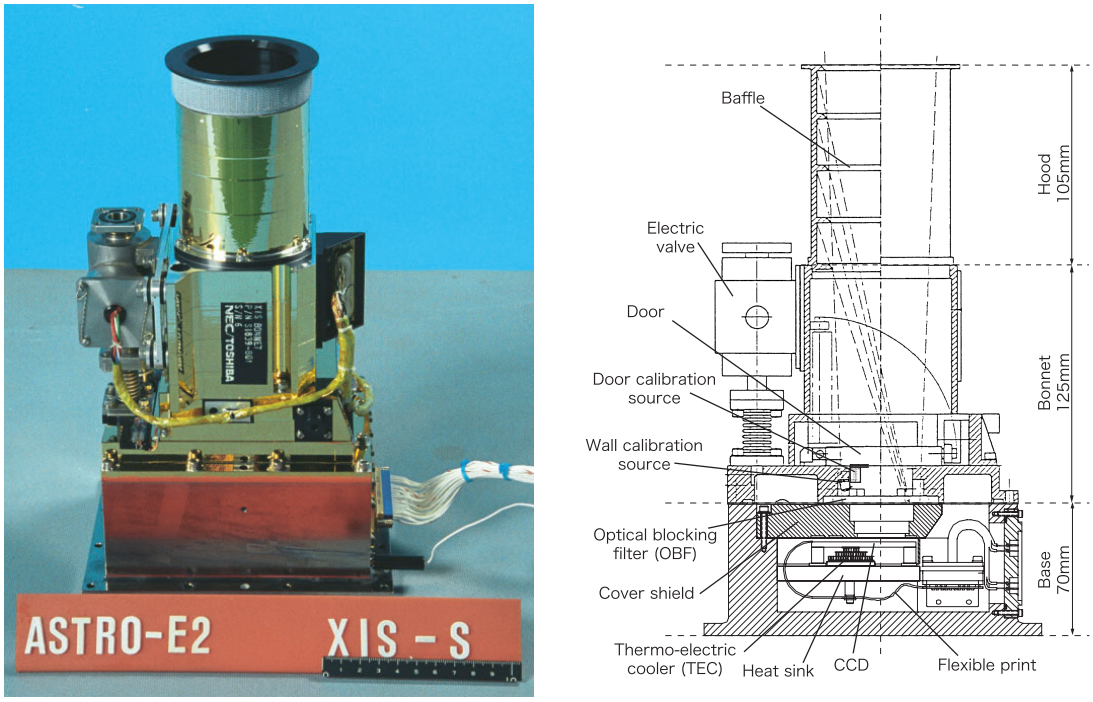

Figure 3.9: Left: Photograph of the XIS unit. Right: that of side view (Koyama et al. 2007).

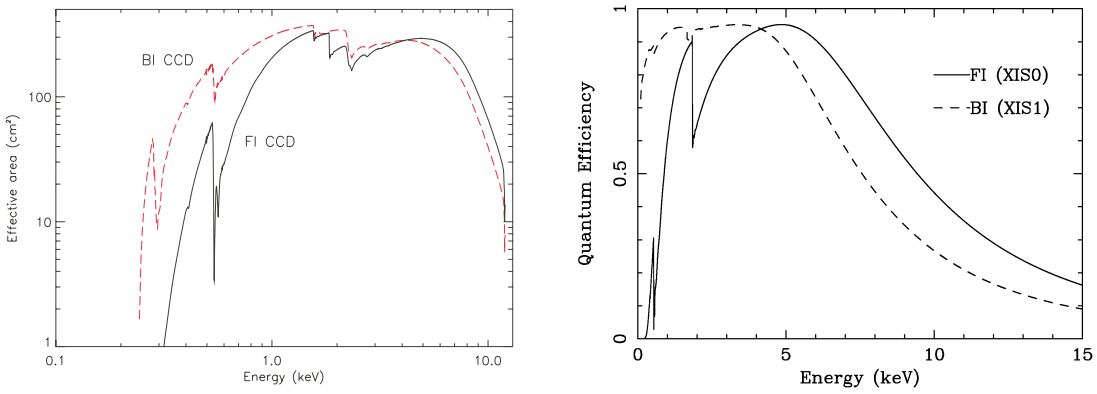

Figure 3.10: Left: the effective area of XIS and XRT. The solid lines shows FI CCD, and broken lines shows BI CCD (Mitsuda et al. 2007). Right: that for quantum efficiency (Koyama et al. 2007).

through the ActY direction, and read out from the corresponding readout node, then sent to the Pixel RAM. In a standard observation mode (normal mode) of XIS, charges are read out from all 1024 × 1024 pixels every 8 sec. While, the integration time of the normal mode is too long for bright sources (>10 mCrab in 0.5 – 10.0 keV), and causes pile-up events, wherein more than one photons are detected by a single pixel during the integration time. To avoid the pile-up, "Window Options" are stored under the sacrifice of the imaging area. In the case of "1/4 window option", quarter of the CCD chip of 1024 × 256 pixels are read out every 2 sec. In this case, the window of image is 1024 pixel in the ActY, and 256 pixel in the ActX. Thus, the time resolution of 2 sec is achieved (Table 3.1). There is also 1/8 or 1/16 window option, the window width is 128 or 64 pixels in ActX, and the time resolution is 1 sec or 0.5 sec, respectively.

For too bright sources to avoid pile-up events even using "Window Options", "Burst Option" is utilized. In this option, the effective exposure is reduced by an artificially made dead time. For example, using "1/4 window option" and "0.5 sec" burst option, events in the first 1.5 sec is discarded and those in the last 0.5 sec is utilized. There are also "Burst Option" of 1 sec, 0.3 sec, and 0.1 sec.

To achieve a much better time resolution, the timing mode, which called parallel sum (P-sum) mode, is utilized, where the 2-dimensional of CCD chip are summed into the ActY axis. In other words, the image area of CCD chip is 1024 × 1 pixels in this mode. The time resolution of the P-sum mode is 8sec/1024ch ∼7.8 msec. Therefore, this mode is utilized for study of timing properties of highly variable and bright sources. The drawback of the P-sum mode is the worse calibration accuracy than normal mode. Also, because of the lack of the dimension, a subtraction of non X-ray background is difficult, and thus non-Xray background is higher than normal mode. Therefore, in this thesis, the latest calibration database (CALDB)[3] is utilized under a collaboration with XIS team.

3.4.3 Status reports of XIS

Unfortunately, the XIS-2 showed an anomaly on November 9th 2006, and around two third of the image was flooded with a large amount of charges. The anomaly made XIS-2 effectively useless for the scientific observations[4]. Similarly, the XIS-0 showed an anomaly on June 23rd 2009, and a part of the segment A of XIS-0 was flooded with a large amount of charges. Therefore, XIS-0 lost around eighth part of the image in the normal clocking mode, and the P-sum clocking mode is not continued. Thus, observations of P-sum clocking mode is available only for XIS-3[5].

[3]http://heasarc.gsfc.nasa.gov/docs/heasarc/caldb/data/suzaku/xis/index/cif_suzaku_xis_20160607.html
[4]http://www.astro.isas.jaxa.jp/suzaku/doc/suzakumemo/suzakumemo-2007-08.pdf
[5]http://www.astro.isas.jaxa.jp/suzaku/doc/suzakumemo/suzakumemo-2010-01.pdf

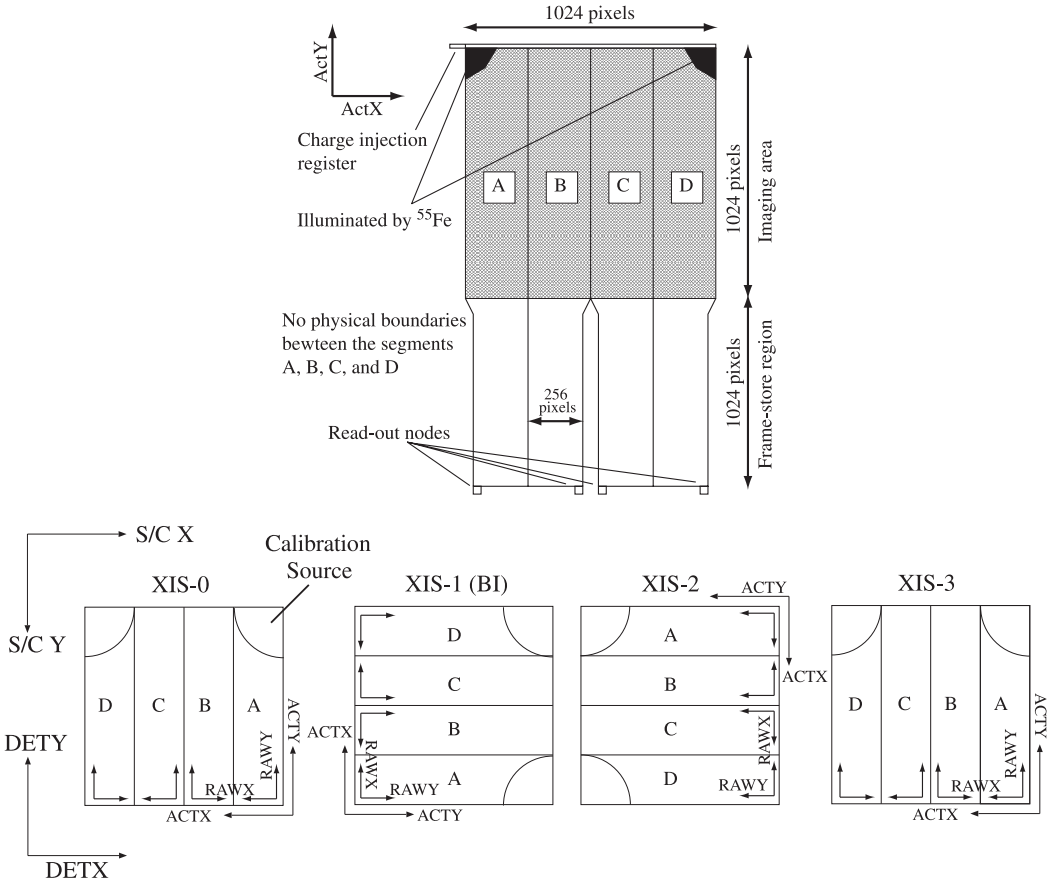

Figure 3.11: Top: the thematic view of the read out nodes of CCD unit (Koyama et al. 2007). Bottom: the detail definition of the CCD coordinate (Ishisaki et al. 2007).

3.5 Hard X-ray Detector (HXD)

3.5.1 Basic properties

The HXD (Takahashi et al. 2007) is non-imaging, collimated hard X-ray detector, which covers the energy range of 10 – 700 keV with better sensitivity than any other past detectors in the hard X-ray band. The basic parameters of HXD are listed in Table 3.2. It has been developed jointly by the University of Tokyo, Toyama Gakuin University, Hiroshima University, ISAS/JAXA, Kanazawa University, Osaka University, Saitama University, SLAC, and RIKEN.

Table 3.2: Basic parameters of the HXD (Takahashi et al. 2007)

Detector	PIN	GSO	WAM
Field of view	34'×34' at E $\lesssim$ 100 keV		2 π (non-pointing)
	4.°5 × 4.°5 at E $\gtrsim$ 100 keV		
Energy range	10 – 70 keV	40 – 600 keV	50 keV – 50 MeV
Geometrical area	21.5 × 21.5 mm^2	24 × 24 mm^2	
	(2mm-thick)	(5mm-thick)	
Energy resolution (FWHM)	$\sim$ 4 keV	$7.6/\sqrt{E_{MeV}}$%	$\sim$30% at 662 keV
Effective area	160 cm^2 at 20 keV	260 cm^2 at 100 keV	800cm^2 at 100 keV
			400cm^2 at 1 MeV
Time resolution	61 μsec		5.625 ms or 31.25 ms for GRB
			1 s for All-Sky-Monitor

Figure 3.12 shows the photograph of HXD. In the hard X-ray region, typically the number of source photons decrease with the energy, thus the source signal is usually weaker than the background signal. Therefore, in higher energy, the lower background level, corresponding to the thorough background rejection, is needed to have an accurate observation. The major background components are incident background within the field of view, incident background from outside of the field of view, and intrinsic background from the material of the detector. To minimize these background, the HXD is designed by utilizing "Well-type active shield" and "Compound-eye configuration".

Figure 3.13 shows the configuration of the HXD sensor. There are 16 "Well-type phoswich counter" (hereafter "Well units") and these are surrounded by 20 bismuth germanate crustal ($Bi_4GE_3O_{12}$; hereafter BGO) anti counter units. The 16 "Well units" and 20 anti-counter units work independently. The main detector of "Well unit" composes silicon-PIN diodes (hereafter PIN) and gadolinium silicate scintillators (Gd_2SiO_5(Ce); hereafter GSO). Each unit forms a 2 × 2 matrix, and the GSO is placed behind of PIN as shown in Figure 3.13. The Well-type BGO anti counter units reduce the backgrounds efficiently utilizing anti-coincident signals, also it works as all sky monitor (Wideband All-sky Monitor; hereafter WAM) for gamma-ray burst, transient objects, and can be utilized for long trend monitor with earth occultation technique thanks to the large effective area. It is important to

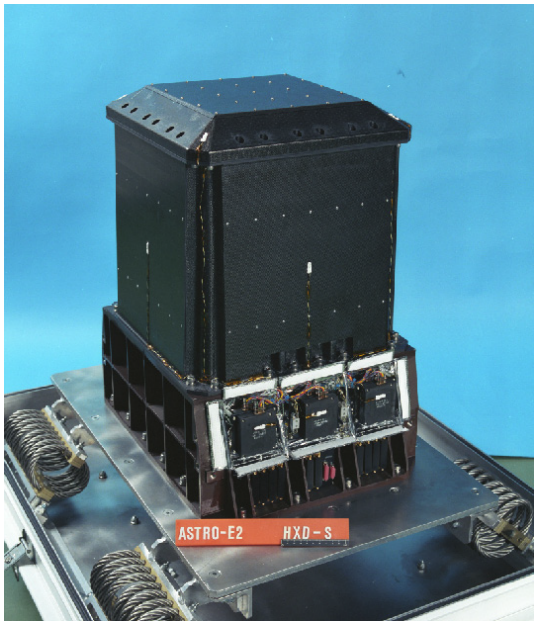

Figure 3.12: Photograph of HXD (Takahashi et al. 2007).

note that the optical axis of HXD is shifted as -3'.5 for DETX direction, comparing with XIS nominal position.

3.5.2 HXD-PIN and -GSO

The source signals are detected by 16 "Well units" (arranged as 4×4 array). Figure 3.14 left shows the effective area of "Well units" (PIN and GSO). The X-rays with the energy of ∼10 – ∼70 keV are detected by PIN, and those of ∼40 – ∼700 keV is mainly detected by GSO. The geometrical area of each PIN is 21.5 × 21.5 mm^2 (2mm-thick), and the affective area is limited to ∼16.5 × 16.5 mm^2 because of the guard ring structure. That of each GSO is 24 × 24 mm^2 (5mm-thick). These 16 "Well units" are surrounded by WAM as written above. The GSO signals and bottom BGO signals are read out by same photomultiplier tubes (PMTs) as shown in Figure 3.13. The decay time of GSO is ∼60 ns, and BGO is ∼300 ns. Utilizing these difference of the decay time, the pulse shape discrimination between GSO and BGO is conducted as shown in Figure 3.15.

BGO has a large atomic number, and has a great capability blocking for the X-rays, the gamma-rays, and particles, thus the structure of "well" BGO collimate the HXD field of view as $4.^\circ5 \times 4.^\circ5$. In addition, to reduce the contamination of cosmic X-ray background, passive collimators called as "fine collimator" are installed in the Well-type BGO shields above PIN. The fine collimator is made of 50 μm thick phosphor bronze foils, arranged to from 8 × 8 square meshes, 3 mm wide and 300 mm long. Figure 3.16 shows the angular transmission function of the fine collimator. The fine collimators define a 34' × 34' full width half maximum FWHM square filed of

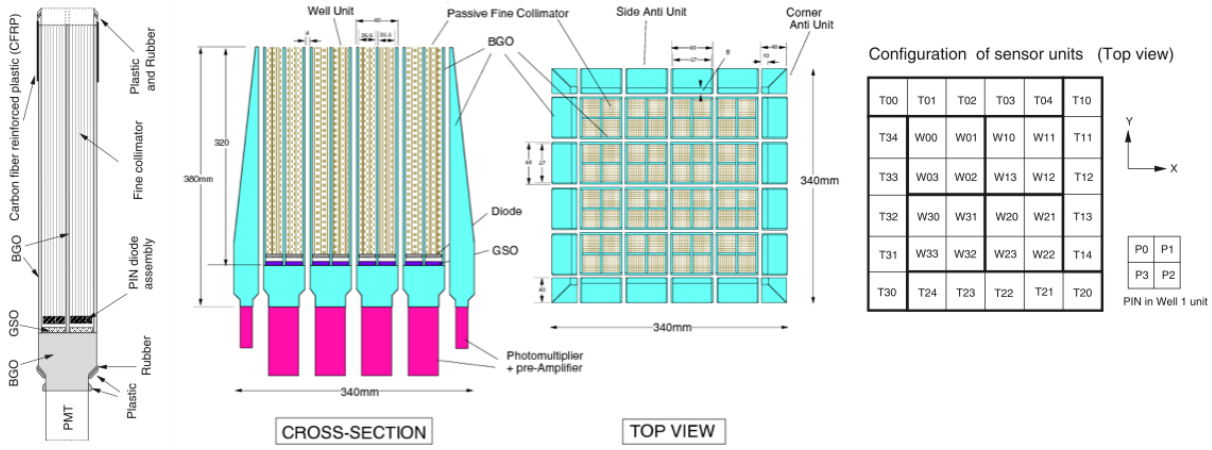

Figure 3.13: Left: side view of Well unit. Middle left: side view of HXD. Middle right: top view of HXD. Right: numbering go the Well and WAM units. (Takahashi et al. 2007).

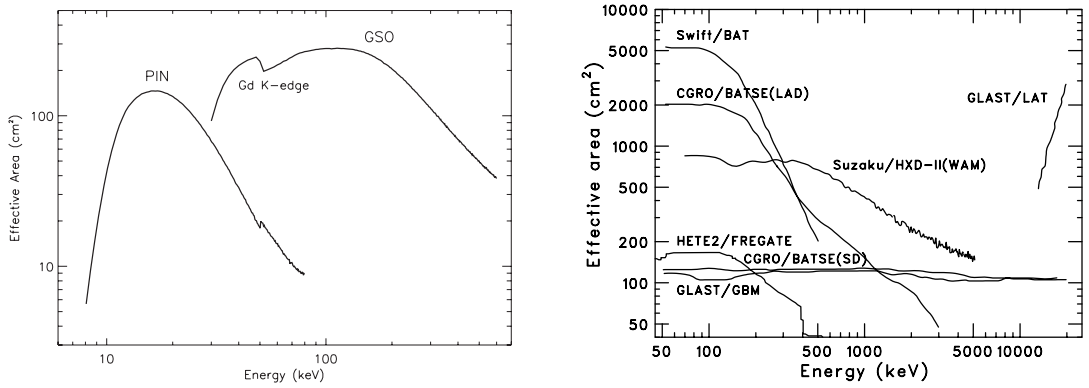

Figure 3.14: Left: the total effective area of main detector of HXD (PIN and GSO) as a function of energy. The effects of photon absorption by materials infant of the detectors are taken into account. Right: the effective area of WAM compering with other all sky monitors (Takahashi et al. 2007).

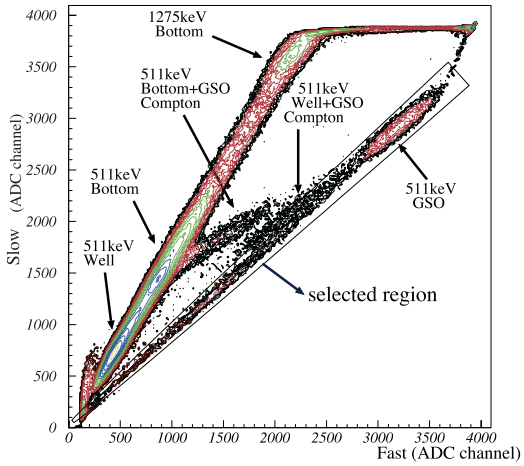

Figure 3.15: A fast-slow diagram for a signals of Well unit with ^{22}Na irradiation (Takahashi et al. 2007).

view.

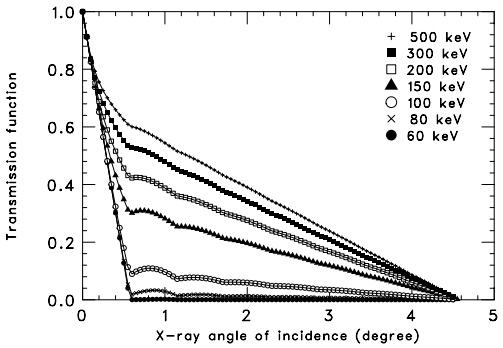

Figure 3.16: Angular transmission function of the fine collimator (Takahashi et al. 2007).

3.5.3 HXD-WAM

The WAM unit composes a thick (∼4 cm) BGO crystal and a PMT. The effective area of WAM achieve ∼800 cm^2 at 100 keV, and ∼400 cm^2 even at 1 MeV as shown in Figure 3.14 right. WAM is not pointing to the target source which are observed with HXD-PIN/GSO and XIS. It has a large field of view (2 π), and works as all sky monitor for gamma-ray burst and transient objects. Utilizing the earth occultation technique, WAM also can work for long trend monitor for bright sources, such as the Crab nebula and Cygnus X-1.

Chapter 4

Observation and Data reduction

4.1 Observation

Suzaku had conducted thirty-two pointing observations of Cyg X-1 during the lifetime. Figure 4.1 shows the *Swift*/BAT light curve (Krimm et al. 2013) of Cyg X-1[1], with the epochs of all the *Suzaku* observations. There are only five *Suzaku* observations in the high/soft state (BAT count rate of < 0.05), three of which have been already published (2010, 2011: Yamada et al. (2013); 2012: Tomsick et al. (2014)). Here we focus on the remaining two pointing observations of the high/soft state of Cyg X-1, taken on 2013 April 8 (ObsID=407015010, hereafter Obs A), and 2013 May 7 (ObsID=407015020, hereafter Obs B).

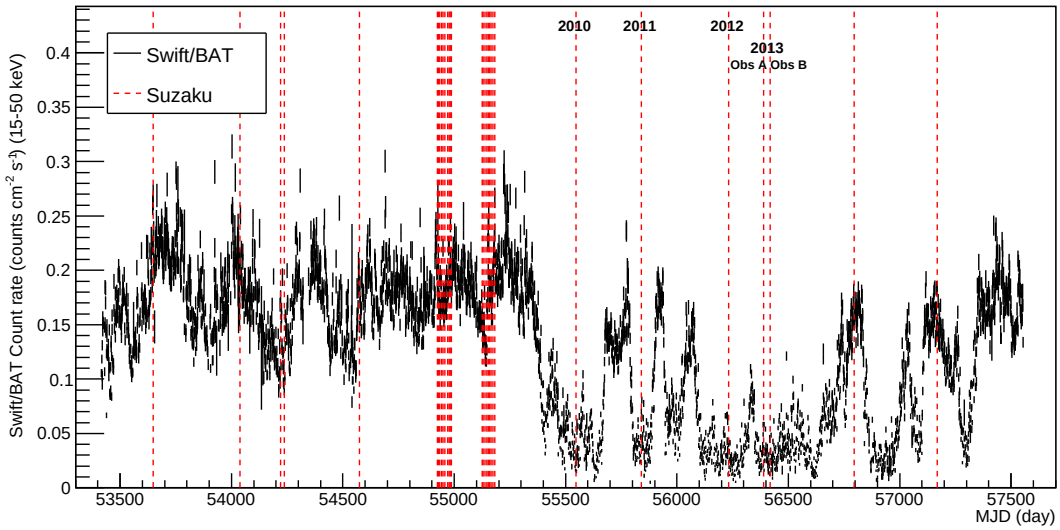

Figure 4.1: Light curve of Cyg X-1 observed by *Swift*/BAT (Krimm et al. 2013). Red dashed lines show the times of *Suzaku* observations. There are five high/soft state (BAT count rate of < 0.05) observations by *Suzaku*.

The XIS-0 and XIS-1 were operated with 1/4 window mode with 0.3-s burst option, and XIS-3 was operated with P-sum (fast timing: Koyama et al. 2007, also See §3.4). We conducted the data reduction only for XIS-0 and XIS-3 because XIS-0 is the best calibrated, and only XIS-3 has a good timing resolution.

4.2 Data reduction of XIS-0

We used XSELECT to extract XIS images, light curves, and spectra, which are screened with the standard selection criteria as described by Suzaku ABC guide[2]. Since Cyg X-1 is a very bright source, we conducted some special event selections and reductions.

[1] http://swift.gsfc.nasa.gov/results/transients/CygX-1
[2] https://heasarc.gsfc.nasa.gov/docs/suzaku/analysis/abc

To extract the events which were not affected by telemetry saturation, we utilized command of XISGTIGEN for uncleaned event files with options of
WINGTI=YES SEGMENTB_A=NO SEGMENT_B=YES SEGMENT_C=YES SEGMENT_D=NO,
because the top priority of observation was set for segment B and the secondary was segment C, and almost all events in segment A and D were saturated. Then, we set a selection criteria as
(GRADE==0||GRADE==2||GRADE==3||GRADE==4||GRADE==6)&&
(STATUS>=0&&STATUS<=524287),
and had a selection of
AOCU_HK_CNT3_NML_P==1 && ANG_DIST<1.5 &&
S0_DTRATE<3 && S1_DTRATE<3 && S2_DTRATE<3 &&
S3_DTRATE<3 && SAA_HXD==0 && T_SAA_HXD>436 &&
ELV<-5 && DYE_ELV>20.
Conducting these event selections, we achieved to create cleaned event files without telemetry saturation.

We excluded the core of the CCD image with a radius of 1.4 arcmin in order to reduce the pile-up fraction below ∼3% based on Yamada et al. (2012). Figure 4.2 shows an example of images of XIS-0 (Obs B) with Window mode observation. Each of the orbital segments is separately shown in Figure 4.2 left, and all of them are superimposed in Figure 4.2 right where the core of image has been excluded. Here we note that the center of image could be slightly (∼arcsec) shifted because of the pointing fluctuation of the satellite, and thus we need to treat carefully.

To estimate the background level, we analyzed the data during the earth occultation with the GTI selection of $ELV < -5$. The estimated XIS-0 background is less than 0.01% in the lower energy range (∼2.0 keV) and less than ∼1% in the higher energy range (∼10 keV) of signal events. Hence we ignore the background in our analysis.

Utilizing XISRMFGEN and XISSIMARFGEN, we created the XIS responses and auxiliary files. Here, we created auxiliary files for each of the orbital segments by consideration of the pointing accuracy.

4.3 Data reduction of XIS-3

We conducted the data reduction for the data of XIS-3, following *Recipe for reducing XIS data taken with the P-sum/timing mode*[3]. As the data reduction of XIS-0, we need to avoid telemetry saturation. We thus also conducted the data reduction of XIS-3 in the same way as XIS-0, utilized a "yes" option of a command of XISGTIGEN only for segment B because the top priority of observation was set for segment B, and almost all events in other segments were saturated. Also we used selection criteria as
(GRADE==0||GRADE==1||GRADE==2)

[3]ftp://legacy.gsfc.nasa.gov/suzaku/doc/xis/Psum-recipe-20150326.pdf

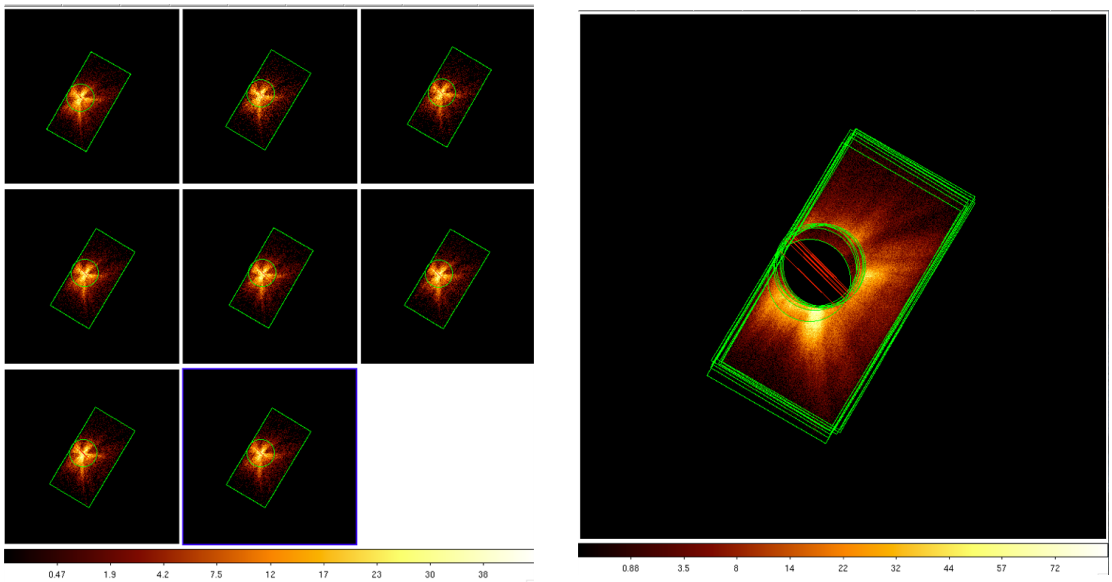

Figure 4.2: The example of images of XIS0 (Obs B) with the Window mode observation. Left: Each of the orbital segments are separately shown. Right: all of them are superimposed where the core of images has been excluded.

&& (STATUS >=0&&STATUS <=524287)
, which is specialized for P-sum mode. Then, we utilized a command of *aebarycen* for a 'barycentric correction' to achieve the precise data.

Figure 4.3 shows an example of images of XIS-3 (Obs B) with P-sum mode observation in ActX–RawY space (left, See §3.4 for a coordinate of XIS), and a projection for ActX (right), In the left panel of Figure 4.3, segment A, C, and D have been extracted. We can see bad pixels around ∼400 pixel in the right panel of Figure 4.3, and it has been removed in the left panel.

To check an accuracy of P-sum mode observations, we made a histogram of GTI of XIS-0 and XIS-3 as shown in Figure 4.4 left, which is a example of the histogram and corresponding to Obs B4 in following sections. The correlation between XIS-0 and XIS-3 is shown in the right panel of Figure 4.4, and we can see that XIS-0 and XIS-3 are clearly correct with each other. Here we note that a command of MGTIME is useful to have the same GTI in many cases. However, timing resolution is significantly different between XIS-0 and XIS-3 in this case, and thus we can not use MGTIME. We also made a spectrum of XIS-0 and XIS-3 to check an accuracy of energy gain as shown in Figure 4.5. Utilizing the edge structures of response, we can estimate the difference of energy scale and it seems to be ∼350 eV. The spectrum of XIS-0 is the best calibrated among three XISs, and P-sum mode is less calibrated (See §3.4). We believe the energy range of the XIS-0, and read that $\mathrm{XIS3_{actual}} = \mathrm{XIS3_{appearance}} - 350$ eV.

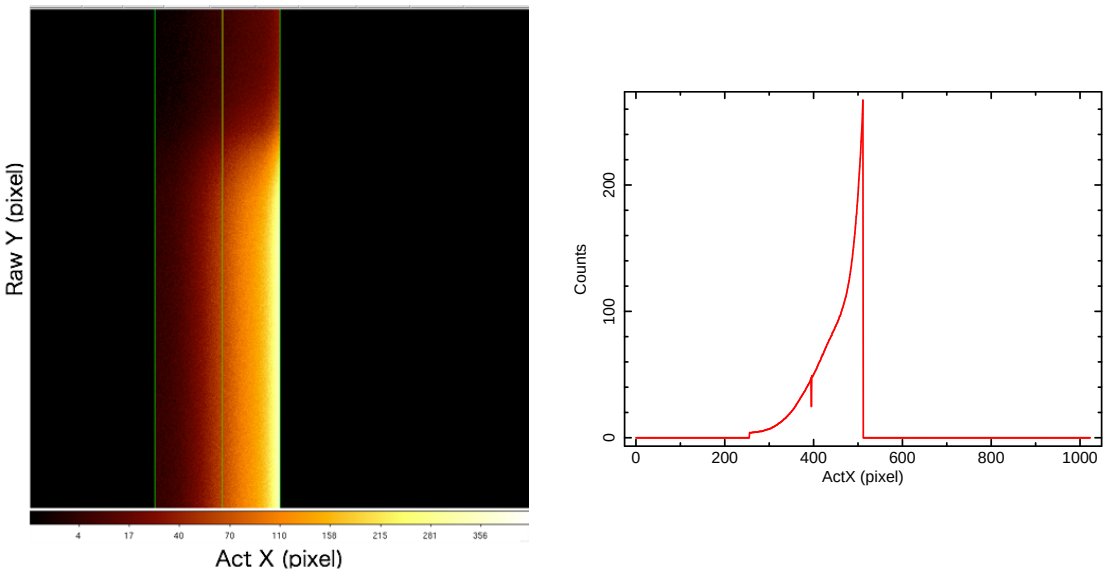

Figure 4.3: The example of an image of XIS3 (Obs B) with P-sum mode observation in ActX–RawY space (left, See §3.4 for a coordinate of XIS), and projection for ActX (right), In the left panel, segment A, C, and D have been extracted, also bad pixel (around ∼400 pixel) has been removed.

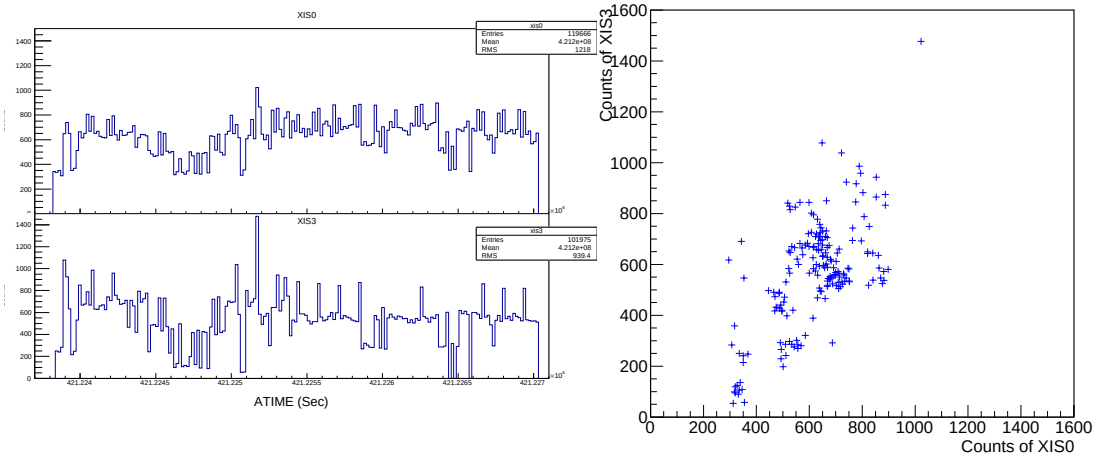

Figure 4.4: Accuracy test of P-sum mode observations for timing. Left: histogram of GTI of XIS0 (Window model, top) and XIS3 (P-sum mode, bottom). Right: The correlation between XIS0 and XIS3.

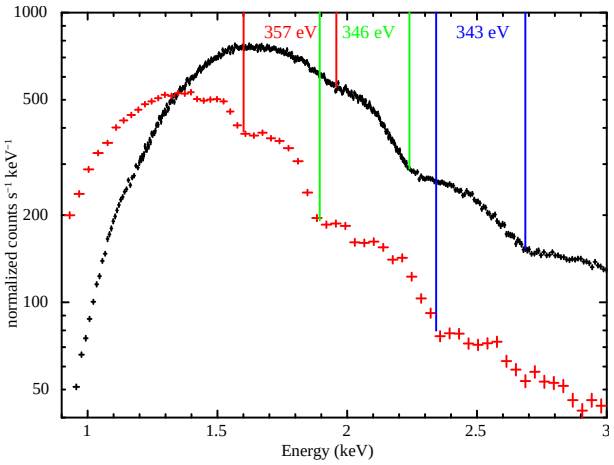

Figure 4.5: Accuracy test of P-sum mode observations for an energy gain issue. Red: XIS0 (Window mode), Black: XIS3 (P-sum mode). The differential energy gain is ∼350 eV.

4.4 Data reduction of HXD-PIN

The HXD-PIN (Takahashi et al. 2007; Kokubun et al. 2007) data reduction is conducted for both observations with the standard procedure, and the ftool of HXD-PINXBPI was used for tuned background files to create the PIN background spectrum accounting for both the non-X-ray background (NXB) and the cosmic X-ray background (CXB) (Fukazawa et al. 2009). Because of a non-imaging detector of HXD, and which has following normal selection criteria; (i) attitude control in pointing mode, (ii) instantaneous pointing is less than 1.5 arcmin, (iii) high voltage is not reduced, (iv) the satellite is outside of SAA (South Atlantic Anomaly), the time after passage from SAA is larger than 500 sec, and time to next SAA passage is larger than 180 sec, (v) the cut-off rigidity is larger than 6 GeV, (vi) the target object should be above the Earth rim by at least 5°. More details are written in the Suzaku ABC guide[4].

4.5 Overview of the observed data after the reductions

The exposure of PIN is 64.51 ks and 20.51 ks for Obs A and Obs B, respectively. Because of the burst option, the corresponding effective exposure of XIS-0 is 6.61 ks and 1.39 ks for Obs A and Obs B, respectively.

Figure 4.6 shows the 0.5-10 keV XIS-0 and 15-30 keV PIN light curves and their hardness ratios for Obs A and Obs B. Plainly there are spectral changes within these two observations. In Obs A, there are a few short excursions to very low hardness

[4]https://heasarc.gsfc.nasa.gov/docs/suzaku/analysis/abc

ratios, but in Obs B this low hardness is sustained over an entire orbit (the fourth segment of Obs B, hereafter Obs B4). Due to the pile-up losses, we need at least an orbit of data to accumulate enough signal-to-noise for a good spectrum. Obs B4 has the lowest hardness ratio of any of the orbital segments in Obs A or Obs B.

To investigate the short-term (∼10 ks) variation during Obs A and Obs B, we split the data in four for Obs A and eight for Obs B as shown in Figure 4.6. Actually, Obs A have twenty-four orbital segments, however we made crude distinctions to understand the rough trend, and then, we split the data for each segment. We give details of the time selection in Table 4.1. Figure 4.7 shows the time averaged spectra of each of the segments from Obs A and B, unfolded with a single $\Gamma = 2$ power-law model. It is clear that the 5 – 60 keV flux during Obs B4 is the smallest. Figure 4.8 shows Obs B4 compared to a compilation of historically soft spectra seen from Cyg X-1, again unfolded assuming a single $\Gamma = 2$ power-law model. The previous softest spectra seen from Cyg X-1 by *Suzaku* was from 2010 (Yamada et al. 2013; Gou et al. 2014; Tomsick et al. 2014). Gou et al. (2014) claimed the softest Cyg X-1 spectra where there was both CCD and higher energy data and showed that the *Suzaku* 2010 data were the softest ever seen at that point. Since Obs B4 is significantly softer, this means it is the softest spectrum yet observed for which there are both CCD data to constrain the disk and higher energy data to constrain the tail. We searched data in Obs A and B which has a similar spectral shape to 2010 *Suzaku* data and similar exposure time to Obs B4 for following analysis sections, and found that the third orbital segments of Obs A2 (hereafter Obs A2iii) is ideal data for the strategy.

There are more pointed RXTE observations than CCD datasets. Grinberg et al. (2014) uniformly analyzed all the archival RXTE data, characterizing their spectra with a phenomenological model of a disk plus broken power law with exponential cutoff. We use their model and fit this to Obs B4 over their 3 – 100 keV energy range. This gives a low energy spectral index of $\Gamma_1 \sim 4.0$, steeper than their steepest index of $\Gamma_1 \sim 3.63$ (Grinberg et al. 2014). Thus Obs B4 is the softest spectrum yet detected from Cyg X-1.

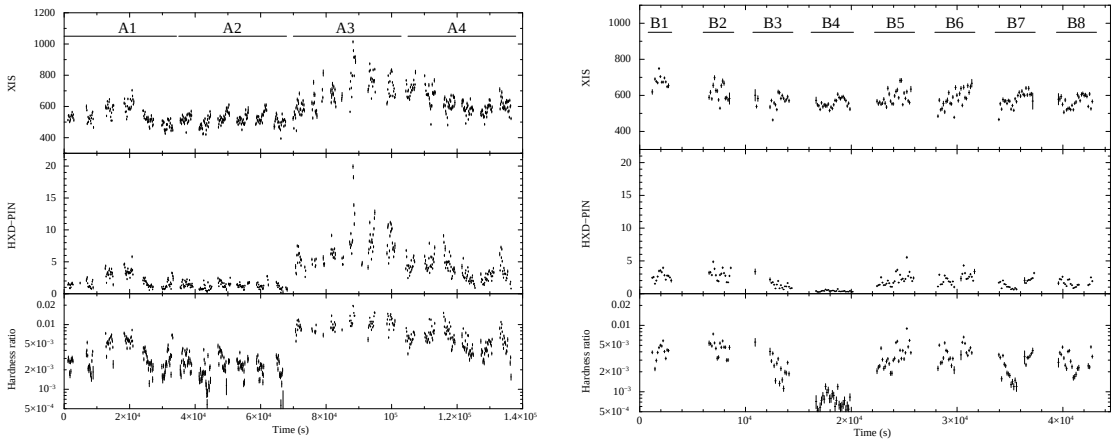

Figure 4.6: The light curves with bin of 128 sec observed by Suzaku during Obs A (Left), and that of Obs B (Right). Top: The light curve of the XIS0 in 0.5 – 10.0 keV. Middle: The light curve of the PIN in 15 –30 keV. Bottom: The hardness ratio between PIN (15 –30 keV) and XIS0 (0.5 – 10.0 keV). Obs B4 has the lowest 15-30 keV flux and the smallest hardness ratio.

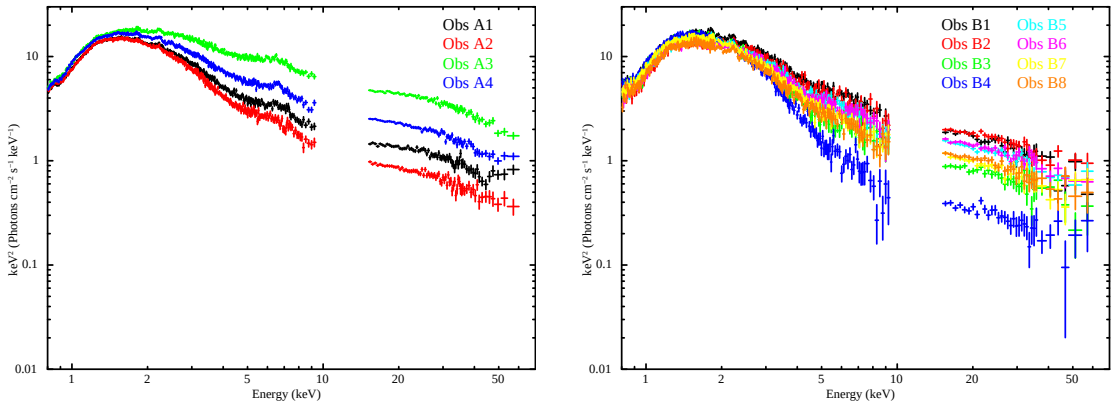

Figure 4.7: Left: The XIS0, PIN spectrum during Obs A1 (black), Obs A2 (red), Obs A3 (green), and Obs A4 (blue), removing the instrumental responses. Right: That of Obs B1 (black), Obs B2 (red), Obs B3 (green), and Obs B4 (blue), Obs B5 (light blue), Obs B6 (magenta), Obs B7 (yellow), and Obs B8 (orange).

Table 4.1: The Observations of Cyg X-1 with *Suzaku*

Observation	Obs ID	Obs start	Obs end	Exposure [ks] XIS0	Exposure [ks] PIN
Obs A	407015010	2013-04-08 02:17:18	2013-04-09 23:00:19	6.61	64.51
A1		2013-04-08 09:17:18	2013-04-08 18:12:12	1.97	15.36
A2		2013-04-08 18:50:44	2013-04-09 04:29:02	1.55	18.51
A3		2013-04-09 04:29:02	2013-04-09 13:04:58	1.36	11.11
A4		2013-04-09 13:57:40	2013-04-09 22:53:38	1.73	19.53
Obs B	407015020	2013-05-07 02:13:17	2013-05-07 14:34:19	1.39	20.51
B1		2013-05-07 02:17:33	2013-05-07 02:43:41	0.19	1.81
B2		2013-05-07 03:47:49	2013-05-07 05:04:13	0.11	2.10
B3		2013-05-07 05:04:13	2013-05-07 05:54:45	0.13	2.04
B4		2013-05-07 06:37:01	2013-05-07 07:30:23	0.22	3.45
B5		2013-05-07 08:12:35	2013-05-07 09:05:57	0.19	3.45
B6		2013-05-07 09:48:11	2013-05-07 11:27:33	0.18	2.97
B7		2013-05-07 11:27:33	2013-05-07 12:17:07	0.19	2.38
B8		2013-05-07 12:59:23	2013-05-07 13:52:39	0.19	2.31
2010	905006010	2010-12-17 00:10:26	2010-12-17 18:41:36	2.99	35.50

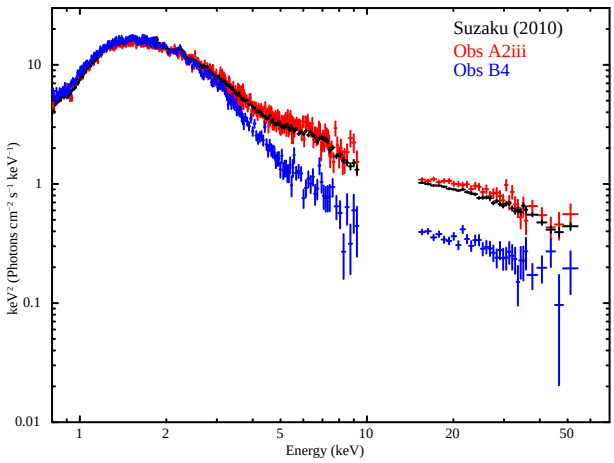

Figure 4.8: The softest previous broadband spectrum of Cyg X-1 (2010, used in Gou et al. (2014), black), has significantly stronger tail than Obs B4 (blue). We also include Obs A2iii (red), in order to show how similar it is to the 2010 *Suzaku* data.

Chapter 5

Data analysis

5.1 Spectral analysis of Cygnus X-1

We use XSPEC version 12.9.0n for all spectral fitting, and give 90% confidence errors on all parameters ($\Delta\chi^2 = 2.706$). We fix the system parameters of distance, black hole mass and disk inclination at $D = 1.86$ kpc, $M = 14.8\ M_\odot$, and $i = 27.1$ deg (Reid et al. 2011; Orosz et al. 2011). The solar abundance table is set to Wilms et al. (2000), and iron abundance is set to 1. We use data from 0.8-8 keV for XIS0, and 15-60 keV for the PIN, but we calculate all models over the range 0.1-1000 keV using the energies extend command as they include convolution components. Additionally, in the following analysis, we fixed the relative normalization CONST of the XIS and PIN at 1.15[1].

We show the results step by step, with detailed parameters for each model given in Table 5.1 – Table 5.5. We are assuming sixteen models with combinations of relativistic disk (KERBB) or non-relativistic disk (DISKBB), thermal component (NTHCOMP, BB, COMPTT), fully hybrid electrons (EQPAIR), and reflections of them as shown in Figure 5.1.

5.1.1 Disk with non-thermal Comptonisation

At first, we follow the model which is used in Gou et al. (2014), where the spectrum is assumed to consist of a relativistic disk (KERRBB: Li et al. 2005), with color temperature correction fixed to 1.7 (Shimura & Takahara 1995), which acts as the source of seed photons for non-thermal Comptonization (SIMPL: Steiner et al. 2009). The SIMPL model in its original form only calculates the sum of the disk and Comptonised photons, whereas only the Comptonised photons are reflected. We thus use the extension of this model, CSIMPL (Kolehmainen et al. 2014) as it allows the Compton tail to be separated from the unscattered disk photons by setting the up scattering switch to 2. We denote this as CSIMPL(2) (Compton scattering component), whereas CSIMPL(1) is the sum of the unscattered disk and Comptonised photons as in SIMPL. Gou et al. (2014) used the XILLVER tables of García et al. (2014) in order to describe the reflection from the disk. These have the most up-to-date treatment of atomic physics, but assume that the illuminating spectrum is a power law, i.e. that source of seed photons for Compton scattering is outside of the bandpass. This is not true in our data. Instead we use the XILCONV model which converts the XILLVER reflection table models into a convolution for use with any continuum (Kolehmainen et al. 2011), parameterized by the ionization parameter $\xi = L/(nR^2)$ of the illuminated disk. We then convolved this with the relativistic smearing model of RELCONV (Dauser et al. 2014) in order to model reflection from the disk. Gou et al. (2014) used TBABS (Wilms et al. 2000) for the absorption model, however we use TBNEW_GAS, which is an updated version[2]. The full model is then given by:

[1] http://www.astro.isas.jaxa.jp/suzaku/doc/suzakumemo/suzakumemo-2008-06.pdf
[2] http://pulsar.sternwarte.uni-erlangen.de/wilms/research/tbabs/

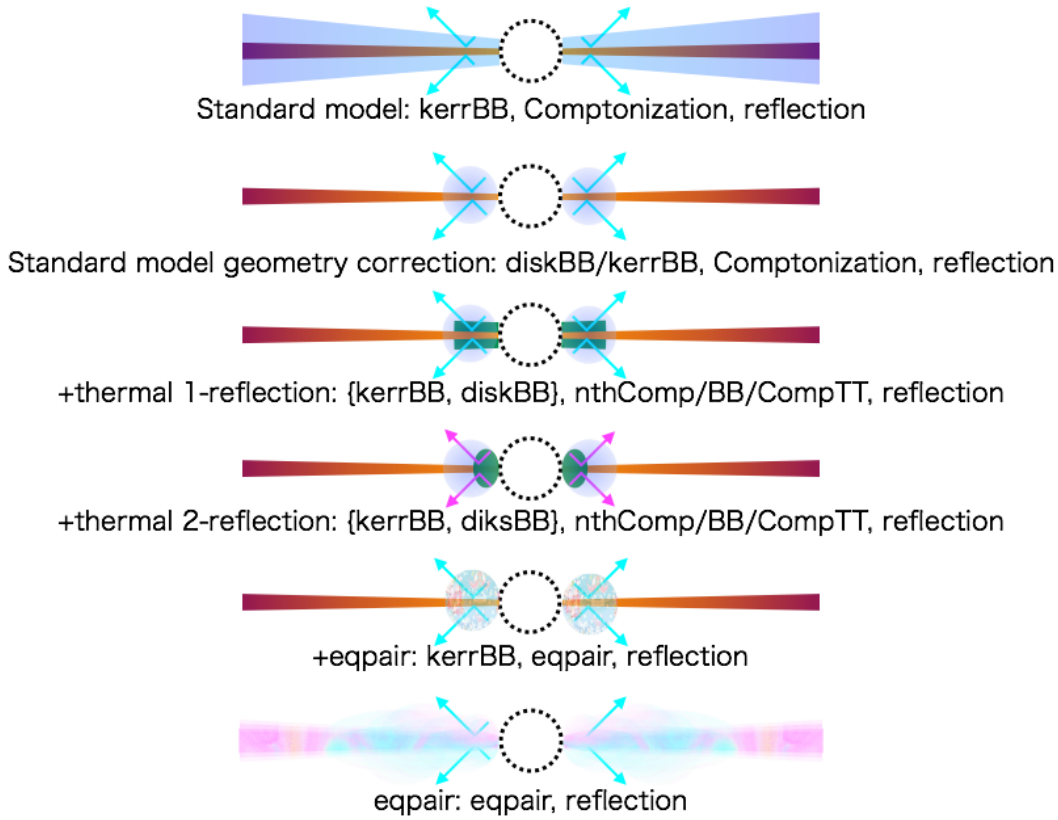

Figure 5.1: The schematic picture of the geometry, which we are assuming. Standard model: relativistic disk and Comptonization of disk photons. Standard model geometry correction: non-relativistic/relativistic disk and Comptonization of disk photons only from inner part of the disk. +thermal with 1-reflection model: relativistic/non-relativistic disk and thermal/non-thermal Comptonization and reflection of the non-thermal Comptonization. +thermal with 2-reflection model: relativistic/non-relativistic disk and thermal/non-thermal Comptonization and reflection of both of the Comptonization. +EQPAIR model: relativistic disk with fully hybrid electrons and their reflection. EQPAIR model: non-relativistic disk with fully hybrid electrons and their reflection.

Kerr disk and Comptonization of disk photons (Standard model)
CONST ∗ TBNEW_GAS(CSIMPL(1) ⊗ KERRBB + RELCONV ⊗ XILCONV(CSIMPL(2) ⊗ KERRBB))

We initially tried to determine the best fit parameters of the relativistic reflection from the data, but there are too many free parameters (potentially three for a broken power law emissivity in RELCONV, then another three which are the relative reflection normalization, iron abundance and ionization parameter in XILCONV) for the data quality. We follow Gou et al. (2014) and fix the radial illumination emissivity to a single power law of index of 2.5, fix the abundance to solar, set the reflector solid angle to unity, the inner radius of RELCONV is set to unity, i.e. tied to the spin dependent innermost stable circular orbit, and leaving only $log(\xi)$ as a single free parameter. We note that if we leave additional parameters free, their values cannot be constrained and the fit is not improved.

The fitting results are shown in Figure 5.2, with parameters given in Table 5.1. This model gives a high spin, $a_* \sim 0.95$, similar to the results of Gou et al. (2014) even though the scattered fraction is significantly lower than in their data. While the fit is adequate, the PIN residuals in Figure 5.2 have some discrepancies below 20 keV, showing that the data are not well described by the high energy tail used in this model. A flatter spectral index would give a better fit at these energies, but the steeper index is required in order to fit the lower energy emission. Allowing more parameters to be free does not improve the fit, and as described above the values for the extra parameters cannot be constrained. Instead, the discrepancies likely indicate that the data would be better fit by two different Comptonisation components (Gierliński et al. 1999; Zdziarski et al. 2002). Such a scenario is also more compatible with the observed time lags (Pottschmidt et al. 2000; Grinberg et al. 2014), and we therefore explore more complex Comptonisation models, where there are two components.

5.1.2 Standard model with geometry correction

Classically the geometry around a black hole is assumed as Figure 2.16, while the Comptonisation components of Standard model covers whole of the disk because it assumes the seed photon of the Comptonisation components is whole of the disk. It is not true for the assumption. Thus, we create a new model to correct the geometry that the seed photon is only inner part of the disk. To correct the geometry, we have 2-step followings.

For the first step, we note that a KERRBB dose not have an overt parameter the disk temperature, thus, we use a DISKBB of non-relativistic disk and estimate the temperature of the temperature of DISKBB and BBODYRAD. Here, the temperature of the BBODYRAD is linked to the temperature of the DISKBB. The scattering factor of CSIMPL is fixed as 1, means one hundred precent photon of the inner disk is scattered and turn to the Comptonization component.

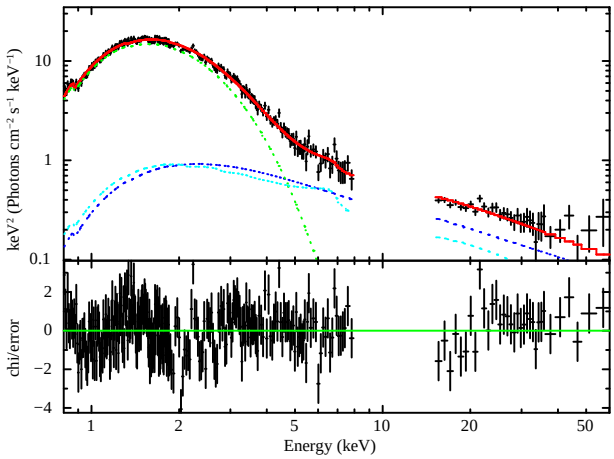

Figure 5.2: The fitting results of Obs B4. Assuming Standard disk model (disk and Comptonization of disk photons, corresponding to Gou et al. (2014)). Red: total, Green: KERRBB , Blue: Comptonization of KERRBB , Cyan: reflection of the Comptonization.

For the second step, after estimation of the temperature, we use KERBB rather than DISKBB, and the temperature of BBODYRAD is fixed to the temperature of DISKBB of the first step. The full model is then given by:

Schwarzschild/Kerr disk and Comptonization of disk photons with geometry correction (Standard model geo-cor)

(i) CONST $*$ TBNEW_GAS(DISKBB + BBODYRAD + CSIMPL(1) $\otimes$ BBODYRAD + RELCONV $\otimes$ XILCONV(CSIMPL(2) $\otimes$ BBODYRAD))
(ii) CONST $*$ TBNEW_GAS(KERRBB + BBODYRAD + CSIMPL(1) $\otimes$ BBODYRAD + RELCONV $\otimes$ XILCONV(CSIMPL(2) $\otimes$ BBODYRAD))

The fitting results of second step is shown in Figure 5.3 and Table 5.1. The ratio of the normalization between DISKBB and BBODYRAD is $\sim$3%, thus 3% photons of the inner part of the disk turn to the Comptonization component. The χ^2/d.o.f. is the same as the Standard model.

5.1.3 Complex Comptonisation: +thermal emission with 1-reflection model

Nonetheless, the Compton continuum could have an impact if it is complex. Even completely non-thermal acceleration processes, where the electrons are injected as a pure power law, do not result in a power law Comptonisation spectrum. Thus, this is motivated by physical models which derive the self consistent electron distribution from acceleration/heating balanced with cooling from both Coulomb collisions and

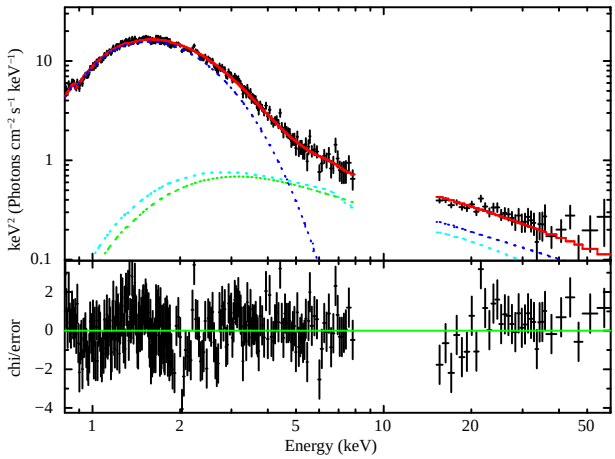

Figure 5.3: The fitting results of Obs B4. Standard model geo cor model (Schwarzschild/Kerr disk and Comptonization of disk photons with geometry correction). Red: total, Green: DISKBB , Blue: Comptonization of only inner part of KERRBB , Cyan: reflection of the Comptonization.

Comptonisation. Coulomb collisions act to thermalize the low energy electrons, so that the resulting steady state electron distribution is hybrid, being thermal at low energies but with a power law tail due to Compton cooling dominating at high energies (Coppi 1999; Zdziarski et al. 2001; Hjalmarsdotter et al. 2016).

+NTHCOMP with 1-reflection

The resulting Compton tail can be approximated as two Compton components, one thermal and one non-thermal (See e.g., Gierliński & Done 2003). We repeat that the fits of Gierliński et al. (1999) to the ASCA and RXTE soft state data from Cyg X-1 (which is only slightly harder than Obs A2iii and the Suzaku 2010 data) required this complex continuum model. We assume that the thermal comptonisation region is itself the seed photons for the non thermal corona, and the reflection of the additional component dose not effect for the spectrum because it is connected to the disk rather than the corona so the model is given by:

Kerr disk and thermal(NTHCOMP)/non-thermal Comptonization and reflection of the non-thermal Comptonization (KERRBB +NTHCOMP with 1-reflection)

CONST $*$ TBNEW_GAS(KERRBB + CSIMPL(1) $\otimes$ NTHCOMP + RELCONV $\otimes$ XILCONV(CSIMPL(2) $\otimes$ NTHCOMP))

This gives a significantly better fit to the data (See Table 5.1), and a significantly lower spin. The fitting result is shown in Figure 5.4 left. Here, we do not show the kT_e of NTHCOMP since it can not be well constrained. The emission which was previously fit as the highest temperature emission from the disk, driving the high

spin, is now fit instead as the Comptonization component. The emission which was previously fit as the highest temperature emission from the disk, driving the high spin, is now fit instead as the thermal Comptonization component. However, the parameters of this thermal Comptonization indicate that it has a steep spectral index and low electron temperature. As such, it seems to be a blackbody shape, and possibly connected to the disk than to the very rarified Compton tail.

Here, we fit the disk continuum with a very simple model in order to try to constrain the potential changes in structure and energetics from that of a standard disk. Our physical picture is of an inner disk which has a different color temperature correction to the remaining disk emission. The KERRBB disk model used above, where it is assumed that the disk extends down to the R_{isco} with a single color temperature correction, so it does not correctly describe this scenario. Instead, we use the DISKBB model for the outer disk, and a NTHCOMP for the inner disk to try to estimate radii and energetics. We replace KERRBB as DISKBB, so the model is given by:

Schwarzschild disk and thermal(NTHCOMP)/non-thermal Comptonization and reflection of the non-thermal Comptonization (DISKBB +NTHCOMP with 1-reflection)

CONST ∗ TBNEW_GAS(DISKBB + CSIMPL(1) ⊗ NTHCOMP + RELCONV ⊗ XILCONV(CSIMPL(2) ⊗ NTHCOMP))

The fitting results shows surpassingly the same parameters as the previous model event though the DISKBB dose not have the relativistic effects of the disk as shown in Table 5.1. Thus, it means we can not constrain spin parameter when it is not extremely high (∼0–0.8). It is a reasonable result considering the relativistic effects as shown in Figure 2.5. Hence we explore the behavior of the additional component such as the additional component is connected disk or not in following sections.

+BB model with 1-reflection

Here, we explore whether this could be simply an overheated region of the inner disk, one with a slightly higher color temperature correction than that assumed for the rest of the disk (1.7, fixed in KERRBB). We replace the thermal Comptonization with a blackbody:

Kerr disk and overheated inner disk (BB) plus non-thermal Comptonization and reflection of the non-thermal Comptonization (KERRBB +BB with 1-reflection)

CONST ∗ TBNEW_GAS(KERRBB + CSIMPL(1) ⊗ BBODYRAD + RELCONV ⊗ XILCONV(CSIMPL(2) ⊗ BBODYRAD))

This gives a very similar χ^2/d.o.f. with the previous model, and shows that this additional component is not noticeably different in shape to a blackbody. The fitting

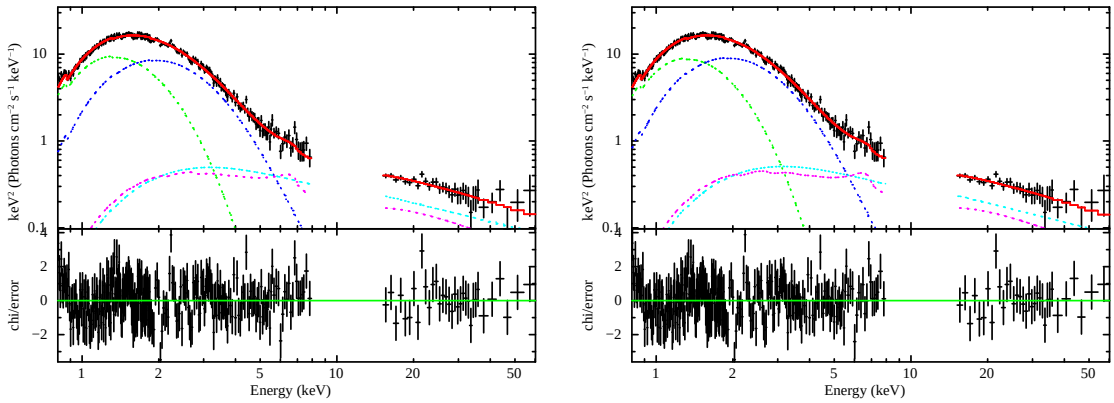

Figure 5.4: The fitting results of Obs B4. Left: KERRBB +NTHCOMP with 1-reflection model (Kerr disk and thermal(NTHCOMP)/non-thermal Comptonization and reflection of the non-thermal Comptonization). Right: DISKBB +NTHCOMP with 1-reflection model (Schwarzschild disk and thermal(NTHCOMP)/non-thermal Comptonization and reflection of the non-thermal Comptonization). Red: total, Green: KERRBB for left, DISKBB for right, Blue: NTHCOMP, Cyan: Comptonization of NTHCOMP, Magenta: reflection of the Comptonization.

result is shown in Figure 5.5 left. Again, this supports the idea that it is connected more to the disk itself than to the Comptonization region. The derived spin is significantly lower than that found from assuming a simple (single color temperature correction) disk and simple (power law electron distribution) Comptonization region.

Here, we replace KERRBB as DISKBB again, thus, it is a test to check the non-relativistic disk can explain the spectrum or not, so the model is given by:

Schwarzschild disk and overheated inner disk (BB) plus non-thermal Comptonization and reflection of the non-thermal Comptonization (DISKBB +BB with 1-reflection)

CONST $*$ TBNEW_GAS(DISKBB + CSIMPL(1) $\otimes$ BBODYRAD + RELCONV $\otimes$ XILCONV(CSIMPL(2) $\otimes$ BBODYRAD))

This gives the same parameters and χ^2/d.o.f. with the previous fit which used KERRBB as the disk component, and show that the additional hotter inner disk component has a more significant impact in broadening the disk continuum than relativistic smearing of the disk emission. The fitting results are shown in Figure 5.5 right. Again, this fit is significantly better than the Standard model which is using a simple disk continuum (See Table 5.1). We derived the apparent radius of the inner disk corresponding to the DISKBB normalization of 100^{+9}_{-24} km. We then assume that the hotter blackbody emission continue from the inner edged of DISKBB, which has area of $2\pi(R^2_{\text{in of DISKBB}} - R^2_{\text{in of BB}})$ with the luminosity from the blackbody normalization of 6.7×10^{36} ergs s^{-1}. The estimated the inner radius of the BB is $90.27^{+5.38}_{-0.46}$ km. While if we assume the shape of the BB is a sphere, then the radius

of BB is $30^{+0.68}_{-9.76}$ km as shown in Figure 5.6, and it shows that the BB dose not suit the relation of $T \propto R^{-3/4}$ with these assumptions. Thus, it means the additional (in this case, BB) is not part of the 'standard' disk.

Here, we calculate 'true' inner radius considering a color temperature correction. A color temperature correction factor of 1.7 (Shimura & Takahara 1995) as used in KERRBB gives a 'true' inner radius which is larger by a factor 1.7^2 (Kubota et al. 2001) i.e. 289 km which is $R_{\rm BB} \sim 13\ R_g$. Here, we define that $R_{\rm isco} = 6R_g = 6GM/c^2$ with $a_* = 0$.

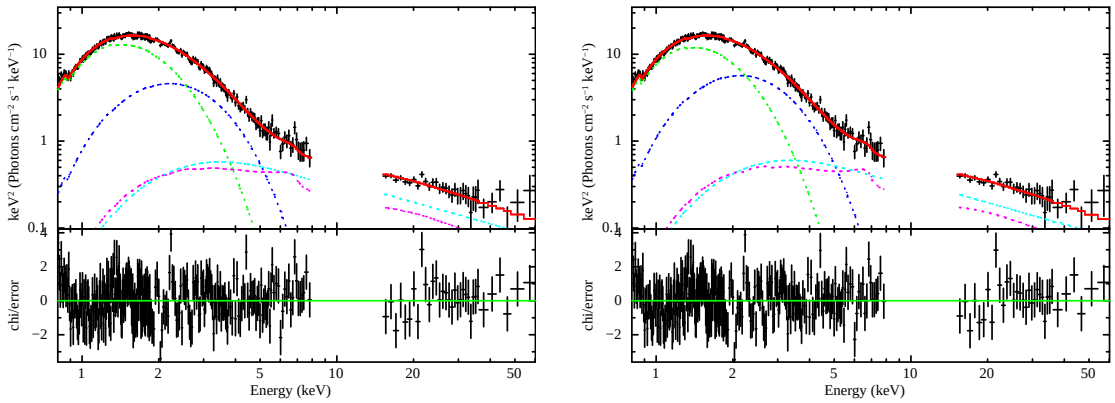

Figure 5.5: The fitting results of Obs B4. Left: KERRBB +BB with 1-reflection model (Kerr disk and overheated inner disk (BB) plus non-thermal Comptonization and reflection of the non-thermal Comptonization). Right: DISKBB +BB with 1-reflection model (Schwarzschild disk and overheated inner disk (BB) plus non-thermal Comptonization and reflection of the non-thermal Comptonization). Red: total, Green: KERRBB for left, DISKBB for right, Blue: BB, Cyan: Comptonization of BB, Magenta: reflection of the Comptonization.

COMPTT with 1-reflection model

We tried to use an additional thermal Comptonisation component of COMPTT to estimate the optical depth of the additional component. Here, we stress again that we reflect only non-thermal Comptonization because we assume the additional component is connected to the disk and the reflection dose not significantly effect for the spectrum

Kerr disk and thermal(COMPTT)/non-thermal Comptonization and reflection of both of the Comptonization (KERRBB +COMPTT with 1-reflection)

CONST ∗ TBNEW_GAS(KERRBB + CSIMPL(1) ⊗ COMPTT + RELCONV ⊗ XILCONV(CSIMPL(1) ⊗ COMPTT))

This gives a very similar χ^2/d.o.f. to the previous model, and a significantly lower spin (See Table 5.2). The fitting results are shown in Figure 5.7 left. Here,

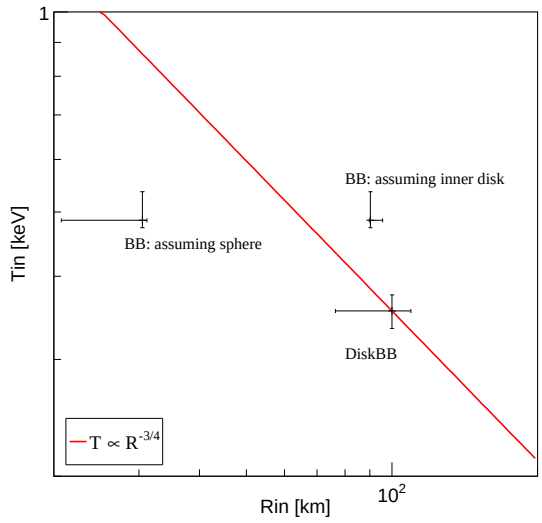

Figure 5.6: Relation between R_{in} and T_{in}, which is derived by normalization of DISKBB and BB. See detail in the text.

we replace KERRBB as DISKBB again, thus, it is a test to check the non-relativistic disk can explain the spectrum or not, so the model is given by:

Schwarzschild disk and thermal(COMPTT)/non-thermal Comptonization and reflection of both of the Comptonization (DISKBB +COMPTT with 1-reflection)

CONST $*$ TBNEW_GAS(DISKBB + CSIMPL(1) $\otimes$ COMPTT + RELCONV $\otimes$ XILCONV(CSIMPL(1) $\otimes$ COMPTT))

This gives a very similar parameters and χ^2/d.o.f. with the previous model as shown in Figure 5.7 right. Here, in both models, we can not determine whether the optical depth is large enough to be connected the disk because of the large ambiguity (still higher than 1). Thus, it may imply that the Comptonization component is perhaps also connected to the corona. We note again that the shape of the additional component is really close to a blackbody, thus, it should be connected to the disk if it is also connected to the corona. Therefore, we explore that the reflection of thermal Comptonization play important role or not in the following sections.

5.1.4 Complex Comptonisation: +thermal emission with 2-reflection model

We assume that the low temperature Comptonisation region is itself the seed photons for the non thermal corona (see below), and use COMPTT to describe the continuum shape from Comptonization of soft photons (Titarchuk 1994). We reflect both

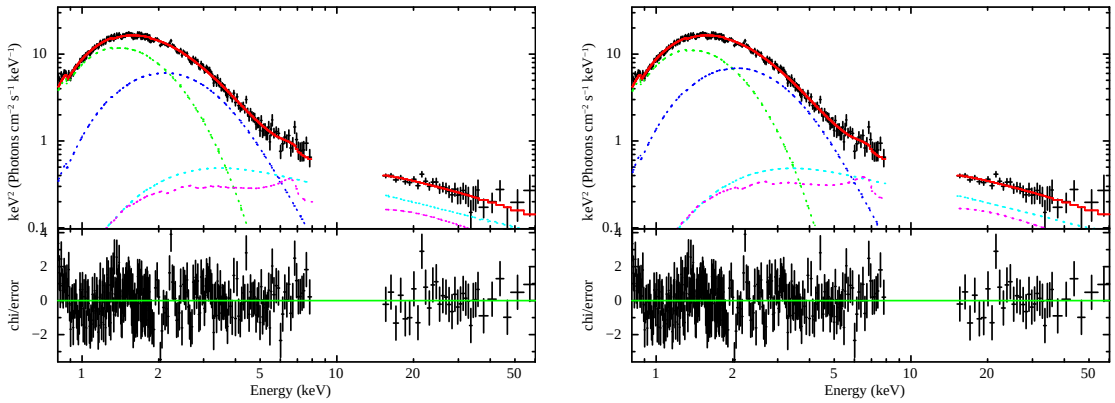

Figure 5.7: The fitting results of Obs B4. Left: KERRBB +COMPTT with 1-reflection model (Kerr disk and thermal(COMPTT)/non-thermal Comptonization and reflection of both of the Comptonization). Right: DISKBB +COMPTT with 1-reflection model (Schwarzschild disk and thermal(COMPTT)/non-thermal Comptonization and reflection of both of the Comptonization). Red: total, Green: KERRBB for left, DISKBB for right, Blue: COMPTT, Cyan: Comptonization of COMPTT, Magenta: reflection of the Comptonization.

Comptonisation components, as we are assuming that the thermal electrons can also illuminate the disk. We approximate the disk itself by KERRBB as before.

We note that KERRBB does not fully capture all the physics of our physical picture, where there is a disk which extends down close to (but not necessarily reaches) the last stable circular orbit of the black hole, and where the disk has a 'standard' color temperature correction only down to some radius, below which the color temperature correction is significantly higher, effectively giving rise to the low temperature, additional Comptonized emission. KERRBB instead assumes that the disk extends down to the last stable circular orbit, with fixed color temperature correction. The KERRBB models will then contain more high energy emission than a standard disk which truncates above the last stable circular orbit (leading to an underestimate of black hole spin). However, the gravitational energy released below this truncation should power the low temperature Comptonisation. Including this power in the KERRBB model would increase the inferred disk luminosity, leading to an overestimate of black hole spin. Since these two effects have opposite effects, and since there are no models available which combine inhomogeneous disk structure with fully general relativistic ray tracing (see Kubota & Done 2016, for an inhomogeneous disk structure with approximate relativistic effects), we simply note that deriving spin is complex and probably not very robust when the spectra are not dominated by a standard disk component.

Kerr disk and thermal(COMPTT)/non-thermal Comptonization and reflection of both of the Comptonization (KERRBB +COMPTT with 2-reflection)

CONST ∗ TBNEW_GAS(KERRBB + CSIMPL(1) ⊗ COMPTT + RELCONV ⊗ XILCONV(CSIMPL(1) ⊗ COMPTT))

This gives a slightly better χ^2/d.o.f. than the previous model, and a significantly lower spin (See Table 5.2). The fitting results are shown in Figure 5.8 left. Better χ^2/d.o.f. with a reflection of the thermal component means the reflection plays important role to explain the spectrum. Thus, in other words, the additional component imply that the vertical structure of the disk is different from the standard disk, and seems to be connected to the corona, too. Here, we repeat that the shape of the additional component is really close to the blackbody. Therefore, we can imagine that the additional component is merged between the disk and the corona. We note that this model slightly overestimates spin, as the thermal Comptonisation photons have not been removed from the disk continuum emission as is done in the SIMPL models (Steiner et al. 2009), so the disk should be slightly more luminous and hence have larger radius (Kubota et al. 2001).

Here, we replace KERRBB as DISKBB again, thus, it is a test to check the non-relativistic disk can explain the spectrum or not, so the model is given by:

Schwarzschild disk and thermal(COMPTT)/non-thermal Comptonization and reflection of both of the Comptonization (DISKBB +COMPTT with 2-reflection]

CONST ∗ TBNEW_GAS(DISKBB + CSIMPL(1) ⊗ COMPTT + RELCONV ⊗ XILCONV(CSIMPL(1) ⊗ COMPTT))

This gives a very similar parameters and χ^2/d.o.f. with the previous model as shown in Figure 5.8 right. It supports again that we can not constrain spin parameter when it is not extremely high (∼0–0.8).

+NTHCOMP with 2-reflection, and +BB with 2-reflection

Here, we utilize the model of NTHCOMP and BB again with the reflection both of thermal and non-thermal components, thus, just replace the COMPTT for the NTHCOMP or BB in the previous model to check the self consistency of the models. The main difference between COMPTT and NTHCOMP is the seed photon. The seed photons of NTHCOMP are assumed as a blacbody, while the seed photons of COMPTT are assumed as Wien distribution. Then, we assume that the additional component is connected to the disk, and extend to the corona, and the full model is described;

Kerr disk and thermal(NTHCOMP)/non-thermal Comptonization and reflection of both of the Comptonization (KERRBB +NTHCOMP with 2-reflection)

CONST ∗ TBNEW_GAS(KERRBB + CSIMPL(1) ⊗ NTHCOMP + RELCONV ⊗ XILCONV(CSIMPL(1) ⊗ NTHCOMP))

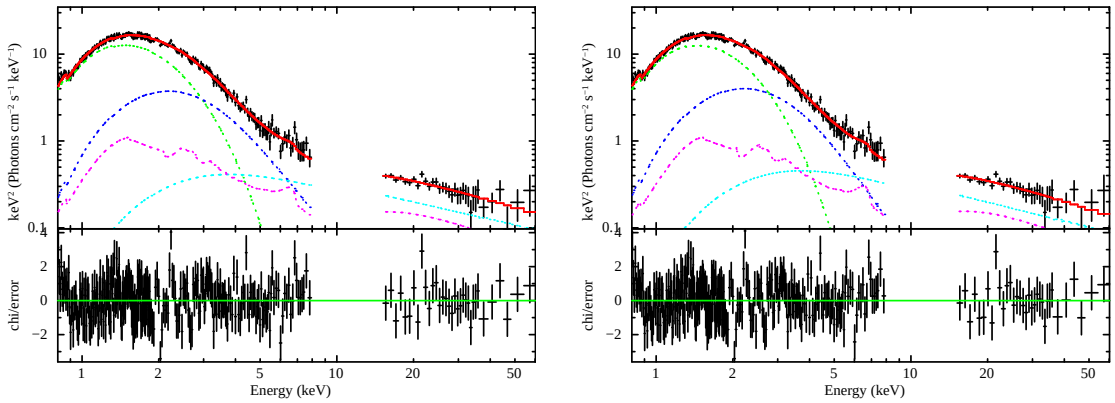

Figure 5.8: The fitting results of Obs B4. Left: KERRBB +COMPTT with 2-reflection model (Kerr disk and thermal(COMPTT)/non-thermal Comptonization and reflection of both of the Comptonization). Right: DISKBB +COMPTT with 2-reflection model (Schwarzschild disk and thermal(COMPTT)/non-thermal Comptonization and reflection of both of the Comptonization). Red: total, Green: KERRBB for left, DISKBB for right, Blue: COMPTT, Cyan: Comptonization of COMPTT, Magenta: reflection both of the COMPTT and Comptonization.

Schwarzschild disk and thermal(NTHCOMP)/non-thermal Comptonization and reflection of both of the Comptonization (DISKBB +NTHCOMP with 2-reflection)

CONST ∗ TBNEW_GAS(DISKBB + CSIMPL(1) ⊗ NTHCOMP + RELCONV ⊗ XILCONV(CSIMPL(1) ⊗ NTHCOMP))

Kerr disk and overheated inner disk (BB) plus non-thermal Comptonization and reflection both of the BB and non-thermal Comptonization (KERRBB +BB with 2-reflection)

CONST ∗ TBNEW_GAS(KERRBB + CSIMPL(1) ⊗ BB + RELCONV ⊗ XILCONV(CSIMPL(1) ⊗ BB))

Schwarzschild disk and overheated inner disk (BB) plus non-thermal Comptonization and reflection both of the BB and non-thermal Comptonization (DISKBB +BB with 2-reflection)

CONST ∗ TBNEW_GAS(DISKBB + CSIMPL(1) ⊗ BB + RELCONV ⊗ XILCONV(CSIMPL(1) ⊗ BB))

These models with 2-reflection give better χ^2/d.o.f. than the models with 1-reflection even when it is assuming BB. Thus, it is very interesting to note because usually the reflection of blackbody components can not effect for the spectrum since it has very high optical depth. The results support that the the additional component is merged between the disk and the corona. Also it supports again that we can not constrain spin parameter when it is not extremely high (∼0–0.8). The fitting results are shown in Figure 5.9 and Table 5.3.

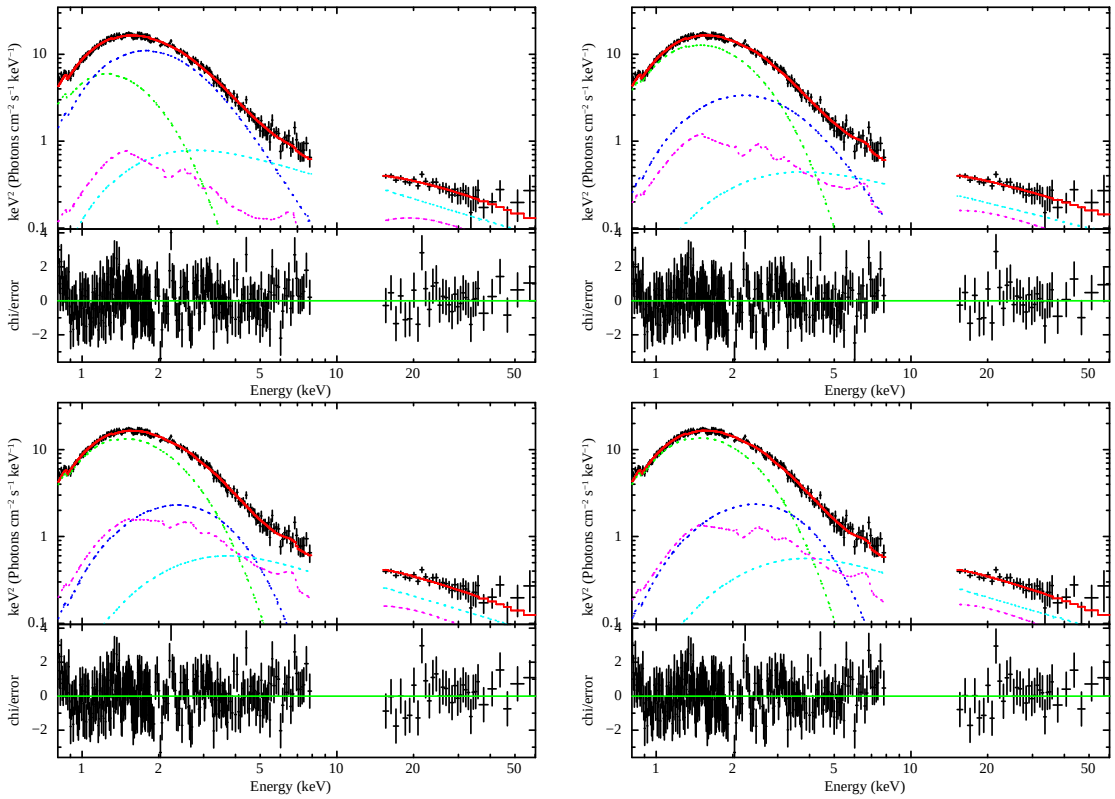

Figure 5.9: The fitting results of Obs B4. Top left: KERRBB +NTHCOMP with 2-reflection model (Kerr disk and thermal(NTHCOMP)/non-thermal Comptonization and reflection of both of the Comptonization). Top right: DISKBB +NTHCOMP with 2-reflection model (Schwarzschild disk and thermal(NTHCOMP)/non-thermal Comptonization and reflection of both of the Comptonization). Bottom left: KERRBB +BB with 2-reflection model (Kerr disk and overheated inner disk (BB) plus non-thermal Comptonization and reflection both of the BB and non-thermal Comptonization). Bottom right: DISKBB +BB with 2-reflection model (Schwarzschild disk and overheated inner disk (BB) plus non-thermal Comptonization and reflection both of the BB and non-thermal Comptonization). Red: total, Green: KERRBB for left, DISKBB for right, Blue: BB, Cyan: Comptonization of BB, Magenta: reflection of the Comptonization.

5.1.5 Complex Comptonisation: +EQPAIR model

In previous models, we confirmed that the additional component is connected to both of the disk and the corona. Thus we use a full model for the additional component, EQPAIR[3], which is wildly used for black hole binaries and AGNi (e.g., Zdziarski et al. 1996, 1998). we assume the additional component as completely non-thermal acceleration, described by a single power law injected electron distribution with index $\Gamma_{\rm inj}$. We allow this index to be free, and fix the lower and upper limits of the electron Lorentz factors to the default values of 1.3 and 1000, respectively. Coulomb cooling depends on the density of electrons in the region which is proportional to the optical depth, $\tau_{\rm p}$, divided by the size scale. We fix the size scale to the default of $R = 10^7$ cm (around $10R_{\rm g}$, see Gierliński et al. 1999), but have $\tau_{\rm p}$ be a free parameter. Compton cooling depends on the density of seed photons, so is $\propto L_{\rm bb}$ divided by the size scale, which is parameterized via the soft seed photon compactness, $\ell_{\rm bb} \propto L_{\rm bb}/R = 10$ (fixed, see Gierliński et al. 1999). The seed photon distribution in `eqpair` can be either a blackbody, or a simple Schwarzschild black hole model (`diskpn`: Gierliński et al. 1999). We do not use the `diskpn` option, and use a usual blackbody for the model.

The full model is:

Kerr disk plus fully hybrid electrons and their reflection (KERRBB +EQPAIR)

CONST $*$ TBNEW_GAS(KERRBB + CSIMPL(1) $\otimes$ EQPAIR + RELCONV $\otimes$ XILCONV(CSIMPL(1) $\otimes$ EQPAIR))

This gives the same χ^2/d.o.f. with previous models above, and also shows significantly lower spin. Thus, we also can see that the additional component is compose the thermal and non-thermal Comptonization. The fitting result are shown in Figure 5.10, and parameters are listed in Table 5.3.

5.1.6 Non-relativistic disk with fully hybrid electrons: EQPAIR

We finally fit with a full model for hybrid electrons, EQPAIR for whole the disk and the additional component. The fitting results are shown in Figure 5.11 right. However, `eqpair` includes seed photons only from a simple blackbody, or from a disk with an approximation to relativistic emissivity from a Schwarzchild black hole, `diskpn` (Gierliński et al. 1999). We use the `diskpn` option, and assume completely non-thermal acceleration, described by a single power law injected electron distribution with index $\Gamma_{\rm inj}$. We allow this index to be free, and fix the lower and upper limits of the electron Lorentz factors to the default values of 1.3 and 1000, respectively. We

[3]http://www.astro.yale.edu/coppi/eqpair/eqpap4.ps

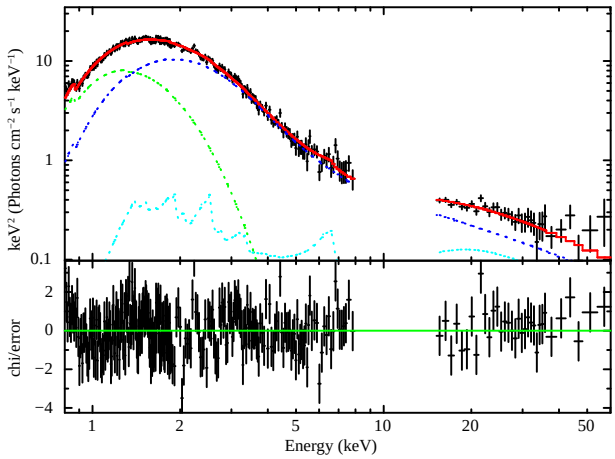

Figure 5.10: The fitting results of Obs B4 with KERRBB +EQPAIR model (Kerr disk plus fully hybrid electrons and their reflection). Red: total, Green: KERRBB, Blue: EQPAIR, Cyan: relection of EQPAIR.

fix the soft seed photon compactness, $\ell_{\rm bb} \propto L/R = 10$, and fix the size scale to the default of $R = 10^7$ cm (See Gierliński et al. 1999).

Schwarzschild disk with fully hybrid electrons and their reflection (EQPAIR)

CONST $*$ TBNEW_GAS(EQPAIR + RELCONV $\otimes$ XILCONV $\otimes$ EQPAIR)

The EQPAIR model returns both the Comptonisation resulting from the hybrid electron distribution and the unComptonised seed photons. However, our fits have a fairly high optical depth, so only a fraction $\exp(-\tau_{\rm p})$ of these unComptonised seed photons escape. Thus the spectrum is mainly the Comptonisation alone, so we reflect the entire EQPAIR continuum to get a good approximation to the reflection from the Comptonisation components. This gives a slightly worse χ^2/d.o.f. value than the +thermal model above, but is more constrained (has three fewer free parameters) so this is not significant. The inferred intrinsic `diskpn` component has a very similar spectral shape to the KERRBB component in these +thermal models, and the complex EQPAIR Comptonisation is very similar in the shape to the sum of the separate thermal and non-thermal Comptonisation components in these +thermal models. However, while this shows that a single zone model can reproduce most of the complex curvature, we again stress that a single-zone model can not explain the time lag behavior (Pottschmidt et al. 2000; Grinberg et al. 2014).

5.1.7 Degenerate solution of Comptonization components

In this subsection, we show a second solution of Comptonization. The blackbody has only one shape, while soft Comptonization components of NTHCOMP and COMPTT

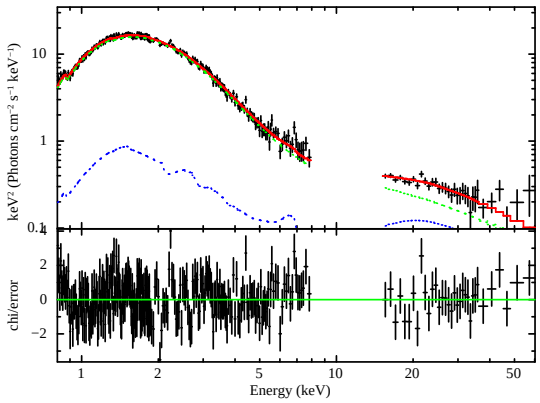

Figure 5.11: The fitting results of Obs B4 with EQPAIR model. Red: total, Green: EQPAIR, Blue: reflection of EQPAIR.

can have more than one solution depending on a temperature of the Comptonization component. In previous sections, physically, we think that the additional component should be connected to the inner disk, thus it should have higher temperature than the disk. However, we also found degenerate solution of Comptonization with lower temperature than the disk for any +thermal model. We show the example of lower temperature Comptonization solution of KERRBB +COMPTT with 2-reflection model, and DISKBB +COMPTT with 2-reflection model as shown in Figure 5.12 and Table 5.4. In the solution, the shape of COMPTT is away from blackbody and covering whole of the thermal emission, and the temperature is lower than the disk. Comparing with the Figure 5.8, the shape of each component is definitely different with each other. Utilizing the model of KERRBB +COMPTT with 2-reflection model with low temperature COMPTT solution, black hole spin is extremely high, while the model of DISKBB +COMPTT with 2-reflection model with low temperature COMPTT solution shows the same parameters excluding spin. We estimated the 'true' inner most radius of ∼120 km with the normalization of the DISKBB. It is ∼5.4 R_g and close to the innermost stable circular orbit of Schwarzschild black hole, thus it is almost consistent with a_*∼0. Thus, the results suggest if we believe the solution, we can not constrain black hole spin at all. In other wards, if the component is away from black body, then we cannot have the same confidence level to derive spin as we have estimated. Additionally, the optical depth of the component is fairy high, while the disk component is not significantly effected by the scattering. Therefore, it means the shape of the component is a "blob" rather than a corona. Furthermore, the χ^2/d.o.f. is $\ll 1$. It is somewhat strange in physical sense.

However, we can reject the solution with time analysis results of the fast time lags in these data (Pottschmidt et al. 2000; Grinberg et al. 2014), and results of this works. See detail following sections.

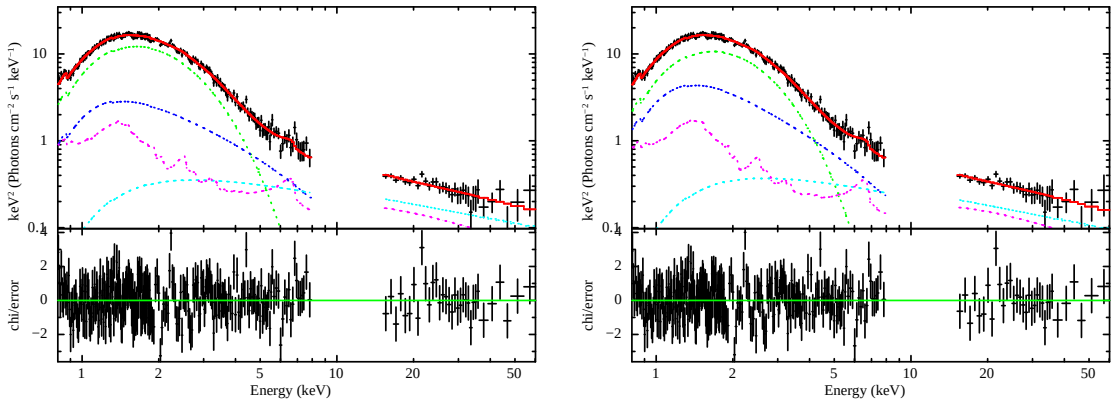

Figure 5.12: The fitting results of Obs B4. Left: KERRBB +COMPTT 2-reflection model with low temperature COMPTT solution (Kerr disk and thermal(COMPTT)/non-thermal Comptonization and reflection of both of the Comptonization). Right: DISKBB +COMPTT 2-reflection model with low temperature COMPTT solution (Schwarzschild disk and thermal(COMPTT)/non-thermal Comptonization and reflection of both of the Comptonization). Red: total, Green: KERRBB for left, DISKBB for right, Blue: COMPTT, Cyan: Comptonization of COMPTT, Magenta: reflection both of the COMPTT and Comptonization.

Table 5.1: Results of fitting the spectra with softest data sets of Obs B4 (i)

Component	Parameter	Standard	Standard model geo-cor	KERRBB +NTHCOMP1-ref	DISKBB +NTHCOMP 1-ref	KERRBB +BB 1-ref	DISKBB +BB 1-ref
TBNEW_GAS	N_H [10^{22} cm^{-2}]	$0.65^{+0.03}_{-0.02}$	$0.65^{+0.02}_{-0.01}$	$0.75^{+0.04}_{-0.03}$	$0.74^{+0.04}_{-0.04}$	$0.74^{+0.03}_{-0.03}$	$0.72^{+0.02}_{-0.02}$
CSIMPL	Γ	$2.93^{+0.11}_{-0.05}$	$2.91^{+0.06}_{-0.06}$	$2.72^{+0.13}_{-0.11}$	$2.73^{+0.14}_{-0.07}$	$2.82^{+0.09}_{-0.09}$	$2.84^{+0.07}_{-0.08}$
	FracSctr	$0.028^{+0.009}_{-0.003}$	1 (fixed)	$0.04^{+0.04}_{-0.01}$	$0.033^{+0.015}_{-0.008}$	$0.80^{+0.04}_{-0.02}$	$0.07^{+0.01}_{-0.01}$
KERRBB	a_*	$0.95^{+0.01}_{-0.01}$	$0.94^{0.01}_{-0.01}$	<0.65	—	$0.60^{+0.26}_{-0.39}$	—
	Mdd [g s^{-1}]	$0.18^{+0.01}_{-0.01}$	$0.20^{0.01}_{-0.01}$	$0.41^{+0.13}_{-0.13}$	—	$0.35^{+0.10}_{-0.06}$	—
DISKBB	T_{in} [keV]	—	—	—	$0.31^{+0.06}_{-0.06}$	—	$0.35^{+0.02}_{-0.02}$
	norm	—	—	—	$4.05^{+3.45}_{-1.26} \times 10^5$	–	$2.56^{+0.51}_{-1.07} \times 10^5$
NTHCOMP	Γ	—	–	$7.63^{+1.21}_{-1.22}$	$7.75^{+3.55}_{-1.63}$	—	—
	kT_{bb} [keV]	—	–	$0.39^{+0.13}_{-0.04}$	$0.39^{+0.07}_{-0.04}$	—	—
	norm	—	–	$8.29^{+4.04}_{-4.92}$	$8.89^{+0.51}_{-0.58}$	—	—
BBODYRAD	kT [keV]	—	0.469 (fixed)	—	—	$0.50^{+0.06}_{-0.05}$	$0.49^{+0.05}_{-0.01}$
	norm	—	$2.54^{+0.30}_{-0.21} \times 10^3$	—	—	$1.87^{+2.04}_{-0.48}$	$2.70^{+0.12}_{-1.45} \times 10^4$
XILCONV	log(ξ)	>3.79	$4.26^{+0.31}_{-0.45}$	$3.69^{+0.49}_{-0.83}$	$3.68^{+0.51}_{-0.60}$	$3.69^{+0.34}_{-0.56}$	$3.70^{+0.67}_{-0.29}$
	χ^2/d.o.f.	364.57/288	364.10/288	329.81/284	329.41/284	332.69/286	331.37/286
High frequency components/Total		12%	10%	4%	4%	4%	4%

Standard disk model: Kerr disk and Comptonization of disk photons
Standard model geo-cor model: Schwarzschild disk and Comptonization of disk photons with geometry correction
KERRBB +NTHCOMP1-ref model: Kerr disk and thermal(NTHCOMP)/non-thermal Comptonization and reflection of the non-thermal Comptonization
DISKBB +NTHCOMP 1-ref model: Schwarzschild disk and thermal(NTHCOMP)/non-thermal Comptonization and reflection of the non-thermal Comptonization
KERRBB +BB 1-ref model: Kerr disk and overheated inner disk (BB) plus non-thermal Comptonization and reflection of the non-thermal Comptonization
DISKBB +BB 1-ref model: Schwarzschild disk and overheated inner disk (BB) plus non-thermal Comptonization and reflection of the non-thermal Comptonization
See APPENDIX for parameter definitions.

Table 5.2: Results of fitting the spectra with softest data sets of Obs B4 (ii)

Component	Parameter	KERRBB +COMPTT 1-ref	DISKBB +COMPTT 1-ref	KERRBB +COMPTT 2-ref	DISKBB +COMPTT 2-ref
TBNEW_GAS	N_H [10^{22} cm^{-2}]	$0.74^{+0.05}_{-0.04}$	$0.72^{+0.03}_{-0.02}$	$0.68^{+0.01}_{-0.03}$	$0.66^{+0.06}_{-0.01}$
CSIMPL	Γ	$2.73^{+0.12}_{-0.16}$	$2.72^{+0.12}_{-0.20}$	$2.67^{+0.18}_{-0.16}$	$2.73^{+0.16}_{-0.16}$
	FracSctr	$0.051^{+0.040}_{-0.024}$	$0.05^{+0.02}_{-0.01}$	$0.07^{+0.06}_{-0.02}$	$0.07^{+0.06}_{-0.02}$
KERRBB	a_*	<0.87	—	$0.80^{+0.08}_{-0.30}$	—
	Mdd [g s^{-1}]	$0.38^{+0.30}_{-0.11}$	—	$0.24^{+0.06}_{-0.03}$	—
DISKBB	T_{in} [keV]	—	$0.34^{+0.05}_{-0.06}$	—	$0.39^{+0.03}_{-0.09}$
	norm	—	$3.02^{+1.81}_{-1.27} \times 10^5$	—	$1.50^{+1.02}_{-0.61} \times 10^5$
COMPTT	T_0 [keV]	$0.44^{+0.11}_{-0.06}$	$0.43^{+0.43}_{-0.08}$	$0.44^{+0.16}_{-0.04}$	$0.46^{+0.21}_{-0.08}$
	kT [keV]	<11.17	<72.01	$3.52^{+28.73}_{-1.65}$	$3.64^{+45.32}_{-0.66}$
	taup	$1.40^{+41.48}_{-1.08}$	$1.43^{+62.80}_{-0.88}$	$1.66^{+10.99}_{-0.62}$	$1.06^{+17.97}_{-0.83}$
	norm	<10.05	$4.68^{+167.48}_{-0.42}$	$1.37^{+1.63}_{-0.87}$	$1.41^{+5.35}_{-0.99}$
NTHCOMP	Γ	—	—	—	—
	kT_{bb} [keV]	—	—	—	—
	norm	—	—	—	—
BBODYRAD	kT [keV]	—	—	—	—
	norm	—	—	—	—
XILCONV	log(ξ)	$3.31^{+0.87}_{-0.53}$	$3.35^{+0.78}_{-0.50}$	$4.00^{+0.27}_{-0.63}$	$4.00^{+0.17}_{-0.65}$
	χ^2/d.o.f.	329.58/284	329.12/284	320.63/284	321.00/284
High frequency components/Total		3%	3%	4%	4%

KERRBB +COMPTT 1-ref model: Kerr disk and thermal(COMPTT)/non-thermal Comptonization and reflection of both of the Comptonization
DISKBB +COMPTT 1-ref model: Schwarzschild disk and thermal(COMPTT)/non-thermal Comptonization and reflection of both of the Comptonization
KERRBB +COMPTT 2-ref model: Kerr disk and thermal(COMPTT)/non-thermal Comptonization and reflection of both of the Comptonization
DISKBB +COMPTT 2-ref model: Schwarzschild disk and thermal(COMPTT)/non-thermal Comptonization and reflection of both of the Comptonization
See APPENDIX for parameter definitions.

Table 5.3: Results of fitting the spectra with softest data sets of Obs B4 (iii)

Component	Parameter	KERRBB +NTHCOMP 2-ref	DISKBB +NTHCOMP 2-ref	KERRBB +BB 2-ref	DISKBB +BB 2-ref	KERRBB +EQPAIR	EQPAIR
TBNEW_GAS	N_H [10^{22} cm^{-2}]	$0.70^{+0.02}_{-0.03}$	$0.64^{+0.02}_{-0.01}$	$0.70^{+0.02}_{-0.01}$	$0.66^{+0.02}_{-0.02}$	$0.69^{+0.01}_{-0.02}$	$0.69^{+0.02}_{-0.02}$
CSIMPL	Γ	$2.90^{+0.09}_{-0.19}$	$2.73^{+0.15}_{-0.08}$	$2.86^{+0.10}_{-0.13}$	$2.86^{+0.09}_{-0.11}$	—	
	FracSctr	$0.04^{+0.02}_{-0.02}$	$0.079^{+0.033}_{-0.024}$	$0.16^{+0.04}_{-0.03}$	$0.15^{+0.02}_{-0.02}$	—	
KERRBB	a_*	<0.52	—	$0.80^{+0.05}_{-0.11}$	—	<0.88	
	Mdd [g s^{-1}]	$0.31^{+0.12}_{-0.11}$	—	$0.26^{+0.04}_{-0.03}$	—	$0.25^{+0.06}_{-0.02}$	
DISKBB	T_{in} [keV]	—	$0.41^{+0.09}_{-0.04}$	—	$0.41^{+0.01}_{-0.02}$	—	
	norm	—	$1.23^{+0.35}_{-0.34} \times 10^5$	—	$1.32^{+0.30}_{-0.12}$	—	
NTHCOMP	Γ	$6.31^{+0.23}_{-2.39}$	$6.11^{+1.22}_{-1.28}$	—	—	—	
	kT_{bb} [keV]	$0.34^{+0.03}_{-0.02}$	$0.46^{+0.03}_{-0.03}$	—	—	—	
	norm	$13.2^{+7.92}_{-7.40}$	$2.34^{+3.38}_{-0.64}$	—	—	—	
BBODYRAD	kT [keV]	—	—	$0.55^{+0.06}_{-0.04}$	$0.58^{+0.03}_{-0.05}$	—	
	norm	—	—	$6.78^{+5.13}_{-3.43} \times 10^3$	$5.67^{+2.61}_{-1.40} \times 10^3$	—	
XILCONV	$\log(\xi)$	$3.97^{+0.35}_{-0.73}$	$3.67^{+0.77}_{-0.49}$	$4.31^{+0.30}_{-0.37}$	$4.07^{+0.33}_{-0.34}$	$4.00^{+0.23}_{-0.62}$	$4.18^{+0.28}_{-0.47}$
EQPAIR	l_h/l_s	—	—	—	—	$0.16^{+0.03}_{-0.03}$	$0.11^{+0.02}_{-0.01}$
	kT_{bb} [keV]	—	—	—	—	$0.50^{+0.06}_{-0.06}$	$0.39^{+0.02}_{-0.01}$
	tau_p	—	—	—	—	$0.35^{+0.21}_{-0.14}$	$1.51^{+1.48}_{-0.50}$
	Γ_{inj}	—	—	—	—	$4.10^{+0.26}_{-0.49}$	$5.00^{+0.00\dagger}_{0.31}$
	norm	—	—	—	—	$1.98^{+3.42}_{-0.99} \times 10^{-9}$	$2.76^{+0.51}_{-0.45}$
	χ^2/d.o.f.	323.01/284	321.21/284	329.50/286	327.80/286	318.16/285	328.88/287
High frequency components/Total		7%	3%	4%	3%	—	—

KERRBB +NTHCOMP 2-ref model: Kerr disk and thermal(NTHCOMP)/non-thermal Comptonization and reflection of both of the Comptonization
DISKBB +NTHCOMP 2-ref model: Schwarzschild disk and thermal(NTHCOMP)/non-thermal Comptonization and reflection of both of the Comptonization
KERRBB +BB 2-ref model: Kerr disk and overheated inner disk (BB) plus non-thermal Comptonization and reflection both of the BB and non-thermal Comptonization
DISKBB +BB 2-ref model: Schwarzschild disk and overheated inner disk (BB) plus non-thermal Comptonization and reflection both of the BB and non-thermal Comptonization
KERRBB +EQPAIR model: Kerr disk plus fully hybrid electrons and their reflection
EQPAIR model: Schwarzschild disk with fully hybrid electrons and their reflection
†the upper limit of Γ_{inj} is pegged to 5.0.
See APPENDIX for parameter definitions.

Table 5.4: Results of fitting the spectra with softest data sets of Obs B4 (vi)

Component	Parameter	KERRBB +COMPTT 2-ref with low temperature COMPTT solution	DISKBB +COMPTT 2-ref with low temperature COMPTT solution
TBNEW_GAS	N_H [10^{22} cm^{-2}]	$0.75^{+0.15}_{-0.06}$	$0.71^{+0.01}_{-0.07}$
CSIMPL	Γ	$2.54^{+0.17}_{-0.19}$	$2.58^{+0.19}_{-0.21}$
	FracSctr	$0.04^{+0.03}_{-0.02}$	$0.03^{+0.03}_{-0.02}$
KERRBB	a_*	>0.97	—
	Mdd [g s^{-1}]	$0.12^{+0.02}_{-0.02}$	—
DISKBB	T_{in} [keV]	—	$0.49^{+0.02}_{-0.01}$
	norm	—	$4.37^{+1.01}_{-1.24} \times 10^4$
COMPTT	T_0 [keV]	$0.17^{+0.06}_{-0.03}$	$0.19^{+0.05}_{-0.03}$
	kT [keV]	$2.29^{+1.56}_{-1.02}$	<10.32
	taup	$3.14^{+1.60}_{-1.69}$	$2.78^{+1.99}_{-0.86}$
	norm	$8.02^{+20.23}_{-4.23}$	$8.97^{+10.80}_{-5.02}$
XILCONV	log(ξ)	$3.38^{+0.34}_{-0.25}$	$3.44^{+0.51}_{-0.33}$
	χ^2/d.o.f.	303.56/284	303.46/284
High frequency components/Total		3–8%	4–9%

KERRBB +COMPTT 2-ref model with low temperature COMPTT solution: Kerr disk and thermal(COMPTT)/non-thermal Comptonization and reflection of both of the Comptonization
DISKBB +COMPTT 2-ref model with low temperature COMPTT solution: Schwarzschild disk and thermal(COMPTT)/non-thermal Comptonization and reflection of both of the Comptonization
See APPENDIX for parameter definitions.

5.2 Timing analysis of Cygnus X-1

In this section, we focus on the time analysis of Obs B4 to constrain the models with the new method of timing analysis. As seen in previous sections, the spectrum of the lower energy band is dominated by the disk emission, while higher energy band is dominated by Comptonized emission. Thus, we set two energy band of 1.5–2.0 keV for lower energy band, and 6.0–10.0 keV band for high energy band, respectively. The time scale of variability is different in these energy band. Typical time scale of the disk (lower energy band) is ∼1–10 sec, and the corona (Comptonized emission, higher energy band) is ∼0.1 sec (e.g., Done et al. 2007; Grinberg et al. 2014).

As seen in Figure 4.3, XIS3 data with the P-sum mode observation has a color modulation in RAWY axis. It would suggest that the data has a telemetry saturation even tough we conducted a data reduction to remove the telemetry saturation. The telemetry saturation may cause some troubles for the study of timing analysis, thus at first, we study the effect. To study the effect, we split the data of Obs B in sixteen in RAWY axis as shown in Figure 5.13. The one segment is corresponding to 64 ch in the RAWY axis. It seems that 0 -703 ch are brighter than 704–1023 ch, and it means lower channels in RAWY have more data than that of higher channels, in other words, telemetry seems to be saturated and data seem not to be stored in higher channels.

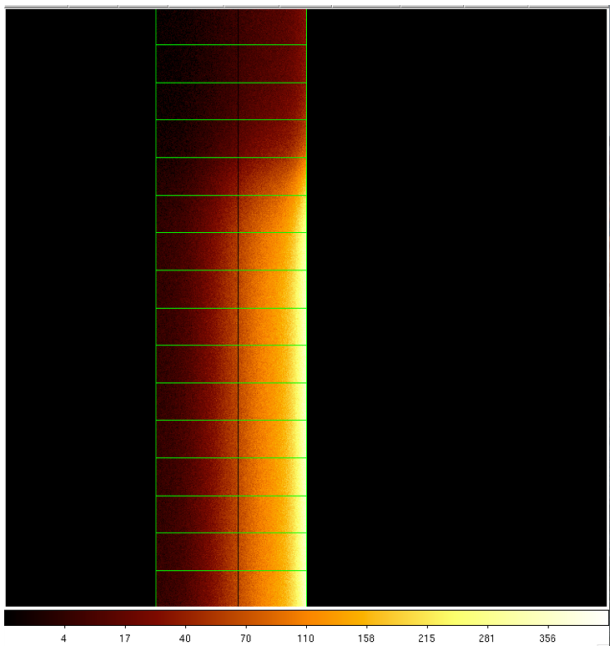

Figure 5.13: Obs B data of XIS3 with P-sum mode observation in ActX–RawY space (See §3.4 for a coordinate of XIS). The data are split in sixteen in RAWY axis.

To confirm the telemetry saturation, we made histograms of counts in RAWY

for Obs B1–B8 as shown in Figure 5.14. In Figure 5.14 left, the horizontal axis is corresponding to the channel in RAWY, and in the right panel, the horizontal axis is corresponding to the channels larger than RAWY channel. The counts rate of Obs B1 is constant for any channels as shown in Figure 5.14 left because the Obs B1 is observed during the contact pass, and the data acquisition rate was set to very high, thus the counts in the channels larger than RAWY channel grow up linearly as shown in Figure 5.14 right. However, in other observations in Obs B, the telemetry seems to be saturated around 512–640 ch. We set RAWY channels as 0–256 ch, 0–512 ch, and 0–1024 ch to see the effect of telemetry saturation, here 0–256 ch and 0–512 ch should not to be affected the telemetry saturation as shown in Figure 5.14. Thus, comparing 0–1024 ch and 0–256/0–512 ch, we can estimate the effect of the telemetry saturation.

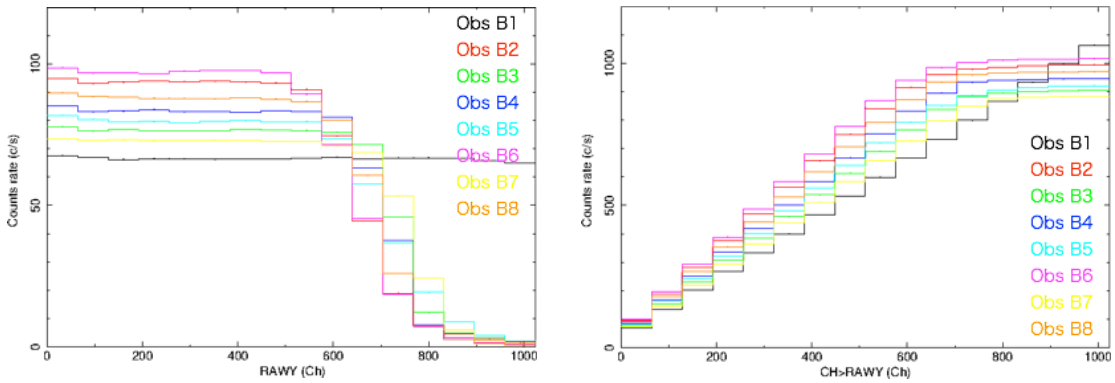

Figure 5.14: The histograms of counts in RAWY for Obs B1–B8. Left: the horizontal axis is corresponding to the channel in RAWY. Right: the horizontal axis is corresponding to the channels larger than RAWY channel.

To construct a power spectrum, we utilize a command of *powspec*. The command has a hidden argument for a normalization, we utilize the argument of 2 to have a power spectra in units of rms^2 Hz^{-1}. If we utilize the argument of -2, the white noise is subtracted automatically, however, the *powspec* may mistake to estimate the white noise level. Thus, in this study, we subtract the white noise by manually to have a strict discussion. Figure 5.15 shows the example of the white noise estimation and subtraction. The upper left panel in Figure 5.15 shows the example of a power spectrum of lower energy band (1.5–2.0 keV) constructed by *powspec* with the normalization argument of 2, and lower left panel shows the that of higher energy band (6.0–10.0 keV). We use above 15 Hz to estimate the white noise level, and subtract the white noise. The power spectrum after subtraction of the white noise are shown in the right panels of Figure 5.15. We can see that the power spectrum of higher energy band has more power.

Figure 5.16 shows the PSD (power spectrum density) of lower energy band (1.5–2.0 keV, left), and higher energy band (6.0–10.0 keV, right) of Obs B4. In this figure, the vertical axis is in the unit of frequency $\times$ power [rms^2 Hz^{-1} Hz], which unit is

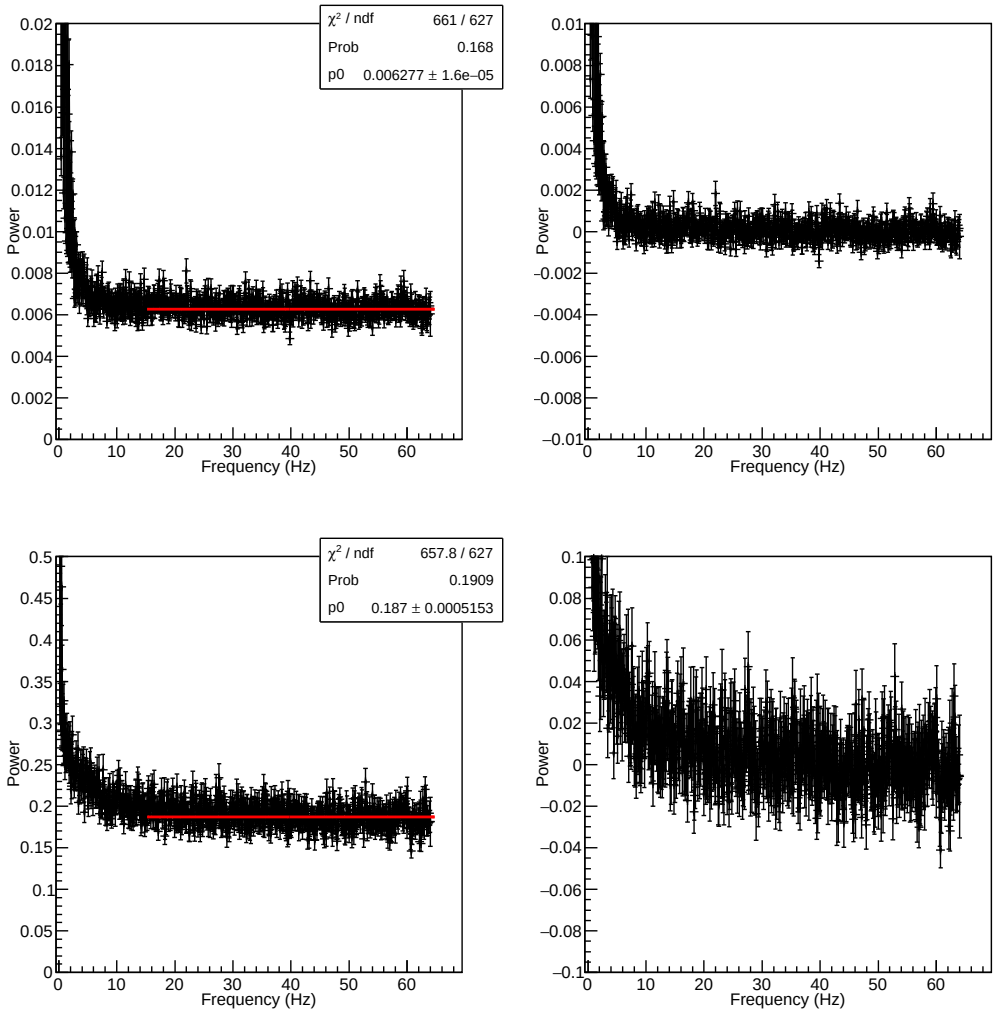

Figure 5.15: The example of the white noise estimation/subtraction of power spectrum. The upper left panel: the power spectrum of lower energy band (1.5–2.0 keV) constructed by *powspec* with the normalization argument of 2. The upper right panel: after subtraction of white noise of the upper left panel. The lower left/right panels: that of higher energy band (6.0–10.0 keV).

widely used to discuss the PSD, and three PSDs are compared among 0–256 ch, 0–512 ch, and 0–1024 ch. The bin time of 0-1024 ch is set to 8 sec. While, the bin times of 0-512 ch and 0-256 ch are set to 4 sec and 2 sec, respectively. Additionally, we used time filter to avoid null time interval for 0–256 ch and 0–512 ch.

The statistics of 0–256 ch is poor as expected, however, these three PSDs are consistent with each other for both of lower energy band and higher energy band. Thus, it means, the effect of telemetry saturation is negligible for this study. Hereafter we only use the PSD of 0–1024 ch to have better statistics. In the PSD of lower energy band shows flat structure for any frequency, while there is "mountain structure" around ∼10 Hz in higher energy band. The "mountain structure" has never been seen in the high/soft state of Cyg X-1 (Grinberg et al. 2014), and seems to be the middle structure between the typical structure of Cyg X-1 and other black hole binaries (See Figure 2.21).

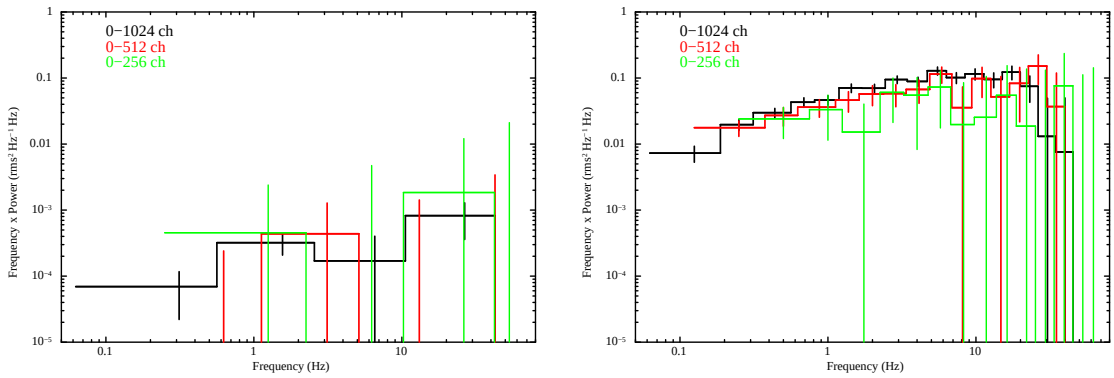

Figure 5.16: The PSD (power spectrum density) of lower energy band (1.5–2.0 keV, left), and higher energy band (6.0–10.0 keV, right) of Obs B4. Black: 0–1024 ch, Red: 0–512 ch, Green: 0–256 ch.

The comparison of PSDs of eight segments in Obs B is shown in Figure 5.17. In the left panel of Figure 5.17, the PSDs in lower energy band (1.5–2.0 keV) are almost consistent with each other, while in the right panel, Obs B4 has significantly higher power than other segments, which have "flat structure" as typical PSD of Cyg X-1. The spectrum of Obs B4 is the softest spectrum of Cyg X-1 ever observed, thus, it means the fewest Comptonization component. Therefore we can imagine that Cyg X-1 had fewer corona and/or fewer stellar wind during Obs B4. The intensity of the flat part (∼0.1 Hz) of the PSDs of higher energy band is almost consistent with the that of typical PSD of Cyg X-1 (See Figure 2.21). The assumed geometry makes it difficult to estimate the origin of the "mountain structure" in the PSD, because there is an additional structure in the PSD event tough less component in the spectrum.

Here, we note that the PSD of the Obs B7 also has a weak "mountain structure" but the spectrum of Obs B7 has significantly higher tail than Obs B4 as shown in Figure 4.7, and we do not understand the reason why Obs B7 could have the

structure.

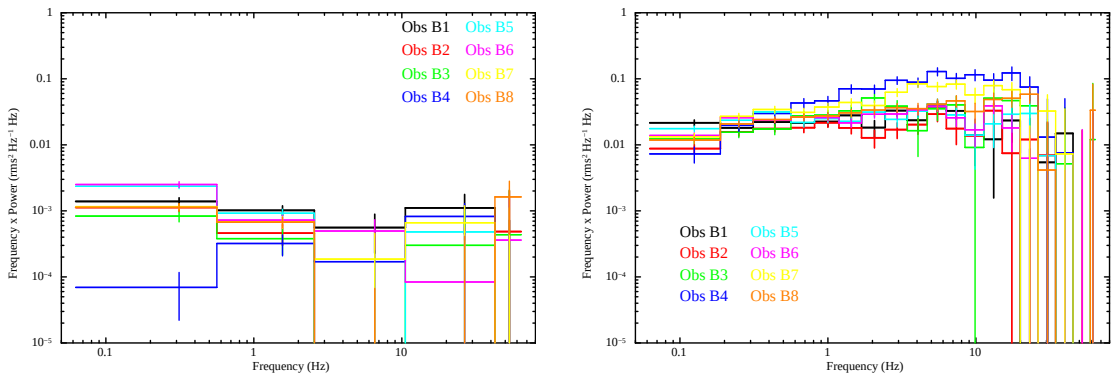

Figure 5.17: The comparison of PSDs of eight segments in Obs B. Left: lower energy band (1.5–2.0 keV), Right: higher energy band (6.0–10.0 keV). Black: Obs B1, Red: Obs B2, Green: Obs B3, Blue: Obs B4, Cyan: Obs B5, Magenta: Obs B6, Yellow: Obs B7, Orange: Obs B8. The Obs B4 has the highest power in Obs B.

To estimate the contamination of faster variability in lower energy band (1.5–2.0 keV), we compared the PSD between higher energy band (6.0–10.0 keV) and lower energy band as shown in Figure 5.18. The Comptonization component can have variability not only fast one but also slow one, while the disk component should have slow variability only. Thus the ratio between the higher and lower energy band in the fast variability, ∼10 Hz, could give us the contamination level of the Comptonization component. Actually, the shape of the ∼10 Hz is almost comparable between lower energy band and higher energy band, thus, it would support the theory. Here, we note that around 0.125 Hz, there is a characteristic peak in higher energy band. It is caused by the read out noise of 8 sec.

We compared the spectral model with the ratio between lower energy band (1.5–2.0 keV) and higher energy band (6.0–10.0 keV). The ratio of high frequency components and total components are summarized in Table 5.1 – Table 5.4, where we consider the non-thermal Comptonization component and the reflection of the non-thermal component have high frequency. The Standard model and Standard model geometry-core has ∼12% of high frequency components in lower energy band. While, +thermal models have 4-7% of high frequency components. The left panel of Figure 5.18 shows the PSD in the unit of frequency × power [rms^2 Hz^{-1} Hz], which is corresponding to raw data. While, in the right panel is in the unit of $\sqrt{\text{frequency} \times \text{power}} \times$Count rate in lower energy band [rms counts sec^{-1}], the standard model (12% level) is shown in red line, and the +thermal model (4% level) is shown in green line, respectively. Thus, in the right panel, we can estimate the contamination level directly. The standard model shows larger power than the lower energy band above ∼1 Hz. Therefore it is rejected. On the another front, the +thermal model is less than (consistent with) the lower energy band, and it is allowed.

While, the low temperature solution of KERRBB +COMPTT with 2-reflection

model is depending on whether we consider COMPTT as connected to the disk as other models or not. If we consider COMPTT as connected to the disk (only slow variability), then the ratio is ∼4% and allowed, but if we consider COMPTT as connected to the corona (can have a fast variavility), then the ratio is ∼9% and rejected. The shape of the COMPTT is away from black body, and has lower temperature than the disk, so it seems not to be connected the disk, however, the optical depth is relatively high, thus, the origin of the low temperature COMPTT is still under discussion. Here, we note that we can reject the low temperature solution with the exist of the fast time lags (Pottschmidt et al. 2000; Grinberg et al. 2014), see §6 for detail. In another front, we can not estimate the fast variability level for EQPAIR model because the model is highly convolved for thermal/non-thermal component.

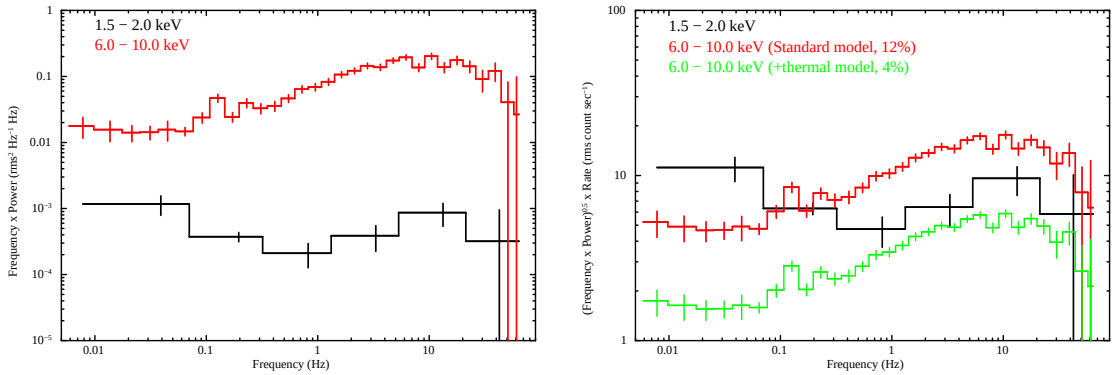

Figure 5.18: The comparison of the PSDs between lower energy band (1.5–2.0 keV), and higher energy band (6.0–10.0 keV). Left: black line shows the lower energy band, and red line shows the higher energy band. The vertical axis is in the unit of frequency × power [rms^2 Hz^{-1} Hz]. Right: black line shows the lower energy band, red line shows the standard model of the higher energy band, and the green line shows the +thermal model of the higher energy band. The vertical axis is in the unit of $\sqrt{\text{frequency} \times \text{power}}$ × Count rate in lower energy band [rms counts sec^{-1}].

5.3 Modeling the soft spectra with stronger tail

We check the consistency of models utilizing the soft spectra with strong Compton tail of A2iii. The spectrum is very similar to *Suzaku* 2010 data, which is used in Gou et al. (2014) and showed extremely high spin, as shown in Figure 4.8. In this section, we adopt the models of the Standard model, KERRBB +COMPTT with 2-reflection model, and DISKBB +COMPTT with 2-reflection model to avoid a redundant sentence.

Figure 5.19 shows the fitting result with the Standard model. The parameters are given in Table 5.5. This model gives a high spin, $a_* \sim 0.94$, similar to the results of B4 and Gou et al. (2014). The scattered fraction is significantly higher than B4 while is close to Gou et al. (2014). We can see large PIN residuals in Fig.5.19 have some discrepancies below 20 keV, showing that the data are not well described by the high energy tail used in this model as seen in B4. Therefore, A2iii data also suggest that the data would be better fit by two different Comptonisation components (Gierliński et al. 1999; Zdziarski et al. 2002).

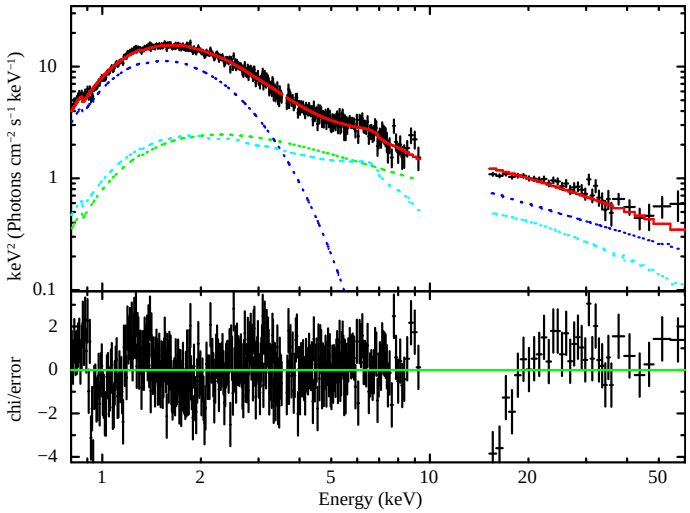

Figure 5.19: The fitting results of Obs A2iii. Assuming Standard disk model (disk and Comptonization of disk photons, corresponding to Gou et al. (2014)). Red: total, Green: KERRBB , Blue: Comptonization of KERRBB , Cyan: reflection of the Comptonization.

Then, we try to use models with an additional thermal component of COMPTT. In previous sections, we found that the reflection of soft Comptonization component significantly works to explain the spectrum, thus we reflect both of the soft Comptonization and non-thermal Comptonization component. Also, to estimate the black hole spin more strictly, we utilize relativistic disk of KERRBB and non-relativistic disk of DISKBB. So, we utilize the model of KERRBB +COMPTT with 2-reflection model and DISKBB +COMPTT with 2-reflection model. The results give a significantly better χ^2/d.o.f. and a significantly lower spin. The fitting results are shown in Figure 5.20 and Table 5.5. The emission which was previously fit as the highest

temperature emission from the disk, driving the high spin, is now fit instead as the thermal Comptonization component as seen in B4 results. Therefore, we can see the consistency of the models we have constructed.

We can briefly conclude that the Standard model always shows extremely high spin and worse χ^2/d.o.f.. While models with an additional component of the soft Comptonization show significantly better χ^2/d.o.f. and lower black hole spin.

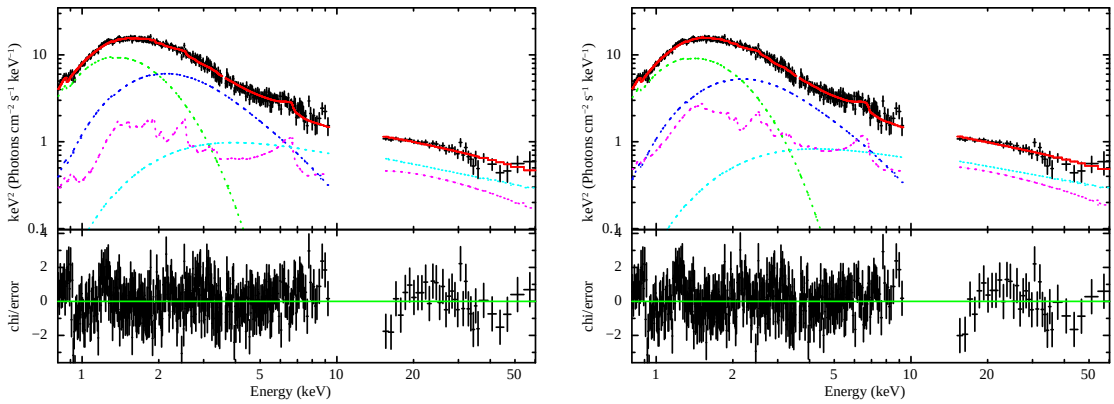

Figure 5.20: The fitting results of Obs A2iii. Left: KERRBB +COMPTT with 2-reflection model (Kerr disk and thermal(COMPTT)/non-thermal Comptonization and reflection of both of the Comptonization). Right: DISKBB +COMPTT with 2-reflection model (Schwarzschild disk and thermal(COMPTT)/non-thermal Comptonization and reflection of both of the Comptonization). Red: total, Green: KERRBB for left, DISKBB for right, Blue: COMPTT, Cyan: Comptonization of COMPTT, Magenta: reflection both of the COMPTT and Comptonization.

Table 5.5: Results of fitting the spectra with stronger tail from Obs A2iii

Component	Parameter	Standard	KERRBB +COMPTT 2-ref	DISKBB +COMPTT 2-ref
TBNEW_GAS	N_H [10^{22} cm^{-2}]	$0.67^{+0.02}_{-0.02}$	$0.76^{+0.04}_{-0.03}$	$0.64^{+0.04}_{-0.04}$
CSIMPL	Γ	$2.88^{+0.04}_{-0.03}$	$2.59^{+0.10}_{-0.12}$	$2.54^{+0.10}_{-0.10}$
	FracSctr	$0.087^{+0.011}_{-0.006}$	$0.09^{+0.02}_{-0.03}$	$0.09^{+0.02}_{-0.02}$
KERRBB	a_*	$0.94^{+0.02}_{-0.02}$	<0.87	—
	Mdd [g s^{-1}]	$0.16^{+0.01}_{-0.01}$	$0.28^{+0.16}_{-0.04}$	—
DISKBB	T_{in} [keV]	—	—	$0.37^{+0.07}_{-0.09}$
	norm	—	—	$1.50^{+1.10}_{-0.32} \times 10^5$
COMPTT	T_0 [keV]	—	$0.40^{+0.04}_{-0.06}$	$0.41^{+0.05}_{-0.03}$
	kT [keV]	—	$2.15^{+1.55}_{-0.06}$	$2.03^{+0.85}_{-0.54}$
	taup	—	$2.97^{+1.17}_{-1.84}$	$3.66^{+1.34}_{-0.97}$
	norm	—	$0.40^{+0.04}_{-0.06}$	$3.92^{+2.09}_{-1.26}$
XILCONV	log(ξ)	$4.27^{+0.09}_{-0.24}$	$2.88^{+0.33}_{-0.18}$	$3.36^{+0.21}_{-0.33}$
	χ^2/d.o.f.	484.39/402	426.75/398	431.05/398

Standard disk model: Kerr disk and Comptonization of disk photons

KERRBB +COMPTT 2-ref model: Kerr disk and thermal(COMPTT)/non-thermal Comptonization and reflection of both of the Comptonization

DISKBB +COMPTT 2-ref model: Schwarzschild disk and thermal(COMPTT)/non-thermal Comptonization and reflection of both of the Comptonization

See APPENDIX for parameter definitions.

Chapter 6

Discussion and conclusion

The 2013 Suzaku data include the softest ever spectrum seen from Cyg X-1. This means that these data have the smallest contamination from the high energy Compton tail, so should give the best determination of black hole spin from disk continuum fitting. However, we see clear evidence (more than 5σ of F-test) that there is additional Comptonisation. Including this component significantly lowers the derived black hole spin compared to standard models where there is only a disk and high energy Compton tail.

Previous modeling of this low temperature thermal Comptonisation component was done using a single zone hybrid (thermal plus non-thermal) Comptonisation, which naturally produces low temperature thermal Comptonised emission even if the electrons are accelerated by purely non-thermal processes. These self consistent models derive the steady state electron distribution by balancing heating/acceleration with Coulomb and Compton cooling (Coppi 1999; Gierliński et al. 1999). However, the fast time lags in these data (Pottschmidt et al. 2000; Grinberg et al. 2014) require that the Comptonisation is radially stratified, rather than arising from a single zone model. Then it seems more plausible that there are really two spatially separated electron distributions, with the low temperature thermal Comptonisation produced at larger radii, and non-thermal Comptonisation (or more likely, a true hybrid Comptonisation component) produced closer to the black hole (see also Gierliński & Done 2003; Hjalmarsdotter et al. 2016; Kubota & Done 2016). The exist of the fast time lags reject low temperature COMPTT solution because the low temperature COMPTT covers whole of the thermal emission and then, the model can not explain the fast time lag.

Furthermore, we have tried to constrain the spectral models with timing analysis. The timing analysis constrain that the fast variability only can be contaminated $\sim$5% level in 1.5–2.0 keV. The estimated value of the fast variability in 1.5–2.0 keV of the Standard model is $\sim$12% level and can not explain the PSD. While, the estimated value of the fast variability in 1.5–2.0 keV of the complex models, which have an additional component, is $\sim$4% level. Thus, the complex models are more pertinent, and support the exist of the additional component. However, we can not estimate the fast variability level for EQPAIR model because the model is highly convolved for thermal/non-thermal component.

The origin of this additional Comptonisation is not clear. We model it in the context of the hybrid Comptonisation. This is naturally produced in the self consistent models which derive the steady state electron distribution by balancing heating/acceleration with Coulomb and Compton cooling (Coppi 1999). However, it is also plausible that there are really two spatially separated electron distributions, with the thermal Comptonisation being connected to the disk while the non-thermal Comptonisation is produced in the corona (see also Gierliński & Done 2003). We note that the other similarly Comptonised soft state seen from XTE J1753−0127 has little X-ray variability (Shaw et al. 2016) and strongly quenched jet emission (Rushton et al. 2016), both of which are features of the disk rather than the corona.

One possibility for the origin of the low temperature Comptonisation region is

that it could be from the disk itself. Cyg X-1 has a long term mass accretion rate which is close to the major hard-to-soft spectral transition, and it is not at all clear whether the source ever fully reaches the classic high/soft state seen in other, brighter, black hole binaries. Other low inclination systems such as GX 339−4 and XTE J1817−330 show ultra soft disk dominated spectra in their lowest luminosity soft states, where the disk dominated spectra have the lowest temperature. In Cyg X-1 the ratio of unabsorbed 6-10 keV/2-6 keV flux in our softest spectrum is 0.05 not < 0.03 as observed in GX 339−4 (Muñoz-Darias et al. 2013). Either Cyg X-1 does not quite reach the soft state proper, or the spin in Cyg X-1 is much higher than that of GX 339−4. We note that reflection fits generally give an extremely high spin for GX 339−4.

The spectrum we could see a consequence of the disk structure in a failed hard-to-soft spectral transition. Other failed hard-to-soft (or very long intermediate state) transitions are reviewed in e.g. Negoro & Maxi Team (2010); Negoro & MAXI Team (2014). Of these, XTE J1753−0127 also shows a similarly very soft Comptonised spectrum appearing on a failed hard to soft transition at very low luminosity. However, it showed more standard disk spectra during higher luminosity failed hard to soft transitions (Shaw et al. 2016), so it is not at all clear what is the trigger for this different behavior. However, it is clear that the soft spectrum of Cyg X-1 is more complex than a simple disk model in these data, and this means that using it to derive black hole spin is not robust. If there is similar soft Comptonisation in the other high/soft state spectra from Cyg X-1 (as seen in Gierliński et al. 1999; Zdziarski et al. 2002), then the high spins derived in the literature from simple disk fits (e.g. Gou et al. 2011, 2014; Tomsick et al. 2014; Walton et al. 2016) may also be systematically overestimated. We also note that similarly complex Comptonisation is also seen in the much higher luminosity system GRS 1915+105, where again its inclusion lowers the derived black hole spin (compare McClintock et al. (2006) with Middleton et al. (2006)).

In the context of the truncated disk model for the spectral transitions (e.g. Esin et al. 1997; Done et al. 2007), an incomplete transition means that the truncated inner disk is still reforming, condensing out of the hot inner flow (Meyer et al. 2007). Hence its vertical structure could be somewhat different than that of a standard thin disk. This results in a lower density, and hence larger color temperature correction (Blaes et al. 2006; Begelman & Pringle 2007; Done & Davis 2008; Davis et al. 2009; Tao & Blaes 2013; Salvesen et al. 2013). Higher temperature inner regions lead to an overestimate of the black hole spin, as demonstrated in our spectral fitting. In particular, any remaining large scale magnetic fields could give pressure support (see e.g. Sądowski 2016, and references therein), perhaps producing a transition Comptonised region between a fully condensed, outer thin disk and the hot inner flow.

However, there are no good models of such a composite disk. The KERRBB (and BHSPEC) models include only a fixed color temperature correction (or fixed vertical structure for the radiation transfer), and fixed inner radius at $R_{\rm isco}$. We

approximated this composite disk structure in two ways, firstly by simply including a blackbody/low temperature Comptonization region in addition to the KERRBB component. This is not entirely appropriate as the outer disk should not then extend down to $R_{\rm isco}$, as assumed by the KERRBB model. Instead, we used the much more complex EQPAIR model, which allows a composite structure for the disk and/or corona, but where we can include only approximate ray tracing to describe the spectrum as seen at infinity (Done et al. 2013; Kubota & Done 2016). Both approximate models for a complex disk give much lower spin, $a_* \lesssim 0.8$. This is compatible with the recent upper limit on spin of $a_* < 0.7$ for the more massive black hole in the recent detection of gravitational waves from a black hole-black hole binary merger (Abbott et al. 2016).

While we cannot do a full spectral-timing analysis on our data due to limitations of the instrument modes, we note that the previous high/soft states with stronger tails used RXTE PCA data (Gou et al. 2011, 2014; Tomsick et al. 2014; Walton et al. 2016). Thus the fast time lags in these spectra can be used to determine the soft Compton component contribution unambiguously. We strongly urge full spectral-timing analyses wherever possible in order to get independent constraints on continuum complexity.

Appendix A

Detail of parameter definitions

Table A.1: Disk models

Component	Parameter	detail	treatment in this thesis
DISKBB	Tin [keV]	temperature at inner disk radius	free parameter
	norm	$(R_{in}/D_{10})^2 cos\theta$	free parameter
		R_{in}: an apparent inner disk radius in km	
		D_{10}: the distance to the source in units of 10 kpc	
		θ: the inclination angle of the disk (θ=0: face on)	
KERRBB	eta	ratio of the disk power produced by a torque at the disk inner boundary to the disk power arising from accretion	0 (fix)
	a	specific angular momentum of the black hole	free parameter
	i [deg]	the inclination angle of the disk (i=0: face on)	27.1 (fix)
	Mbh	the mass of the black hole in units of the solar mass	14.8 (fix)
	Mdd [10^{18} g/s]	the effective mass accretion rate of the disk	free parameter
	Dbh [kpc]	the distance from the observer to the black hole	18.6 (fix)
	hd	spectral hardening factor (T_{col}/T_{eff})	1.7 (fix)
	rflag	a flag to switch on/off the effect of self-irradiation	1 (fix)
	lflag	a flag to switch on/off the effect of limb-darkening	0 (fix)
	norm	normalization	1 (fix)

Table A.2: Thermal component models

Component	Parameter	detail	treatment in this thesis
BB	kT [keV]	temperature	free parameter
	norm	L_{39}/D_{10}^2	free parameter
		L_{39}: the source luminosity in units of 10^{39} erg/sec	
		D_{10}: is the distance to the source in units of 10 kpc	
BBRAD	kT [keV]	temperature	free parameter
	norm	R_{in}^2/D_{10}^2	free parameter
		R_{in}: the source radius in km	
		D_{10}: the distance to the source in units of 10 kpc	
NTHCOMP	Γ	asymptotic power-law photon index	free parameter
	kT_e	electron temperature (high energy rollover)	free parameter
	kT_{bb}	seed photon temperature (low energy rollover)	free parameter
	inp_type	0 or 1 for blackbody or disk-blackbody seed photons	0 (fix)
	Redshift	redshift	0 (fix)
	norm	normalization, unity at 1 keV for a norm of 1	free parameter
COMPTT	Redshift	redshift	0 (fix)
	T0 [keV]	Input soft photon (Wien) temperature	free parameter
	kT [keV]	Plasma temperature	free parameter
	taup	Plasma optical depth	free parameter
	approx	Geometry switch	1 (fix)
		$\leq$1 disk, >1 sphere, 0 use analytic approximation	
	norm	normalization	free parameter

Table A.3: Fully hybrid electrons model

Component	Parameter	detail	treatment in this thesis
EQPAIR	l_h/l_s	ratio of the hard to soft compactnesses	free parameter
	l_{bb}	the soft photon compactness	10 (fix)
	kT_{bb} [eV]	if >0 then temperature of a blackbody	free parameter
		if <0 then abs (kTbb) is the Tmax parameter	
		for the `diskpn` model	
	l_{nt}/l_h	fraction of power supplied to energetic particles	1 (fix)
		which goes into accelerating non-thermal particles	
	τ_p	the Thomson scattering depth	free parameter
	radius [cm]	the size of the scattering region	10^7 (fix)
	γ_{min}	minimum Lorentz factor of the pairs	1.3 (fix)
	γ_{max}	maximum Lorentz factor of the pairs	1000 (fix)
	Γ_{inj}	a power-law from γ_{min} to γ_{max}	free parameter
	pairinj	0/1 accelerated particles are electrons from thermal pool,	0 (fix)
		accelerated particles are electrons and positrons	
	cosIncl	inclination of reflecting material wrt line-of-sight	cos(27.1 deg) (fix)
	Refl	fraction of scattering region's emission	0 (fix)
		intercepted by reflecting material	
	Fe_abund	relative abundance of iron	1 (fix)
	Ab_met	relative abundance of other metals	1 (fix)
	T_disk [K]	temperature of reflecting disk	10^6 (fix)
	ξ	ionization parameter of reflector	0 (fix)
	β	power-law index with radius of disk reflection emissivity	-10 (fix)
	R_{in} [GM/c^2]	inner radius of reflecting material	10 (fix)
	R_{out} [GM/c^2]	outer radius of reflecting material	1000 (fix)
	Redshift	redshift	0 (fix)
	norm	normalization	free parameter

Table A.4: Reflection models

Component	Parameter	detail	treatment in this thesis
RELCONV	Index1	emissivity index for r < Rbr	2.5 (fix)
	Index1	emissivity index for r > Rbr	2.5 (fix)
	Rbr	radius where emissivity changes from Index1 to Index2	6 (fix)
	a	spin of the black hole	linked to the disk
	Incl [deg]	the inclination angle of the disk	27.1 (fix)
	Rin	inner radius of the disk	-1 (fix)
		Rin < 0, continued to the ISCO	
	Rout	outer radius of the disk	400 (fix)
	limb	limb-darkening/-brightening law for mu=cos(angle$_{\rm emission}$):	0 (fix)
		0 = isotropic, 1 = darkening, 2 = brightening	
XILCONV	rel$_{\rm refl}$	the relative reflection normalization	-1 (fix)
		rel$_{\rm refl}$ <0, only the reflected component is returned	
	Redshift	redshift	0 (fix)
	Fe_abund	the iron abundance relative to Solar	1 (fix)
	cosIncl	cosine of the inclination angle	cos(27.1) (fix)
	log(ξ)	the ionization parameter used by the table models	3 (fix)
	cutoff [keV]	the exponential cut-off energy	300 (fix)

Table A.5: Comptonization of a seed spectrum models

Component	Parameter	detail	treatment in this thesis
SIMPL	Γ	the photon power law index.	free parameter
	FracSctr	The scattered fraction (between 0 and 1)	free parameter
	UpScOnly	A flag to switch. >0, up-scattering only	1 (fix)
		<0, both up- and down-scattering	
CSIMPL	Γ	the photon power law index.	free parameter
	FracSctr	The scattered fraction (between 0 and 1)	free parameter
	UpScOnly	A flag to switch. 0, up-scattering only	1 or 2 (fix)
		1, both up- and down-scattering	
		2, separated from the unscattered disk photons	

Table A.6: Absorption model

Component	Parameter	detail	treatment in this thesis
TBNEW_GAS [10^{22} atoms cm^{-2}]	nH	equivalent hydrogen column	free parameter

Acknowledgment

I would like to express my best gratitude to Prof. Chris Done in Dharam university, ISAS/JAXA. I am proud of being working with her to create dozen of models and study carefully. We have been discussing the physical meanings of the models more than thousand times, and she always provided me fruitful idea. I wish to thank for Prof. Yasushi Fukazawa in Hiroshima university for management during six years of my scientific life in high energy astrophysics group. Many thanks for Dr. Shin'ya Yamada in Tokyo metropolitan university, he kindly introduced the way of data reduction, whose method is specialized for very high counts rate data, is complicated. My special thanks for Dr. Hiromitsu Takahashi in Hiroshima university, he always kindly take any notice of myself and had a lot of deep discussions not only the subject but also other missions. I appreciate Dr. Magnus Axelsson in Tokyo metropolitan university, he gave me really pertinent advices and then I could carry forward the study. Thanks to Dr. Akifumi Yoshikawa, earlier work on these Cyg X-1 data. For all colleagues and secretaries of our group, thank you all your supports. Finally, I greatly thank my family for their infinite supports anywhere and anytime.

To study astrophysics, we need to have color pens and coffee.

My supervisor said. Shall we continue to discuss, picking up colorful pens to draw exciting pictures to explain the geometry with smelling the coffee in the air.

References

Abbott, B. P., et al. 2016, Physical Review Letters, 116, 241103

Abramowicz, M. A., Chen, X., Kato, S., Lasota, J.-P., & Regev, O. 1995, ApJ, 438, L37

Abramowicz, M. A., Czerny, B., Lasota, J. P., & Szuszkiewicz, E. 1988, ApJ, 332, 646

Albert, J., et al. 2007, ApJ, 665, L51

Arévalo, P., & Uttley, P. 2006, MNRAS, 367, 801

Axelsson, M., Borgonovo, L., & Larsson, S. 2005, A&A, 438, 999

Axelsson, M., Church, R. P., Davies, M. B., Levan, A. J., & Ryde, F. 2011, MNRAS, 412, 2260

Ballantyne, D. R., Ross, R. R., & Fabian, A. C. 2001, MNRAS, 327, 10

Begelman, M. C., & Pringle, J. E. 2007, MNRAS, 375, 1070

Belloni, T., Méndez, M., & Homan, J. 2005, A&A, 437, 209

Blaes, O. M., Davis, S. W., Hirose, S., Krolik, J. H., & Stone, J. M. 2006, ApJ, 645, 1402

Blandford, R. D., & Znajek, R. L. 1977, MNRAS, 179, 433

Blundell, K. M., & Bowler, M. G. 2004, ApJ, 616, L159

Bolton, C. T. 1975, ApJ, 200, 269

Brown, G. E., Lee, C.-H., & Moreno Méndez, E. 2008, ApJ, 685, 1063

Cantiello, M., Mankovich, C., Bildsten, L., Christensen-Dalsgaard, J., & Paxton, B. 2014, ApJ, 788, 93

Cherepashchuk, A. M., et al. 2005, A&A, 437, 561

Churazov, E., Gilfanov, M., & Revnivtsev, M. 2001, MNRAS, 321, 759

Coppi, P. S. 1999, in Astronomical Society of the Pacific Conference Series, Vol. 161, High Energy Processes in Accreting Black Holes, ed. J. Poutanen & R. Svensson, 375

Dauser, T., García, J., Parker, M. L., Fabian, A. C., & Wilms, J. 2014, MNRAS, 444, L100

Davis, S. W., Blaes, O. M., Hirose, S., & Krolik, J. H. 2009, ApJ, 703, 569

Davis, S. W., Done, C., & Blaes, O. M. 2006, ApJ, 647, 525

Done, C., & Davis, S. W. 2008, ApJ, 683, 389

Done, C., & Diaz Trigo, M. 2010, MNRAS, 407, 2287

Done, C., & Gierliński, M. 2005, MNRAS, 364, 208

Done, C., Gierliński, M., & Kubota, A. 2007, A&A Rev., 15, 1

Done, C., Jin, C., Middleton, M., & Ward, M. 2013, MNRAS, 434, 1955

Droulans, R., Belmont, R., Malzac, J., & Jourdain, E. 2010, ApJ, 717, 1022

Dunn, R. J. H., Fender, R. P., Körding, E. G., Belloni, T., & Cabanac, C. 2010, MNRAS, 403, 61

Duro, R., et al. 2011, A&A, 533, L3

Ebisawa, K., Mitsuda, K., & Hanawa, T. 1991, ApJ, 367, 213

Esin, A. A., McClintock, J. E., & Narayan, R. 1997, ApJ, 489, 865

Fabian, A. C., Rees, M. J., Stella, L., & White, N. E. 1989, MNRAS, 238, 729

Fabian, A. C., et al. 2012, MNRAS, 424, 217

Fender, R. P., Belloni, T. M., & Gallo, E. 2004, MNRAS, 355, 1105

Fragile, P. C., Straub, O., & Blaes, O. 2016, MNRAS, 461, 1356

Fukazawa, Y., et al. 2009, PASJ, 61, S17

Galeev, A. A., Rosner, R., & Vaiana, G. S. 1979, ApJ, 229, 318

Gammie, C. F., Shapiro, S. L., & McKinney, J. C. 2004, ApJ, 602, 312

García, J., et al. 2014, ApJ, 782, 76

Gierliński, M., & Done, C. 2003, MNRAS, 342, 1083

—. 2004, MNRAS, 347, 885

Gierliński, M., & Newton, J. 2006, MNRAS, 370, 837

Gierliński, M., Zdziarski, A. A., Poutanen, J., Coppi, P. S., Ebisawa, K., & Johnson, W. N. 1999, MNRAS, 309, 496

Gies, D. R., et al. 2008, ApJ, 678, 1237

Gilfanov, M., Churazov, E., & Revnivtsev, M. 1999, A&A, 352, 182

Gladstone, J., Done, C., & Gierliński, M. 2007, MNRAS, 378, 13

Gou, L., et al. 2011, ApJ, 742, 85

—. 2014, ApJ, 790, 29

Grinberg, V., et al. 2014, A&A, 565, A1

Heger, A., Langer, N., & Woosley, S. E. 2000, ApJ, 528, 368

Heger, A., & Woosley, S. E. 2002, ApJ, 567, 532

Hjalmarsdotter, L., Axelsson, M., & Done, C. 2016, MNRAS, 456, 4354

Ingram, A., Done, C., & Fragile, P. C. 2009, MNRAS, 397, L101

Ingram, A., van der Klis, M., Middleton, M., Done, C., Altamirano, D., Heil, L., Uttley, P., & Axelsson, M. 2016, MNRAS, 461, 1967

Ishisaki, Y., et al. 2007, PASJ, 59, 113

Jefremov, P. I., Tsupko, O. Y., & Bisnovatyi-Kogan, G. S. 2015, Phys. Rev. D, 91, 124030

Jourdain, E., Roques, J. P., Chauvin, M., & Clark, D. J. 2012, ApJ, 761, 27

Kalogera, V., & Baym, G. 1996, ApJ, 470, L61

Kaplan, S. A. 1949, Zhurnal Eksperimentalnoi i Teoreticheskoi Fiziki, 19, 951

Kawano, T., Done, C., Yamada, S., Takahashi, H., Axelsson, M., & Fukazawa, Y. 2017, ArXiv e-prints

Kelley, R. L., et al. 2007, PASJ, 59, 77

Kerr, R. P. 1963, Physical review letters, 11, 237

Kokubun, M., et al. 2007, PASJ, 59, 53

Kolehmainen, M., & Done, C. 2010, MNRAS, 406, 2206

Kolehmainen, M., Done, C., & Díaz Trigo, M. 2011, MNRAS, 416, 311

—. 2014, MNRAS, 437, 316

Kotov, O., Churazov, E., & Gilfanov, M. 2001, MNRAS, 327, 799

Koyama, K., et al. 2007, PASJ, 59, 23

Krimm, H. A., et al. 2013, ApJS, 209, 14

Kubota, A., & Done, C. 2016, MNRAS, 458, 4238

Kubota, A., & Makishima, K. 2004, ApJ, 601, 428

Kubota, A., Makishima, K., & Ebisawa, K. 2001, ApJ, 560, L147

Laor, A. 1991, ApJ, 376, 90

Laurent, P., Rodriguez, J., Wilms, J., Cadolle Bel, M., Pottschmidt, K., & Grinberg, V. 2011, Science, 332, 438

Lee, C.-H., Brown, G. E., & Wijers, R. A. M. J. 2002, ApJ, 575, 996

Li, L.-X., Zimmerman, E. R., Narayan, R., & McClintock, J. E. 2005, ApJS, 157, 335

Liu, Q. Z., van Paradijs, J., & van den Heuvel, E. P. J. 2006, A&A, 455, 1165

Ludlam, R. M., Miller, J. M., & Cackett, E. M. 2015, ApJ, 806, 262

Lyubarskii, Y. E. 1997, MNRAS, 292, 679

Maccarone, T. J., & Coppi, P. S. 2002, MNRAS, 336, 817

Makishima, K., Maejima, Y., Mitsuda, K., Bradt, H. V., Remillard, R. A., Tuohy, I. R., Hoshi, R., & Nakagawa, M. 1986, ApJ, 308, 635

Makishima, K., et al. 2000, ApJ, 535, 632

Manmoto, T., Mineshige, S., & Kusunose, M. 1997, ApJ, 489, 791

Markoff, S., Nowak, M. A., & Wilms, J. 2005, ApJ, 635, 1203

McClintock, J. E., Narayan, R., & Steiner, J. F. 2014, Space Sci. Rev., 183, 295

McClintock, J. E., & Remillard, R. A. 2006, Black hole binaries, ed. W. H. G. Lewin & M. van der Klis, 157–213

McClintock, J. E., Shafee, R., Narayan, R., Remillard, R. A., Davis, S. W., & Li, L.-X. 2006, ApJ, 652, 518

McKinney, J. C., & Gammie, C. F. 2004, ApJ, 611, 977

Meyer, F., Liu, B. F., & Meyer-Hofmeister, E. 2007, A&A, 463, 1

Middleton, M., Done, C., Gierliński, M., & Davis, S. W. 2006, MNRAS, 373, 1004

Miller, J. M., Homan, J., Steeghs, D., Rupen, M., Hunstead, R. W., Wijnands, R., Charles, P. A., & Fabian, A. C. 2006, ApJ, 653, 525

Miller, J. M., Reynolds, C. S., Fabian, A. C., Miniutti, G., & Gallo, L. C. 2009, ApJ, 697, 900

Miller, J. M., et al. 2012, ApJ, 759, L6

Mirabel, I. F., Dhawan, V., Chaty, S., Rodriguez, L. F., Marti, J., Robinson, C. R., Swank, J., & Geballe, T. 1998, A&A, 330, L9

Mitsuda, K., et al. 2007, PASJ, 59, 1

Miyamoto, S., & Kitamoto, S. 1989, Nature, 342, 773

Moreno Méndez, E., & Cantiello, M. 2016, New A, 44, 58

Mori, H., et al. 2005, PASJ, 57, 245

Motta, S. E., Belloni, T. M., Stella, L., Muñoz-Darias, T., & Fender, R. 2014, MNRAS, 437, 2554

Muñoz-Darias, T., Coriat, M., Plant, D. S., Ponti, G., Fender, R. P., & Dunn, R. J. H. 2013, MNRAS, 432, 1330

Narayan, R., & McClintock, J. E. 2012, MNRAS, 419, L69

Negoro, H., & Maxi Team. 2010, in The First Year of MAXI: Monitoring Variable X-ray Sources, 6

Negoro, H., & MAXI Team. 2014, in Suzaku-MAXI 2014: Expanding the Frontiers of the X-ray Universe, ed. M. Ishida, R. Petre, & K. Mitsuda, 128

Nowak, M. A. 1995, PASP, 107, 1207

—. 2000, MNRAS, 318, 361

Nowak, M. A., Vaughan, B. A., Wilms, J., Dove, J. B., & Begelman, M. C. 1999, ApJ, 510, 874

Oda, M. 1977, Space Sci. Rev., 20, 757

Oda, M., Gorenstein, P., Gursky, H., Kellogg, E., Schreier, E., Tananbaum, H., & Giacconi, R. 1971, ApJ, 166, L1

Orosz, J. A., McClintock, J. E., Aufdenberg, J. P., Remillard, R. A., Reid, M. J., Narayan, R., & Gou, L. 2011, ApJ, 742, 84

Orosz, J. A., Steiner, J. F., McClintock, J. E., Buxton, M. M., Bailyn, C. D., Steeghs, D., Guberman, A., & Torres, M. A. P. 2014, ApJ, 794, 154

Orosz, J. A., et al. 2007, Nature, 449, 872

—. 2009, ApJ, 697, 573

Overbye, D. 1991, Lonely hearts of the cosmos (McMillan)

Paczynski, B. 1974, A&A, 34, 161

Paragi, Z., et al. 2013, MNRAS, 432, 1319

Parker, M. L., et al. 2015, ApJ, 808, 9

Penrose, R. 1969, Nuovo Cimento Rivista Serie, 1

Pietsch, W., Haberl, F., Sasaki, M., Gaetz, T. J., Plucinsky, P. P., Ghavamian, P., Long, K. S., & Pannuti, T. G. 2006, ApJ, 646, 420

Pietsch, W., Mochejska, B. J., Misanovic, Z., Haberl, F., Ehle, M., & Trinchieri, G. 2004, A&A, 413, 879

Pottschmidt, K., Wilms, J., Nowak, M. A., Heindl, W. A., Smith, D. M., & Staubert, R. 2000, A&A, 357, L17

Poutanen, J., & Fabian, A. C. 1999, MNRAS, 306, L31

Rapisarda, S., Ingram, A., Kalamkar, M., & van der Klis, M. 2016, MNRAS, 462, 4078

Reid, M. J., McClintock, J. E., Narayan, R., Gou, L., Remillard, R. A., & Orosz, J. A. 2011, ApJ, 742, 83

Reis, R. C., Fabian, A. C., & Miller, J. M. 2010, MNRAS, 402, 836

Remillard, R. A., & McClintock, J. E. 2006, ARA&A, 44, 49

Rushton, A., et al. 2012, MNRAS, 419, 3194

Rushton, A. P., et al. 2016, MNRAS, 463, 628

Sabatini, S., et al. 2010, ApJ, 712, L10

—. 2013, ApJ, 766, 83

Salvesen, G., Miller, J. M., Reis, R. C., & Begelman, M. C. 2013, MNRAS, 431, 3510

Sądowski, A. 2016, MNRAS, 462, 960

Schwarzschild, K. 1916, in Sitzungsberichte der Königlich Preussischen Akademie der Wissenschaften zu Berlin, Phys.-Math. Klasse, 424-434 (1916)

Serlemitsos, P. J., et al. 2007, PASJ, 59, 9

Shakura, N. I., & Sunyaev, R. A. 1973, A&A, 24, 337

Shaw, A. W., et al. 2016, MNRAS, 458, 1636

Shidatsu, M., et al. 2011, PASJ, 63, S785

Shimura, T., & Takahara, F. 1995, ApJ, 445, 780

Smith, D. M., Heindl, W. A., & Swank, J. H. 2002, ApJ, 569, 362

Sobolewska, M. A., & Życki, P. T. 2006, MNRAS, 370, 405

Steiner, J. F., McClintock, J. E., Remillard, R. A., Gou, L., Yamada, S., & Narayan, R. 2010, ApJ, 718, L117

Steiner, J. F., Narayan, R., McClintock, J. E., & Ebisawa, K. 2009, PASP, 121, 1279

Stella, L., & Vietri, M. 1998, ApJ, 492, L59

—. 1999, Physical Review Letters, 82, 17

Stirling, A. M., Spencer, R. E., de la Force, C. J., Garrett, M. A., Fender, R. P., & Ogley, R. N. 2001, MNRAS, 327, 1273

Suijs, M. P. L., Langer, N., Poelarends, A.-J., Yoon, S.-C., Heger, A., & Herwig, F. 2008, A&A, 481, L87

Sunyaev, R. A., & Truemper, J. 1979, Nature, 279, 506

Takahashi, T., et al. 2007, PASJ, 59, 35

Tanaka, Y., & Shibazaki, N. 1996, ARA&A, 34, 607

Tao, T., & Blaes, O. 2013, ApJ, 770, 55

Tauris, T. M., & van den Heuvel, E. P. J. 2006, Formation and evolution of compact stellar X-ray sources, ed. W. H. G. Lewin & M. van der Klis, 623–665

Thorne, K. S. 1974, ApJ, 191, 507

Titarchuk, L. 1994, ApJ, 434, 570

Tomsick, J. A., Yamaoka, K., Corbel, S., Kaaret, P., Kalemci, E., & Migliari, S. 2009, ApJ, 707, L87

Tomsick, J. A., et al. 2014, ApJ, 780, 78

Ueda, Y., Ebisawa, K., & Done, C. 1994, PASJ, 46, 107

Uttley, P., Wilkinson, T., Cassatella, P., Wilms, J., Pottschmidt, K., Hanke, M., & Böck, M. 2011, MNRAS, 414, L60

Čechura, J., Vrtilek, S. D., & Hadrava, P. 2015, MNRAS, 450, 2410

Visser, M. 2007, ArXiv e-prints

Walton, D. J., et al. 2016, ApJ, 826, 87

Wilms, J., Allen, A., & McCray, R. 2000, ApJ, 542, 914

Yamada, S., Negoro, H., Torii, S., Noda, H., Mineshige, S., & Makishima, K. 2013, ApJ, 767, L34

Yamada, S., et al. 2012, PASJ, 64, 53

Yu, W., & Yan, Z. 2009, ApJ, 701, 1940

Yuan, F., Quataert, E., & Narayan, R. 2003, ApJ, 598, 301

Zanin, R., Fernández-Barral, A., de Oña Wilhelmi, E., Aharonian, F., Blanch, O., Bosch-Ramon, V., & Galindo, D. 2016, A&A, 596, A55

Zdziarski, A. A., Grove, J. E., Poutanen, J., Rao, A. R., & Vadawale, S. V. 2001, ApJ, 554, L45

Zdziarski, A. A., Johnson, W. N., & Magdziarz, P. 1996, MNRAS, 283, 193

Zdziarski, A. A., Malyshev, D., Chernyakova, M., & Pooley, G. G. 2016a, ArXiv e-prints

Zdziarski, A. A., Paul, D., Osborne, R., & Rao, A. R. 2016b, MNRAS, 463, 1153

Zdziarski, A. A., Poutanen, J., Mikolajewska, J., Gierlinski, M., Ebisawa, K., & Johnson, W. N. 1998, MNRAS, 301, 435

Zdziarski, A. A., Poutanen, J., Paciesas, W. S., & Wen, L. 2002, ApJ, 578, 357